Symmetry matching excitation of rotational symmetric plasmonic nanostructures

Dissertation

der Mathematisch-Naturwissenschaftlichen Fakultät

der Eberhard Karls Universität Tübingen

zur Erlangung des Grades eines

Doktors der Naturwissenschaften

(Dr. rer. nat.)

vorgelegt von

Dipl.-Chem. Sebastian Jäger

aus Albstadt

Tübingen

2013

Tag der mündlichen Qualifikation: 07.02.2014

Dekan: Prof. Dr. Wolfgang Rosenstiel

1. Berichterstatter: Prof. Dr. Alfred J. Meixner

2. Berichterstatter: PD Dr. Marc Brecht

for Regina, I love you!

Table of contents

List of abbreviations and symbols

Abbreviations

AO	air objective lens
APD	avalanche photo diode
APDM	azimuthally polarized doughnut mode
Au	gold
CVB	cylindrical vector beams
FRET	Förster resonance energy transfer
FWHM	full width at half maximum
HG	Hermite-Gauss
ITO	indium tin oxide
MC	mode converter
NA	numerical aperture
nm	nano meter
NV center	nitrogen vacancy center
OL	objective lens
PALM	photoactivated localization microscopy
PH	pinhole
PM	parabolic mirror
RPDM	radially polarized doughnut mode
SEM	scanning electron microscopy
SERS	surface enhanced raman spectroscopy
SNOM	scanning near field optical microscope
SRR	split ring resonator
STED	stimulated emission depletion
STORM	stochastic optical reconstruction microscopy
TIRF	total internal reflection fluorescence
cw	continuous wave

Symbols

I	intensity
c	speed of light
ε	dielectric constant
ε_0	vacuum permittivity
k	wave vector
λ	wavelength
n	index of refraction
P	power
ω	angular frequency

1. Introduction

1.1. Motivation

The luminescence of gold was first reported by Mooridan in 1969.[MOO69] This discovery was possible, after Maiman invented the laser in 1960.[MAI60] Mooridan excited gold, copper and gold-copper alloys with the Ar-Ion laser wavelengths of 488 nm and 514.5 nm. He found luminescence spectra where the positions of the spectral maxima are independent of the excitation wavelength with a quantum efficiency of around 10^{-10}.[MOO69] The quantum efficiency of gold luminescence rises dramatically if, instead of bulk gold, small particles are used.[BOY86]

Especially in nano particles, the luminescence of gold is greatly enhanced. This enhancement is closely related to the plasmonic behavior of gold nano particles. Plasmons are collective, coherent oscillations of the conduction band electrons in a metal and are named in 1960 by Stern and Ferrell, where they are using the term "surface plasmon" for a shortcut of "surface plasma oscillation".[STE60] In nano particles, these oscillations are called particle plasmons, here the electrons of the whole particle are oscillating, contrary to surface plasmons that are localized at the surface of a metal film. These particle plasmons exhibit resonance frequencies, which depend on the particle size, shape, refractive index of the surrounding media and material composition. here light is effectively absorbed and scattered. [KEL03, MAL01] These extraordinary optical properties made gold nano particles a valuable candidates for microscopic investigations e.g. as markers for biological systems.[ANK08, JOU13, SAH12, SHA11]

The simplest type of such nano particles are spherical particles. Their optical properties are isotropic and can be described by the Mie theory.[BOH83, MIE08] The variation of the shape also alters the optical properties of the nano particles. To determine the optical properties like the plasmon resonance of such nano particles the straight forward method is to acquire an absorption-, extinction- or scattering spectrum of a nano particle solution usually in water.[DOR64] Alternatively, when the nano particles or -structures are fabricated on a surface, dark field microscopy and spectroscopy can provide scattering spectra of single nano particles[SOE01], while transmission- or absorption spectra can be taken of nano structures manufactured as arrays on a surface [VER09]. Nearly all of these

methods are using linearly or randomly polarized light for the examination of the plasmonic properties.

In microscopy, the orientation of such nano particles can be determined by using laser beams with cylindrical polarization properties, namely radially and azimuthally polarized laser modes. [FAI07, WAC12] This method already utilizes that the polarizability of gold nano rods is different in the main axis compared to the short axis at given wavelengths. Excitation using the focus of a high numerical aperture objective radially or azimuthally polarized laser beam offer the possibility to excite selectively in z direction or in the sample plane. In a similar fashion, nano structures that have a symmetry matching the focal fields can be investigated.

In this thesis, all investigated structures have a rotational symmetry in common. The rotation axis for all these structures is normal to the substrate in the center of the structure. In combination with the radially and azimuthally polarized laser modes, a stepwise match of the symmetry of the possible plasmonic polarizability and the excitation is established. At the beginning only a match with the symmetry of the radially polarized laser focus with the nanostructure is made by the investigation of gold nano posts on glass, gold nano discs on silicon and gold nano cones on glass. With the gold nano posts, an examination of the focal fields with different types of microscopes and focusing elements is done to evaluate the capabilities of the individual microscopes to image plasmonic systems. Second, with the investigation of gold discs on silicon, first spectroscopic measurements of the gold luminescence of plasmonic structures are introduced. For the discrimination in polarization between the focal fields of azimuthally and radially polarized laser beams, an interesting spectroscopic phenomenon is found when gold nano cones are excited. A first variation of the cross section of the structure is done by the investigation of gold nano rings, but here no azimuthally excitability of the structure exists. Finally a way for nearly perfect excitation symmetry match between the azimuthal polarization and a plasmonic structure is found by using so called plasmonic oligomers. One plasmonic oligomer is a hexagonal arrangement of seven aluminum discs that, as a collective, can be tuned to achieve an azimuthal resonance. By excitation of this azimuthal resonance, a strong near field between the six outer particles of the oligomer is formed. To study this near field, a new scanning near field optical microscopy (SNOM) operation mode, utilizing the one-photon gold luminescence, is developed.

1.2. Outline of this thesis

In chapter 2 the theoretical background for this work is stated. First, a short introduction into the field of plasmonics, ranging from surface to particle plasmons, is given. In addition the mechanisms of the one-photon gold luminescence are explained to give an insight in the investigated processes. The second part of chapter 2 is a brief introduction of the techniques used for the experiments of this thesis, namely confocal microscopy and near-field microscopy. Furthermore the used azimuthally and radially polarized laser beams, also called cylindrical vector beams (CVB), and their focal fields are described. The used hardware for these techniques is described in chapter 3, where the different microscopes as well as the mode conversion are described.

The fourth chapter includes the complete experimental part of this work. Here the individual experiments are presented in detail and the results are discussed accordingly. In Chapter 4.1 four different focusing elements are tested by their capabilities to image gold nano posts on a glass surface. Chapter 4.2 focuses on the luminescence behavior of gold discs on silicon, whereas in chapter 4.3 the difference in the spectra of gold cones on glass when excited with radial or azimuthal polarization is investigated. Subsequently, in chapter 4.4 gold nano rings raster scanned through the focus of the two laser modes, lead to an interesting imaging behavior. In chapter 4.5 the transition of splitring resonators to plasmonic oligomers and their excitability with radial and azimuthal polarization is presented. For the investigation of the plasmonic oligomers a new SNOM operating mode is invented.

Finally in chapter 5, I will give a summary and conclusion of the achieved results and end with an outline which experiments can be done further to obtain new insights in the field of nano plasmonics.

2. Theoretical background

2.1. Plasmons

Plasmons are the energy quanta similar to photons of coherent density oscillations of the conduction band electrons in a metal. To support such a plasmon, the real part of the dielectric constant of the plasmon material, ε_1' has to be smaller than 0, while the absolute value of ε_1' has to be larger than the dielectric constant of the surrounding medium ε_2. This can be found in metals and doped semiconductors.

2.1.1. Surface plasmons

Surface plasmons are plasmons localized at interfaces of e.g. a metal and a dielectric media. The surface plasmons are longitudinal waves with the wave vector k_x, that can therefore be detected by an evanescent, electromagnetic field in z-direction. The dispersion relation of a surface plasmon is given by:

$$k_x = \frac{\omega}{c} \cdot \sqrt{\frac{\varepsilon_1 \cdot \varepsilon_2}{\varepsilon_1 + \varepsilon_2}} \qquad (2.1)$$

ω frequency of the plasmon

c speed of light

ε_1 dielectric constant of the plasmon material

ε_2 dielectric constant of the surrounding media

Photons can't excite surface plasmons directly, due to the fact that the wave vectors k of photons with the same energy like the corresponding plasmon are given by $\omega = c \cdot k_x / n$, so they are not as long as the wave vector of the plasmon (see Figure 1). One possibility to couple photons into surface plasmons uses the evanescent field of a totally reflected light beam, used i.e. in the Kretschmann configuration where a thin metal film is evaporated on a glass prism.[KRE71] Here the wave vector of the light at the glass-metal interface is big enough to excite a plasmon at the metal-air interface. A second way to couple light into

surface plasmons utilizes optical gratings to increase the wave vector of the incoming light by the reciprocal lattice vector of the grating.[MAI07, NOV06, RAE88]
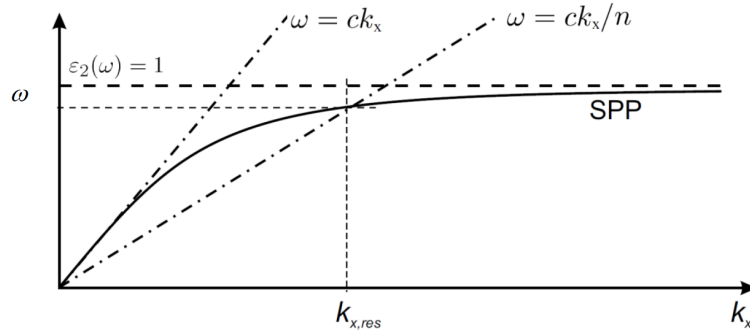

Figure 1: Dispersion relation of a Surface Plasmon (SPP). The free space light line is marked with $\omega = ck_x$ while the light line in glass is tilted ($\omega = ck_x/n$). Taken from Ref. [NOV06]

2.1.2. Particle plasmons

The confinement of a surface plasmon takes place in *z*-direction, while it is propagating along the surface. To confine a plasmon in more dimensions the geometry of the material has to be adapted going to small particles. Here, the surface plasmons are localized to the size of the particle and thus are called localized surface plasmons or particle plasmons. The movement of the conduction electrons inside of the geometrical confinement of a small particle creates a displacement in respect to the positively charged atomic cores. This displacement of positive and negative charge creates an electric field that acts as a restoring force. For particles smaller than the wavelength, this response has the properties of a dipole with the polarizability:

$$\alpha(\omega) = 4\pi\varepsilon_0 a^3 \left(\frac{\varepsilon_1(\omega) - \varepsilon_2}{\varepsilon_1(\omega) + 2\varepsilon_2} \right) \tag{2.2}$$

ε_0	vacuum permittivity
a	radius of the particle
ε_1	dielectric constant of the plasmon material
ε_2	dielectric constant of the surrounding media

At the resonance, $\alpha(\omega)$ has its maximum, what is fulfilled when the denominator of Eq. (2.2) has a minimum. For the case of small or little changing imaginary dielectric constants the resonance condition can be simplified to the "Fröhlich criterion":

$$\mathrm{Re}\,\varepsilon_1(\omega) = -2\varepsilon_2 \tag{2.3}$$

This criterion clearly shows the direct dependence of the resonance frequency on the dielectric constant of the environment. Additionally, the polarizeability α depends on the material and the shape of a particle, and has to be calculated to predict the particle properties, i.e. scattering or absorption.[MAI07, NOV06]
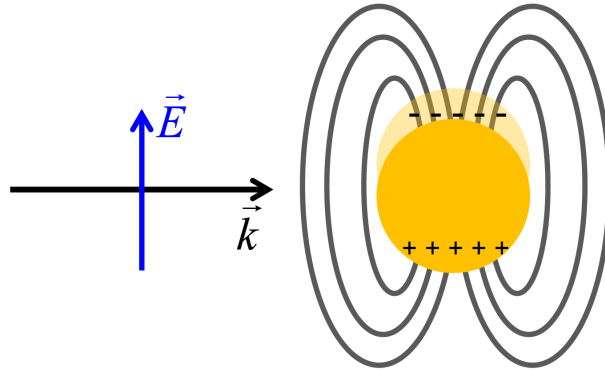
Figure 2: Illustration of the excitation of a particle plasmon in a gold sphere by a linearly polarized plane wave (blue: $\vec{E}$ field, black: propagation direction $\vec{k}$ of the wave). The electrons are shifted towards the cores, polarizing the particles and building up a dipolar field.

2.1.3. Coupling of particle plasmons

At close proximity, the energy of the particle plasmon can be transferred from one particle to the other, so that they cannot be seen as independent particles anymore. This coupling of the two particles leads to a change of the resonance behavior of every particle towards a collective behavior. For particle spacing $r \ll \lambda$ the wavelength shift caused by the coupling follows a r^{-3} dependence, matching the assumption, that small particles are acting like a point-dipole.[MAI07] The field at one particle is composed of the incident field $\vec{E}_0$ and the fields emitted by the surrounding particles. For the contribution of the surrounding particles not only the r^{-3} dependence has to be considered, but also the

relative orientation of the dipoles toward each other. The field $\vec{E}$ that excites one dipole is the sum of the incident field $\vec{E}_0$ and the field of the neighboring dipole $\vec{\mu}$ [JAI10]:

$$\vec{E} = \vec{E}_0 + \frac{\xi\vec{\mu}}{4\pi\varepsilon_0 r^3} \qquad\qquad (2.4)$$

ξ orientation factor

$\vec{\mu}$ dipole momentum

If the coupling occurs perpendicular to the connecting axis, a slight blue shift of the resonance wavelength is observable (see Figure 3a). Here the two dipoles of the particles are parallel aside each other, so that the positive and the negative partial charges of each particle are in vicinity. The repulsive force of these charges now increases the energy needed to excite the plasmons. (see Figure 3a). For coupling along the connecting axis of the particles, a red shift in the resonance wavelength can be observed. In such a configuration, the single particles are acting like one long particle, where all the dipole moments are supporting each other (see Figure 3b). [JAI10, MAI07]
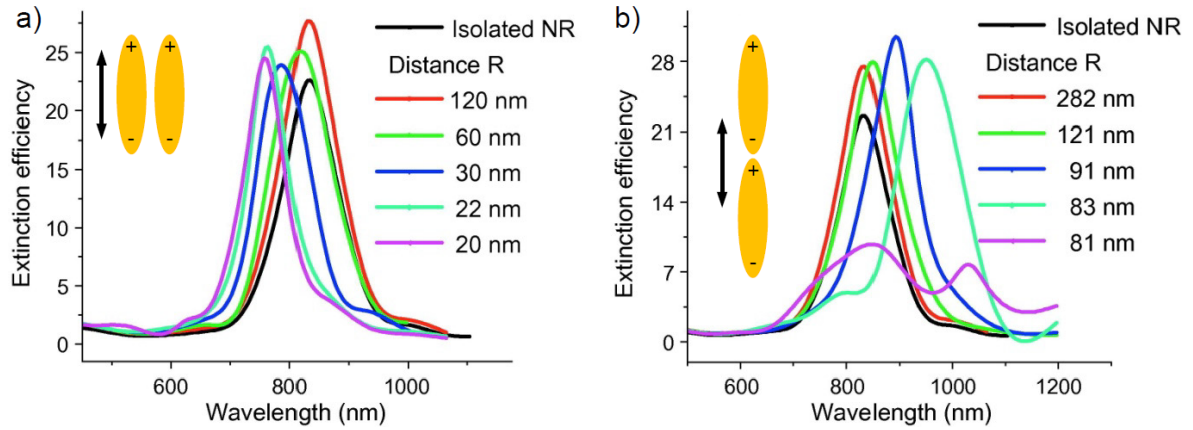

Figure 3: Resonance shift for two coupled gold nano rods. a) The coupling occurs perpendicular to the connection axis leading to a blue shift in the resonance wavelength. b) A coupling along the connection axis results in a considerable red shift of the resonance wavelength. Adapted from [JAI10].

2.2. Gold luminescence

In 1969 Mooradian reported the photoluminescence of noble metals at visible wavelengths. He used a 488 nm Ar-ion laser to excite planar, bulk gold, copper and gold-copper alloy surfaces. However, due to very fast non-radiative relaxation processes, the reported gold bulk luminescence has a very low quantum efficiency of 10^{-10}.[MOO69] Although the luminescence of noble metals is a surface process, it was found that by decreasing the size of the gold towards rough surfaces as well as towards nano particles an increase in the quantum yield up to 10^{-4} is observable.[BOY86, TCH11] Looking at the band structure of gold, the bands involved in the luminescence process are the 5d and the 6sp band.[BEV03]

The photoluminescence of gold could be further divided in two categories: the luminescence with a linear response to the excitation power, also called the one-photon luminescence and the luminescence with a non linear response to the excitation power, the two -, three -, … photon luminescence. The multi photon luminescence can only be observed by excitation with a pulsed laser with high pulse powers. These short pulses excite non-equilibrium electron hole pairs which can recombine by emitting luminescence blue shifted towards the excitation wavelength.[BIA12]
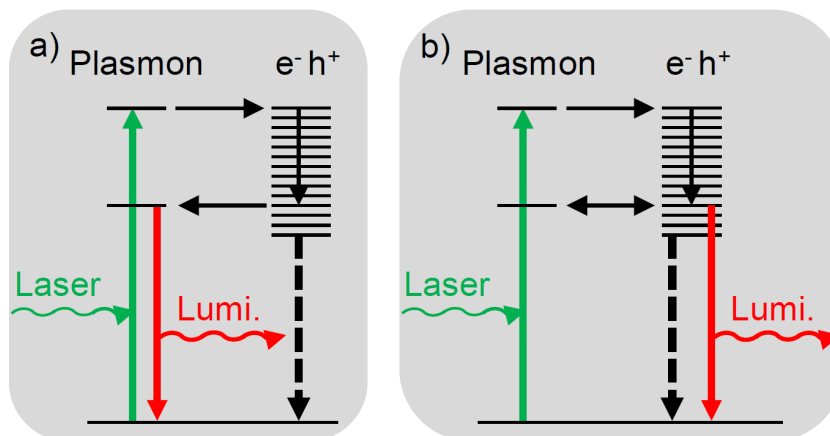
Figure 4: Two possible mechanisms of the plasmon enhanced gold luminescence: a) A photon excites a plasmon that decays into an electron-hole pair (exciton). The exciton can lose its energy, i.e. to the lattice, and after that re-excite a plasmon which emits the luminescence. b) Again the primary excited plasmon decays into an exciton, which looses energy. Here the exciton emits luminescence, which is enhanced according to its energy by the plasmon bands of the structure.

Under cw illumination only the one-photon luminescence is observable. The origin of this luminescence is still a matter of active research where two models are discussed (see Figure 4). In the first model, the excitation light source excites a plasmon or an electron hole pair which can lose its energy, i.e. by scattering partly to the phonon lattice. The electron hole pair with less energy recombines by emitting a new plasmon, which directly decays radiatively.[DUL04] In the second model an interband electron hole pair recombination enhanced by the spectrally overlapping plasmon field leads to the enhanced luminescence in gold nano particles.[MOH00]

In general, the luminescence of gold nano objects excited with visible light has a linear dependence with respect to the power of the excitation source.[TCH11] This leads towards a broad range of applications of gold nano structures, i.e. as luminescent markers in biological applications [WAC12] or as luminescent near field probes [JAE13].
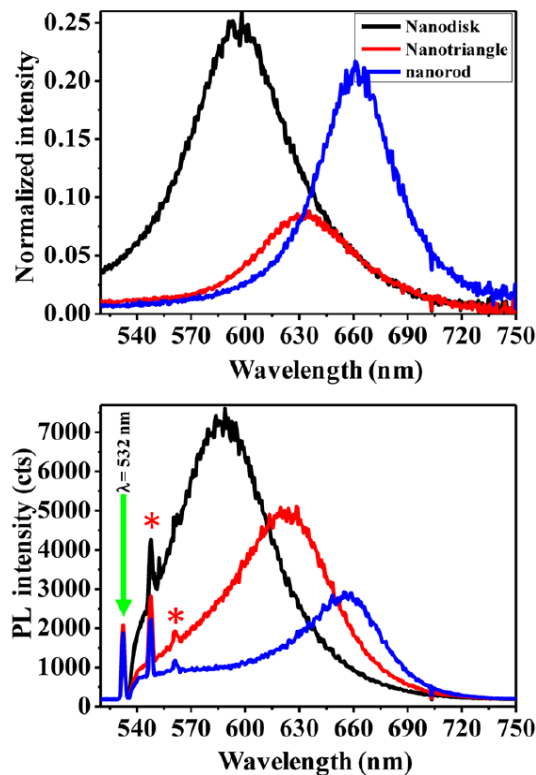
Figure 5: Scattering (top) and luminescence spectra (bottom) of a single gold nano disc (black), nano triangle (red) and nano rod (blue). The maxima of the luminescence and the scattering spectra are at the same wavelengths. Note the signal for the nano rod between 540 nm and 570 nm which is much higher compared to the background intensity found e.g. at 750 nm. Here, the gold luminescence does not overlap with a plasmon band, causing a background that is close to the bulk gold luminescence. The excitation wavelength is marked with 532 nm (green arrow), while the sharp peaks marked with a red star are Raman scattering peaks of the Si/SiO$_2$ substrate. Taken from Ref. [HU12].

The one-photon luminescence is, in both models, coupled to the plasmon bands of the nano structure. Here the plasmon resonance of a gold structure acts as enhancement factor for the luminescence spectrum of bulk gold. Depending on the excitation wavelength, the shape of the luminescence spectrum is similar to the shape of the scattering spectrum of the nano structure (see Figure 5).[FAN12, HU12, STE08, TCH11, YOR12]

2.3. Confocal microscopy

In conventional or wide-field light microscopy, the whole sample area is illuminated by a light source, so that the observed image of the sample is acquired at once. While getting nice fast overview images of a sample, the possibilities of acquiring spectroscopic information like lifetimes or spectra of the sample are limited. For this purpose a point by point acquisition of the optical information like in a confocal microscope is beneficial.
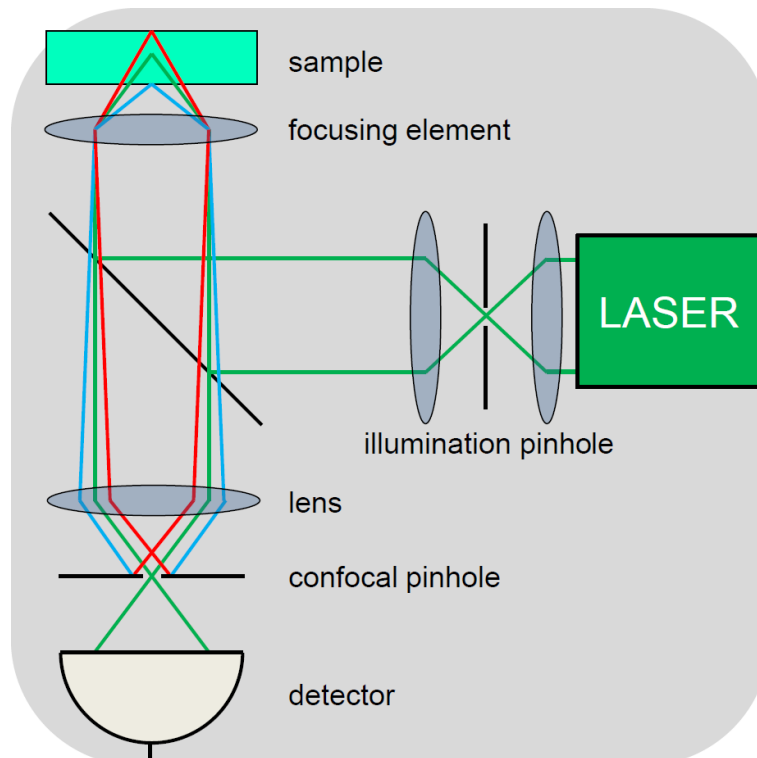

Figure 6: Scheme of a confocal microscope. The excitation beam from the laser is focused by the focusing element into the sample. The signal of the focal spot is collected by the same element and then focused through the confocal pinhole towards the detector (green rays). Signals emerging out of the focal plane (red and blue rays) are blocked by the confocal pinhole in front of the detector.

The confocal microscope was invented in 1957 by Marvin Minsky and the principle is illustrated in Figure 6.[MIN57] In confocal laser scanning microscopy the sample is illuminated by a laser beam via the focusing element, which is usually an objective lens but can also be a parabolic mirror.[LIE01] Here the laser is focused to a diffraction limited spot. The light emitted/scattered by this sample area is collected by the same focusing element and focused through a pinhole, positioned confocally with the focus of the focusing element, serving as a spatial filter blocking light emitted from outside of the focal area. By raster scanning the sample in two- or three directions 2D or 3D images can be acquired with enhanced contrast.

In a confocal microscope the lateral resolution r is, like in all diffraction limited techniques such as the conventional microscopy, given by the Rayleigh criterion [RAY96]:

$$r = 1.22 \cdot \frac{\lambda_0}{2 \cdot n \cdot \sin \theta}$$
(2.5)

λ_0 the vacuum wavelength of the incident light

n the refractive index of the medium

θ the half opening angle of the focusing element

The advantage of the confocal microscope is the enhanced axial resolution that is increased by the confocal pinhole, cutting off the out of plane light. Second, this discrimination of the desired light of the focal area to the light emitted by the surrounding area additionally leads to an enhanced contrast or low background in the recorded images.

2.4. Near-field microscopy

Several ways of beating the diffraction limit have been developed over the last years. Some of them like STED or PALM/STORM are purely optical techniques and are categorized as far field techniques, like confocal microscopy. Here, only the information of the object radiated into the far-field is recorded. Another way of breaking the diffraction limit utilizes sharp, optically active tips that are scanned over the sample at very close distances. These tips interact with the not radiating evanescent field of a sample and can

make this near-field information accessible. The lateral as well as the axial resolution is then improved to the size of the tip apex.

What is the difference between far-field and near-field? This can be illustrated by looking onto the time independent part of a monochromatic electric field $\vec{E}(x,y,z)$ in a Cartesian coordinate system, which is propagating in z-direction inside a source-free region, according to[BRA07, NOV06]. While $z=0$ is the location of the sample with a size smaller than the wavelength.

$$\vec{E}(x,y,z)=\frac{1}{2\pi}\int_{-\infty}^{+\infty}\int_{-\infty}^{+\infty}\vec{\tilde{E}}(k_x,k_y;z)\cdot e^{i(k_x\cdot x+k_y\cdot y)}dk_xdk_y \qquad (2.6)$$

k_x, k_y \qquad\qquad real spatial wave vectors

$\vec{\tilde{E}}(k_x,k_y,z)$ \qquad\qquad two dimensional Fourier spectra

The electric field has to satisfy the Helmholtz equation, where the wave vector is $k=\frac{2\pi}{\lambda}$:

$$\nabla^2\vec{E}(x,y,z)+k^2\vec{E}(x,y,z)=0 \qquad (2.7)$$

$$\nabla=\frac{\partial}{\partial x},\frac{\partial}{\partial y},\frac{\partial}{\partial z}$$

By developing the Fourier components of $\vec{\tilde{E}}(k_x,k_y,z)$ in z-direction, the Helmholtz equation (2.7) with the electric field of equation (2.6) leads towards a second order differential equation:

$$\frac{d^2}{dz^2}\vec{\tilde{E}}(x,y,z)+k_z^2\vec{\tilde{E}}(x,y,z)=0 \qquad (2.8)$$

With

$$k_z=\sqrt{k^2-\left(k_x^2+k_y^2\right)} \qquad (2.9)$$

a general solution of the equation (2.8) can be written as:

$$\vec{\tilde{E}}(k_x,k_y,z)=A_1(k_x,k_y)\cdot e^{+i(k_z\cdot z)}+A_2(k_x,k_y)\cdot e^{-i(k_z\cdot z)} \qquad (2.10)$$

where A_i are arbitrary functions of (k_x, k_y). In A_1, the + in the exponent indicates the propagation direction of this wave into the half space in $z > 0$, while the - in the exponent of A_2 defines the propagation direction to the $z < 0$ half-space. If we set the source of the electric field inside of $z \leq 0$ and consider only $z > 0$ as propagation direction, equation (2.6) together with equation (2.10) is:

$$\vec{E}(x,y,z) = \frac{1}{2\pi} \int\limits_{-\infty}^{+\infty} \int\limits_{-\infty}^{+\infty} A_1 \cdot e^{i(k_z \cdot z)} \cdot e^{i(k_x \cdot x, k_y \cdot y)} dk_x dk_y \qquad (2.11)$$

Here the integrand can also be written in the form $A \cdot e^{ikr}$, with $k = (k_x, k_y, k_z)$ and $r = x + y + z$, leading the statement of equation (2.11) as a spectrum of plane waves with the amplitude A.

To distinguish between far and near field, we look at the field distribution in the x, y-plane at $z = 0$, $\vec{E}(x,y,0)$. Therefore we place a field probe at a distance $z = d$. As boundary conditions we set the Fourier spectra $\vec{\tilde{E}}(k_x, k_y, d)$ at $z = 0$ to $\vec{\tilde{E}}(k_x, k_y, 0)$ and for $z = \infty$ we have $\vec{\tilde{E}}(k_x, k_y, d) = 0$ so the field fades away. Now we get for the Fourier component:

$$\vec{\tilde{E}}(k_x, k_y, d) = \vec{\tilde{E}}(k_x, k_y, 0) \cdot e^{i(k_z \cdot d)} \qquad (2.12)$$

After reverse transformation the field distribution for $z = 0$ is obtained:

$$\vec{E}(x,y,z) = \frac{1}{2\pi} \cdot e^{i(k_z \cdot d)} \int\limits_{-\infty}^{+\infty} \int\limits_{-\infty}^{+\infty} \vec{\tilde{E}}(k_x, k_y, 0) \cdot e^{i(k_x \cdot x + k_y \cdot y)} dk_x dk_y \qquad (2.13)$$

Equation (2.9) shows, that the values of k_z could be real as well as imaginary. For an imaginary k_z, the amplitude in equation (2.13) has an exponential decay with a decay length smaller than the wavelength. Therefore, these waves cannot propagate in z-direction and are called evanescent waves, i.e. the near field.

For real values of k_z, the Fourier components are propagating, plane waves, i.e. the far field. Their part of the field distribution is bigger than $1/k = \lambda/2\pi$, converging to the diffraction limit of a classical microscope.

2.5. Cylindrical Vector Beams (CVB)

The intensity and polarization profile of the beam emitted by a laser depends on the quality of its resonator. In most cases a pure linear polarized Gaussian distribution is desired, also known as the fundamental resonator mode. Besides of this fundamental mode, several other modes are possible like the cylindrical vector beams (CVB) or more specifically radially and azimuthally polarized doughnut modes (RPDM and APDM).

The generation and interaction of electric and magnetic fields with matter is generally described by the Maxwells equations. By assuming a homogeneous and isotropic medium in a field- and charge-free space, the wave equation derived from the Maxwell equations is:

$$\nabla^2 \psi - \frac{1}{c^2} \frac{\partial^2 \psi}{\partial t^2} = 0 \tag{2.14}$$

ψ \qquad wave function

c \qquad speed of light in vacuum

The wave functions as solutions of the wave equation (2.14) are a sum of space- and time dependent functions:

$$\psi = E(x, y, z, t) = \sum a(\omega) u(x, y, z) e^{i(kz - \omega t)} \tag{2.15}$$

ω \qquad angular frequency

x, y, z \qquad spatial coordinates

Combined with the wave equation (2.14) and $k = \left(\dfrac{\omega}{c} \right)$, this wave function leads to a partial differential equation, the Helmholtz equation:

$$\nabla^2 E(x, y, z, t) - k^2 E(x, y, z, t) = 0 \tag{2.16}$$

For the case of monochromatic light, the solution for the electric field of a paraxial beam in Cartesian coordinates is:

$$E(x, y, z, t) = u(x, y, z) e^{i(kz - \omega t)} \tag{2.17}$$

By using the slowly varying envelop approximation

$$\frac{\partial^2 u}{\partial z^2} \ll k^2 u \ , \qquad \frac{\partial^2 u}{\partial z^2} \ll k\frac{\partial u}{\partial z} \tag{2.18}$$

and a separation of the variables in x and y, the Hermite-Gauss (HG_{mn}) modes are derived in the form of:

$$u(x,y,z) = E_0 H_m\left(\sqrt{2}\,\frac{x}{w(z)}\right) H_n\left(\sqrt{2}\,\frac{y}{w(z)}\right)\frac{w_0}{w(z)}\,e^{-i\varphi_{mn}(z)}\,e^{i\frac{k}{2q(z)}r^2} \tag{2.19}$$

With $H_m(x)$, the Hermite polynoms that are a solution to the differential equation

$$\frac{d^2 H_m}{dx^2} - 2x\frac{dH_m}{dx} + 2mH_m = 0 \tag{2.20}$$

and: E_0 constant electrical field amplitude

                     $w(z)$ beam size

                     w_0 beam waist size

$\varphi_{mn}(z) = (m+n+1)\tan^{-1}\left(\dfrac{z}{z_0}\right)$ Gouy phase shift

              $q(z) = z - iz_0$ complex beam parameter, with

               $z_0 = \dfrac{\pi w_0}{\lambda}$ Rayleigh range

The fundamental Gaussian beam is the solution of Eq. (2.19) with $m = n = 0$ is written as:

$$u(x,y,z) = E_0\frac{w_0}{w(z)}e^{-i\varphi_{mn}(z)}e^{i\frac{k}{2q(z)}r^2} \tag{2.21}$$

The same derivation can be made in cylindrical coordinates instead of Cartesian coordinates, starting with the general solution for the Helmholtz equation (2.16):

$$E(r,\phi,z,t) = u(r,\phi,z)e^{i(kz-\omega t)} \tag{2.22}$$

By applying this as initial point to the slowly varying envelop approximation the Laguerre-Gauss (LG_{pl}) modes are derived by separation of the variables in r and ϕ:

$$u\left(r,\phi,z\right)=E_0\left(\sqrt{2}\,\frac{r}{\omega}\right)^l L_p^l\left(2\frac{r^2}{\omega^2}\right)\frac{w_0}{w(z)}\,e^{-i\varphi_{pl}(z)}\,e^{i\frac{k}{2q(z)}r^2}\,e^{il\phi}\tag{2.23}$$

with $L_p^l(x)$, the corresponding Laguerre polynomials that are a solution to the differential equation:

$$x\frac{d^2 L_p^l}{dx^2}-(l+1-x)\frac{dL_p^l}{dx}+pL_p^l=0\tag{2.24}$$

and for the Gouy phase shift $\varphi_{pl}(z)=(2p+l+1)\tan^{-1}\left(\dfrac{z}{z_0}\right)$.

The fundamental Gaussian beam is one solution of the Laguerre-Gauss mode with $l = p = 0$.[NOV06, SIE86, ZHA09] Intensity plots of the first four fundamental HG modes are drawn in Figure 7. In principle the numbers of m and n are representing the number of horizontal and vertical knots in the mode structure, respectively.
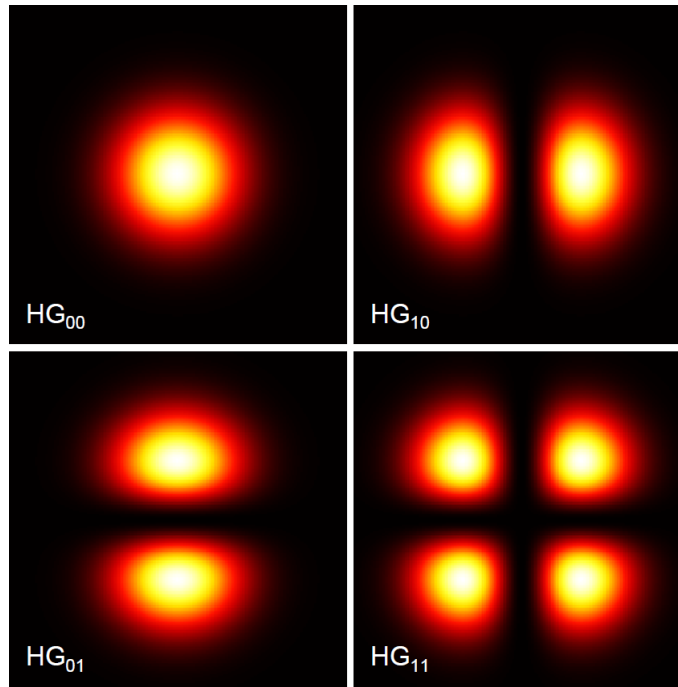

Figure 7: Intensity plot of the first four Hermite-Gauss beams, showing the system in their nomenclature. The n-value, order of the beam, represents the number of vertical knots of the mode, while the m-value, degree of the beam, represents the number of horizontal knots of the mode. Due to the different coordinate systems, this correlation is not valid for the Laguerre-Gauss beams.

By superposition of different HG_{nm}- or LG_{nm}-beams, all possible laser beams can be described. Intrinsically, the Hermite-Gauss and Laguerre-Gauss modes are scalar fields where the polarization of a beam isn't taken into account. To gain access to the polarization information of a beam, the full wave equation for the electric field has to be used.[ZHA09] This consideration leads e.g. to the expressions (2.25) and (2.26), where the already named CVBs can mathematically be constructed using the HG_{01} and HG_{10} beams. The polarization of the corresponding modes is established by multiplying the scalar HG modes with a unity vector in x or y direction.

$$\text{RPDM} = HG_{10} \cdot \vec{n}_x + HG_{01} \cdot \vec{n}_y \tag{2.25}$$

$$\text{APDM} = -HG_{01} \cdot \vec{n}_x + HG_{10} \cdot \vec{n}_y \tag{2.26}$$

$\vec{n}_x, \vec{n}_y$ unity vectors to polarize the scalar fields

Note: In some literature, the equation for the construction of the APDM contains an error concerning the minus before the HG_{01}. This error would lead to a mode with polarization vectors pointing at each other.

2.6.   Calculation of focal fields

For the use in microscopy, the fields of different laser beams in the focus of an objective lens should be known. Especially the previously introduced CVBs express unique fields in the focus of a high NA objective lens or parabolic mirror.

A method to calculate the fields in the focus of an objective lens, which also takes the polarization into account, was introduced by Wolf and Richards for a focused Gaussian beam in 1959[RIC59] and was adapted to CVBs by Youngworth and Brown in 2000[YOU00]. In 2001 Lieb et al. modified this method to calculate the fields in the focus of a high NA parabolic mirror.[LIE01a]

In principle, in this method the focusing element (objective lens or parabolic mirror) transforms the incoming planar wave front into a spherical wave with a sphere radius corresponding to the focal length f. In the focal volume, the electric field of a point with the cylindrical coordinates $P(\rho, \varphi, z)$ is:

$$\vec{E}(\rho,\varphi,z) = -\frac{ikf}{2\pi} \int\limits_{0}^{2\pi} \int\limits_{0}^{\theta_{max}} \vec{E}_f(\theta,\phi) e^{iksz} \sin\theta d\theta d\phi \qquad (2.27)$$

By integration over the whole focal volume, the complete field distribution can be calculated. The NA of the focusing element is related to θ_{max} with $NA = n \cdot \sin\theta_{max}$. A scheme of the method is shown in Figure 8:
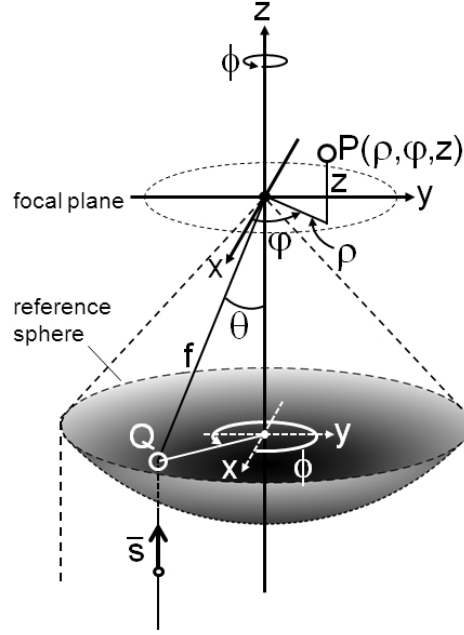
Figure 8: Scheme of the coordinate system used to calculate the fields in a focus based on Eq. (2.27). At the point Q, the electric field $\vec{E}_f(\theta,\phi)$ is given by the radius f of the reference sphere, as well as the incident angle θ and the relative angle ϕ. Every point P is defined in cylindrical coordinates by the angle φ and lengths ρ and z. Taken from Ref. [JAE13a].

The resulting fields are not only depending on the used laser beam and the type of focusing element, they also depend on the index of refraction of the medium inside of the focal volume, e.g. at surfaces.

In general, when focusing the RPDM at high geometrical NA's, it expresses a strong electric field polarized in the propagation direction of the beam, also called longitudinal polarization or z-polarization. This longitudinal polarized field has a center symmetric energy distribution as plotted in Figure 9a. This longitudinal polarized field has a diffraction limited spot size of approx. $\lambda/2$, depending on the NA. It is surrounded by a radially, in plane polarized ring or doughnut shaped field which is, depending on the NA of

the focusing element, usually weaker than the longitudinal polarized component (Figure 9a). In the focus of the APDM the azimuthally polarized fields are exclusively in plane, while keeping the doughnut shape of the beam (Figure 9 b). The size of the APDM focus, depends on the NA and is approx. λ .[NOV06, RIC59, WOL59]

The program "focused fields" written by Andreas Lieb is capable to calculate the optical fields in the focus of objective lenses and parabolic mirrors.[LIE01] It was used to calculate all the focal fields needed for this thesis.
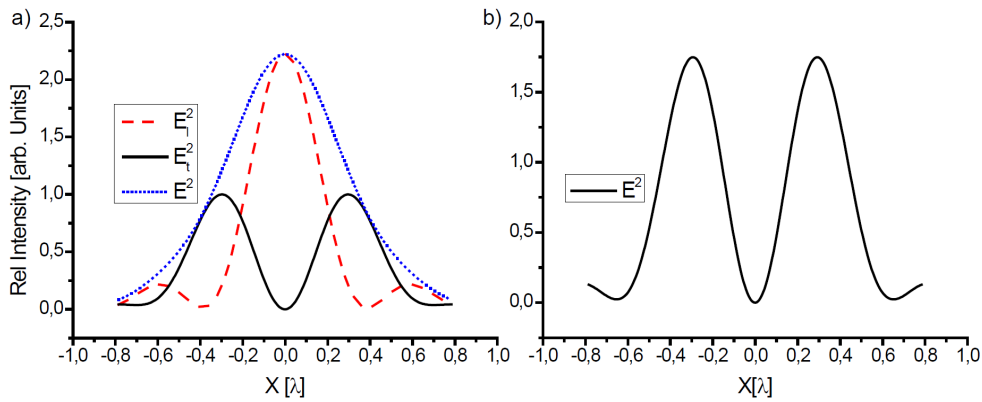
Figure 9: Electric field distribution in the foci of the RPDM (left) and APDM (right) for an oil immersion objective lens with an NA of 1.25 at a wavelength of 632.8 nm at a glass-air interface. At these conditions, the longitudinal field (red dashed line) of the RPDM is approx. 2.5 times higher than the transversal field (black solid line). In the focus of the APDM only a transversal field can be found. E_t^2 : transversal field, E_l^2 : longitudinal field, $E^2 = E_t^2 + E_l^2$

3. Instrumentation

3.1. Confocal microscopes

The experimental work presented in this thesis was performed with two different types of home build confocal microscopes. One microscope uses objective lenses as focusing element and is denoted as OL-setup. The other microscope uses a parabolic mirror as focusing element and is denoted as PM-setup. Common to both setups is:

- the use of a mode conversion to create the APDM or RPDM and
- the substitution of the confocal pinhole by a detector with an active surface size of the pinhole.

3.1.1. OL-setup

Two different OL-setups, both are inverted confocal microscopes, have been used. One of the setups has the additional capability to support a module for near field optical microscopy (setup A), while the other has the advantage of using different laser wavelengths (setup B).

Setup A uses a 632.8 nm HeNe Laser as excitation source. The laser beam is converted into the APDM / RPDM by a four quadrant $\lambda/2$-wave plate mode-converter.[DOR03] After passing a 50:50 non polarizing beam splitter, the excitation beam is focused by an oil immersion objective (Zeiss, CP-ACHROMAT 100x, NA: 1.25) lens onto the sample. To scan the sample through the focus a 3 axis piezo scanning table (Physik Instrumente, P-517.3CL) is used. The signal from the sample is collected with the same objective, and after passing the 50:50 non polarizing beam splitter, the signal is either directed via a flipping mirror to avalanche photo diodes (Perkin Elmer, SPCM-AQR-14, abbr. APD) for imaging or to a spectrometer (Princeton Instruments, Acton SP 300i) equipped with a CCD (charge coupled device)-detector (Princeton Instruments, SPEC-10). Before the APDs, the signal is again divided by a 50:50 non polarizing beam splitter. One APD detects the elastic scattered light of the sample, using 5OD neutral density filter to reduce the intensity of the beam. The second APD is used to detect the luminescence signal selected by a 633 nm long pass filter (Semrock, RazorEdge LP633RU). The whole instrument is controlled by an SPM 100 (RHK Technology) controller and the corresponding software

(XPMPro 2.0). In addition a home build near-field module, with shear force controlled feedback, can be attached on top of the microscope and is further described in section 3.2.

The differences of setup B are in the laser sources, the mode conversion part and a different controller. As laser sources two lasers can be used:

- HeNe-laser, $\lambda = 632,8$ nm
- Ar/Kr-laser with several wavelengths between 450 nm and 647 nm (Coherent Inc., Innova 300)

As the excitation wavelengths can vary, the respective filter sets for the observation of luminescence signals are adapted accordingly. The mode conversion is performed by a liquid crystal polarization converter (Arcoptix, Radial-Azimuthal Polarization Converter), which can be adjusted freely to wavelengths between 350 nm and 1700 nm.[STA96] Setup B is controlled by a home build software based on LabView and electronic components of National Instruments and therefore lacks the ability to support the near-field module used in setup A.

3.1.2. PM-setup

The third setup is a combined confocal and near field optical microscope based upon a parabolic mirror as focusing element.[SAC08] The NA of the parabolic mirror is 0.9995 corresponding to a maximum focusing angle of nearly 90°. Due to geometrical restrictions, it is not possible to achieve these high focusing angles with a lens based microscope. Another advantage of a parabolic mirror is the lack of chromatic aberrations,which is the result of the reflective, instead of a refractive like in lens based focusing, working principle,.

The beam path is similar to the beam path of setup A, where after the mode conversion, the beam diameter is adapted to the aperture of the parabolic mirror. In the collection beam path, the PM setup utilizes a single APD as well as a spectrograph (Princeton Instruments, Acton SP 300i) with coupled CCD camera (Princeton Instruments, SPEC-10) for the study of luminescence signals. To support a near-field module, this setup is also equipped with SPM 100 controller like setup A.

3.1.3. Mode conversion

For the conversion of a linear polarized Gaussian beam into the RPDM/APDM, the polarization has to be turned for a specific value at each point in the beam. This can be done with specially cut and realigned $\lambda/2$-wave plates as shown in Figure 10b.[DOR03] When a collimated, linear polarized laser beam passes this mode converter, the polarization in each quadrant is turned according to the orientation of the fast axis of the corresponding wave plate. After the mode converter, the laser beam already possesses a radial or azimuthal polarization but the intensity profile still has a Gaussian shape. To acquire the RPDM or APDM, the beam is focused through a pinhole, working as a spatial filter.
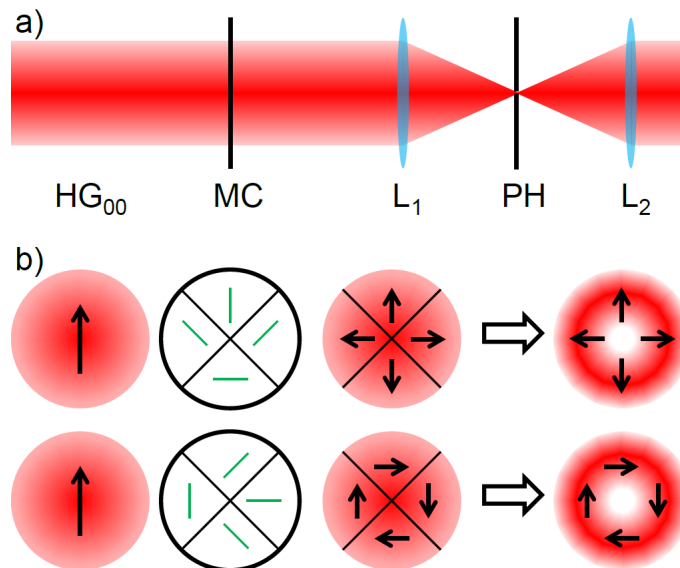
Figure 10: Schematic drawing of the mode conversion technique according to [DOR03]. a) A linear polarized Gaussian beam (HG$_{00}$) is transmitted through the mode converter (MC) and then focused through a pinhole (PH) as a spatial filter. L$_1$ and L$_2$ are the lenses of the spatial filter. b) Cross sections through the laser beam at the positions HG$_{00}$, L$_1$ and L$_2$ (red) where the polarization states are given by the black arrows. The cross section of the mode converter is also given (black-white circle with green lines). The green lines are indicating the fast transmission axis of the individual $\lambda/2$-wave plate quadrant inside the mode converter.

Unfortunately the $\lambda/2$-wave plates can only be used for one wavelength. If different wavelengths are in use, either several of these mode converters or an adjustable liquid crystal mode converter have to be used.[STA96]

3.2. Near-field setup

As shown in section 2.4, the evanescent near field does not propagate in *z*-direction like the far field. To visualize this near field, several techniques based on sharp tips scanned in close proximity over the sample surface, inside the region of the near field, have been developed. Two types of near field probes can be categorized. One is called "aperture probes", where an aperture with a diameter smaller than the wavelength is used. [HEC00] The simplest form of such a probe would be a metal film with a small hole. Other types of aperture probes are silicon AFM probes with a little aperture hole or sharp glass fiber tips where a metal film with an aperture at the apex was manufactured. This probes can be used either to excite the near field, while the response of the sample is measured in the far field, or the excitation is done via the far field and the detection is carried out via the aperture probe. Also the excitation and the detection can be done via the same aperture probe. The resolutions of these kind of probes is limited by their transmission. For an aperture with a diameter of 50 nm a transmission of 10^{-6} is possible, while for an aperture diameter of 20 nm the transmission decreases to 10^{-12}.[NOV06] To circumvent the limitation of the aperture, it is possible to use single emitters at the apex of the tip, increasing the resolution to the size of the single emitter.[KAL01, KUE01, MIC00]
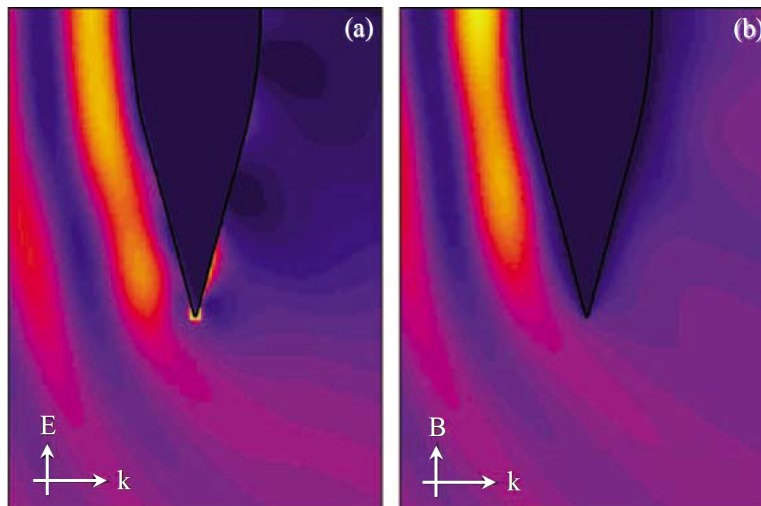
Figure 11: Calculated intensity distribution near a laser-irradiated gold tip. The exciting wave is incident from the left and forms a standing wave pattern as it interferes with the reflected field from the tip shaft, and at the end of the tip, the wave diffracts. Two different excitation polarizations are used. The field-enhancement effect is observed only if the incident wave is polarized along the tip axis (*a*). In the case of an incident wave polarized perpendicular to the tip axis, the field near the tip is attenuated (*b*).Taken from Ref. [NOV06a]

The second type of near-field probes are apertureless probes. These are sharp semiconductor or metal tips acting like an optical antenna and can efficiently scatter energy from the near field to the far field. Due to the freely movable conduction band electrons, near-field tips made of metals can generate their own near field, when the applied optical field to the tip is polarized parallel to the tip's main axis (see Figure 11). The free electrons in the tip are moved by the incoming electric field up and down the tip. Due to the geometry of the tip, the electrons are concentrated at the apex. This effect can be maximized, if the applied optical field is in resonance with the surface plasmons of the tip.

The near field setup used in this thesis utilizes sharp, electro-chemically etched, gold tips while the tip – sample distance control is done by shear force.[NOV06] The tip is mounted at a quartz tuning fork (see Figure 12), acting as a piezoelectric sensor. This tuning fork is excited mechanically by a piezo tube at its resonance frequency, while the amplitude and the phase of the vibration of the tuning fork are measured with the electric signal acquired at the tuning fork. In close proximity to the sample, the tip feels the friction of the surface material, what changes the resonance frequency of the system. This is reflected in the measured signal as a change in the amplitude and the phase. Due to the higher sensitivity, the phase signal is used for the distance control feedback.
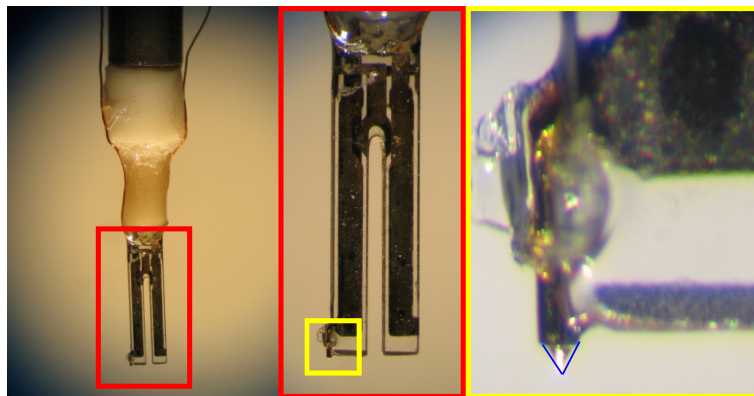
Figure 12: Main part of the near-field module. Left: the tuning fork (red box) is connected by a marcor cylinder (white cylinder) with an x, y, z piezo tube (grey cylinder at the top). The two wires to read out the oscillation signal of the tuning fork are visible left and right of the marcor cylinder and the piezo tube. Middle: magnified image of the tuning fork with attached gold tip (yellow box, magnification right with the tip encircled with a blue V)

4. Experimental section

4.1. Gold posts on glass for imaging comparison

There are several ways to map the intensity distribution of focal fields, all using point like and luminescent objects, i.e. fluorescent beads or quantum dots. But also plasmonic systems can be used to map the focal fields. Their size is much smaller with respect to the size of the focus and so they are matching the condition of a point like object. Second, the scattering cross section of plasmonic objects is much bigger compared to molecules or quantum dots.

The gold posts are manufactured by e-beam lithography by Julia Fulmes of the research group "Plasmonic Nanostructures", University of Tübingen. As substrate, a round, 0.17 mm thick cover slide with a diameter of 5 mm is chosen to fulfill the demands regarding the sample size of the PM- and the OL-microscopes. All posts are 100 nm high and have a diameter of 65 nm. For the needs of the e-beam lithography and to be able to control the structures via SEM, between the glass and the gold structure a 50 nm thin indium tin oxide layer (ITO) is added.

Figure 13: Intensity distributions of a 632.8 nm wavelength APDM in the focus of the four different focusing elements at a glass air interface. The air objective lens (AO) (black solid line), with the smallest NA of 0.75 has the largest diameter of more than 1x λ. The parabolic mirror (PM) (red dashed line) with the high NA of 0.998 in air achieves similar small spots, with focal diameters smaller than 1x λ, like the oil immersion objectives with the NAs of 1.25 (green dotted line) and 1.46 (blue dash dot dot line).

To characterize the focal fields and the imaging capability of the parabolic mirror as well as the air objective lens with NA = 0.75 and the two oil immersion objective lenses with NA = 1.25 and NA = 1.46, the gold posts are scanned through the 632.8 nm wavelength APDM/RPDM foci of these focusing elements. For these focusing elements, the focal fields have been calculated (see Figures 13 and 14). The focal fields of the APDM reflect the symmetry and the polarization of the collimated laser beam, namely a center symmetric doughnut shape and azimuthal (in plane) polarization. The difference of the four focusing elements is in the size of the focal spot which decreases with increasing NA of the focusing element (see Figure 13).
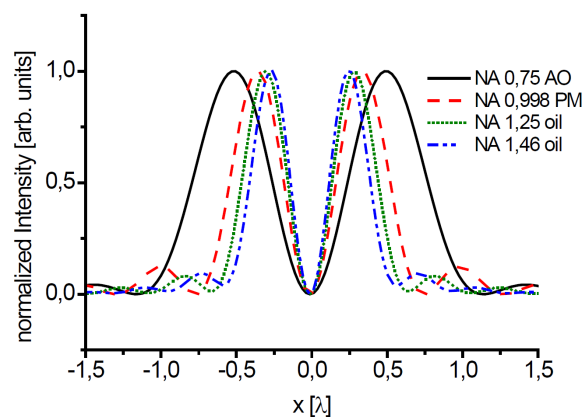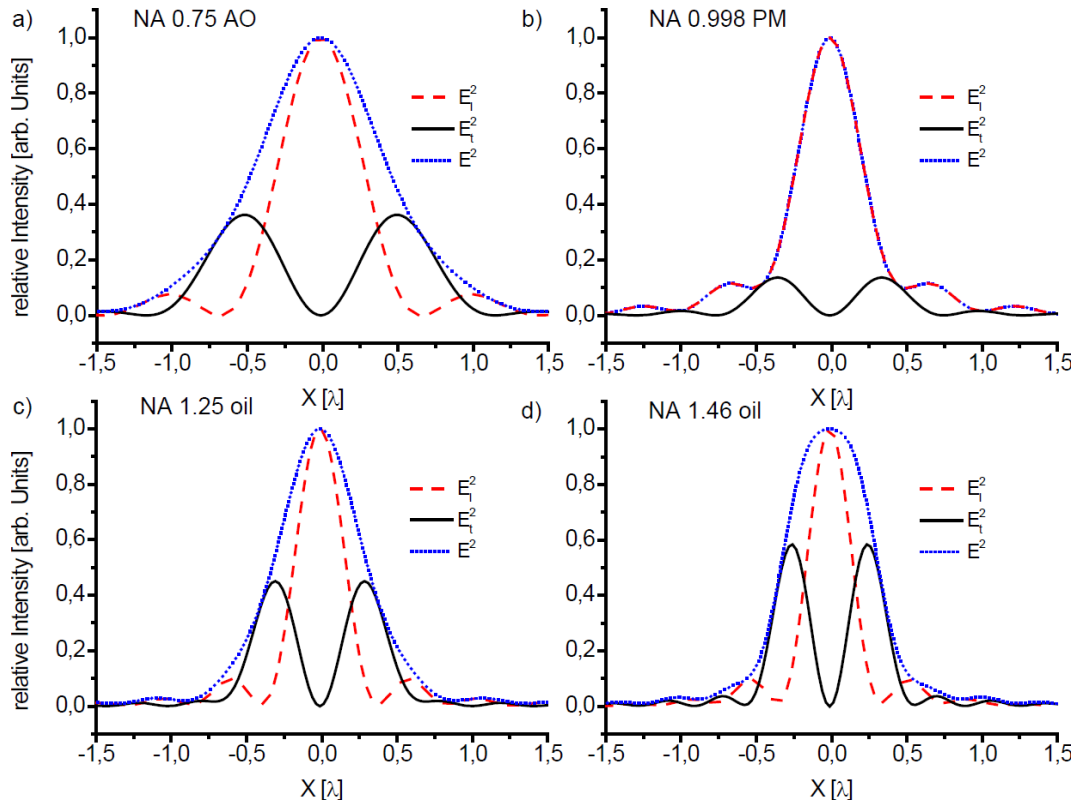

Figure 14: Intensity distributions of a focused 632.8 nm wavelength, RPDM in the focus of different focusing elements at a glass air interface. The longitudinal- or z-field (E_l^2) is plotted as red, dashed line while the black solid line is showing the transversal- or in plane field (E_t^2) in the focus. The sum of both fields ($E^2 = E_l^2 + E_t^2$) is plotted with a blue, dotted line. The single graphs showing the focal fields for a) an air objective lens with an NA of 0.75, b) a parabolic mirror with an NA of 0.998, c) an oil immersion objective lens with an NA of 1.25 and d) an oil immersion objective lens with an NA of 1.46.

For the focal fields of the RPDM, the intensity distributions, normalized to the maximum value, can be found in Figure 14. The air objective lens, like for the APDM in Figure 13, has a larger focus and a comparable high transversal field. In the focus of the other immersion free focusing element, the parabolic mirror, the longitudinal field dominates the field distribution, whereas the transversal component is negligible. Objective lenses with sharper foci are the ones with the NAs 1.25 and 1.46 using oil immersion. By increasing the NA, the foci shrinks, but also the ratio between longitudinal and transversal field is influenced and rises with the NA.

Figure 15 shows the dark field scattering spectra of the gold nano posts, highlighting two resonance wavelengths at 550 nm and at 680 nm. In theory, the long axis of such a post is, compared to the short axis, connected to a more red shifted resonance. This resonance can be found at a wavelength 680 nm. The long axis of the post is standing upright at the sample surface, where it can only be excited by a field polarized in z-direction, like the longitudinal field of the RPDM focus. On the other hand, the diameter of the posts is connected to a blue shifted resonance in respect to the resonance of the long axis. This resonance is found at 550 nm in the dark field spectra and can be linked by the fixed position of the posts to an in plane polarized excitation. This kind of polarization can be found either in the APDM focal field or the transversal component of the RPDM focus.
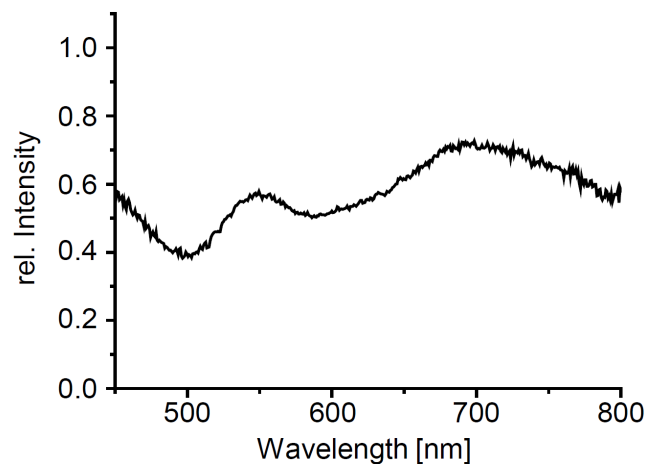

Figure 15: Dark field scattering spectra of 100 nm high and 65 nm in diameter sized gold posts on glass. The main resonance wavelength can be found at 680 nm and the second at 550 nm while below 500 nm the d-band absorption of gold rises.

The resulting confocal scanning patterns generated by excitation of one single post with the APDM are shown in Figure 16a-d. The scan pattern is the result of a convolution of the excitation polarizability of the post in the base plane and the distribution of the electrical field vectors in the focal field (Figure 16e-h). The patterns differ from the corresponding field distribution calculations. Especially a change in the rotationally symmetrical intensity distribution can be observed. As shown in chapter 2.1, the excitation of the dipole in a particle is extremely sensitive to its shape. Slight deviations in the base cross section of a post from the round shape directly influences the resonance of the particle leading towards different absorption cross sections for different excitation polarization directions.

Figure 16: Scan images of one gold post on glass excited with the APDM. The focusing elements are a) an air objective lens with an NA of 0.75, b) a parabolic mirror with an NA of 0.998, c) an oil immersion objective lens with an NA of 1.25 and d) an oil immersion objective lens with an NA of 1.46 (d). The corresponding simulated focal field distributions in the focal plane are shown in e) to h).

The background of the images is influenced primarily by the glass substrate, observed as a wavelike pattern around the posts.[HUS11] To obtain similar maximum intensities, the structures have to be excited with different laser powers (P_{exc}). Data with the excitation power, signal and background intensities as well as the noise level and a signal intensity that is normalized with respect to the excitation power are listed in
Table 1.

APDM	P_{exc}	I_{signal}	$I_{background}$	Noise	$\dfrac{I_{signal} - I_{background}}{P_{exc}}$
NA 0.75 AO	2600 μW	438 kHz	351 kHz	10 kHz	43,5 Hz/μW
NA 0.998 PM	200 μW	45 kHz	30 kHz	4 kHz	75 Hz/μW
NA 1.25 oil	100 μW	765 kHz	600 kHz	17 kHz	1650 Hz/μW
NA 1.46 oil	100 μW	680 kHz	475 kHz	12 kHz	2050 Hz/μW

Table 1: Excitation powers and obtained signal strengths for measurements with different focusing elements for APDM illumination.

Obviously, the techniques with oil immersion (NA 1.25 and 1.46) are collecting more signal compared to the immersion free techniques (AO and PM). The emission properties of the gold luminescence can be seen like the emission properties of a dipole. In this case, the dipole is near a glass surface that is influencing the emission pattern of the dipole. As shown in chapter 2.2, the one-photon luminescence of gold has a linear dependence on the used excitation power. So when the net value of the one-photon luminescence signal emitted by the gold post is divided by the excitation power, a comparable value is derived. The net value of the one-photon luminescence signal is the signal of the post subtracted by the background signal.

The longitudinal field of the RPDM focus is used to excite the long axis of the posts, and has a good overlap of the used laser wavelength and the resonance wavelength of the long axis. Figure 17 shows the confocal scanning images of a gold post in the focus of the RPDM (Fig. 17a - d) together with the field simulations of the total field E^2 (Fig. 17e - h) and the longitudinal field E_l^2 (Fig. 17i - l). The experimental pattern has, due to the good match of the excitation wavelength with the resonance of the long axis, a high similarity with the longitudinal field in the focus.
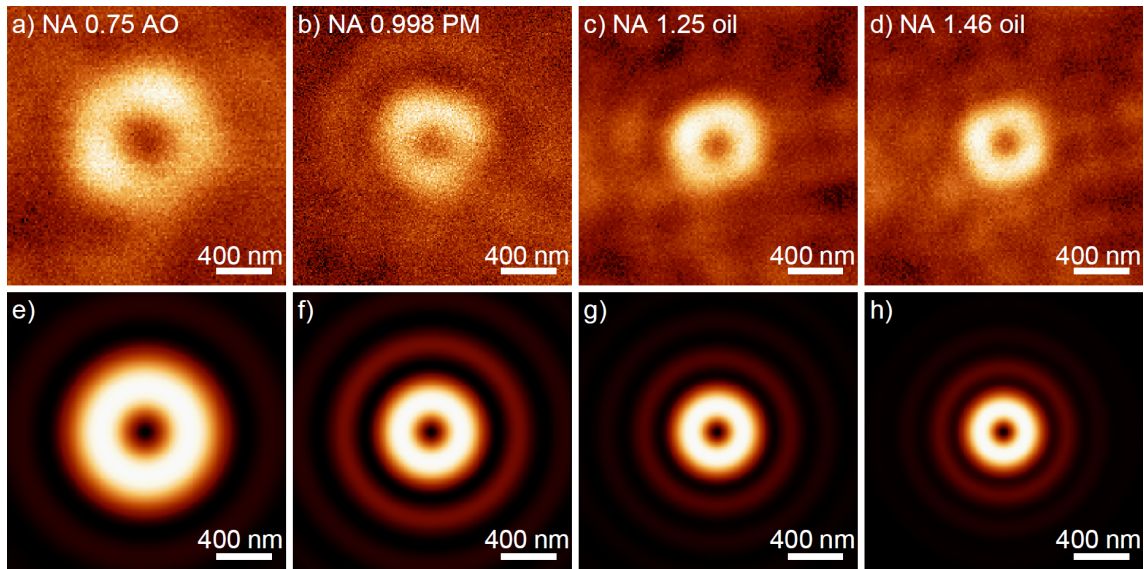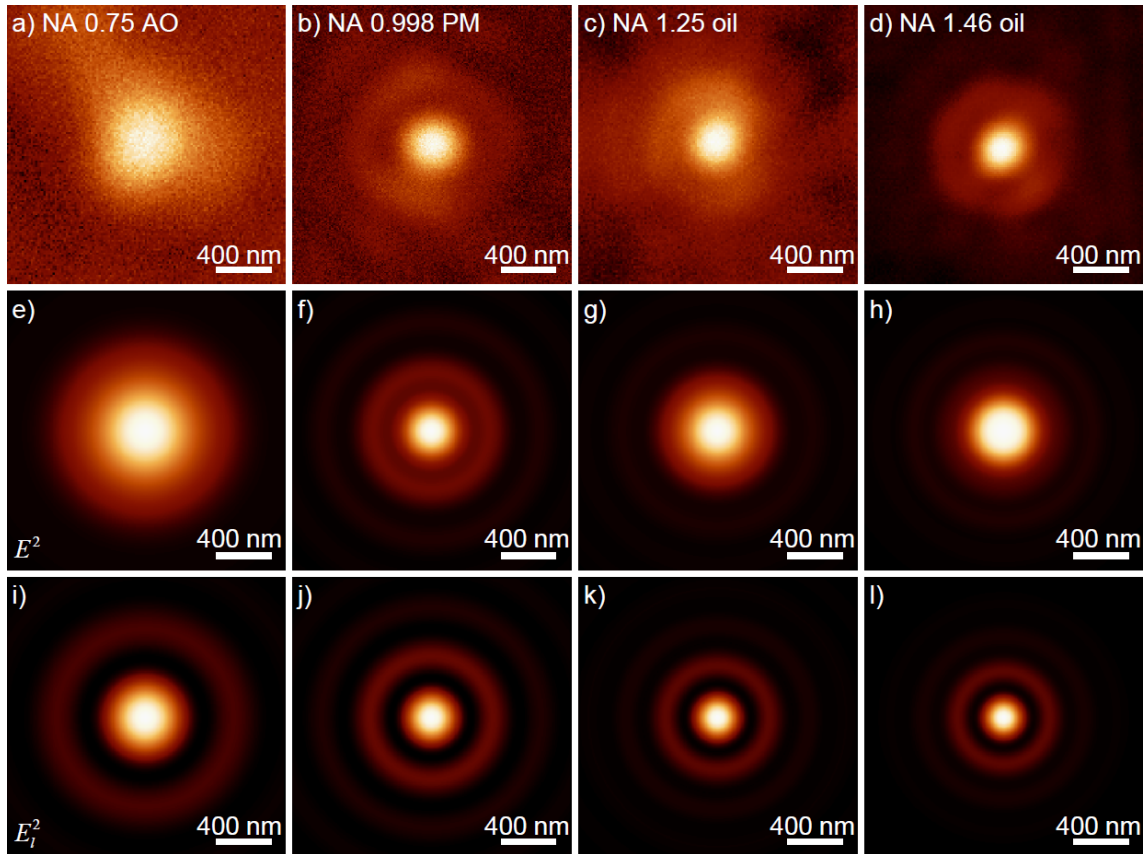
Figure 17: Scan images of one gold post on glass excited with the RPDM. The focusing elements are a) an air objective lens with a NA of 0.75, b) a parabolic mirror with a NA of 0.998, c) an oil immersion objective lens with a NA of 1.25 and d) an oil immersion objective lens with a NA of 1.46. e) to h) shows the corresponding simulated total focal field (E^2) distributions in the focal plane, while in i) to l) only the longitudinal field component of the focal field (E_l^2) is plotted.

Data with the excitation power, signal and background intensities as well as the noise level and a signal intensity that is normalized with respect to the excitation power are listed in

Table 2. The difference between the immersion free and the immersion based focusing elements is more dramatic when using the RPDM. The smaller NA of the air objective lens compared to the parabolic mirror leads to a significant difference in the signal.

RPDM	P_{exc}	I_{signal}	$I_{background}$	Noise	$\dfrac{I_{signal} - I_{background}}{P_{exc}}$
NA 0.75 AO	2600 μW	380 kHz	245 kHz	20 kHz	51,9 Hz/μW
NA 0.998 PM	200 μW	110 kHz	30 kHz	6 kHz	400 Hz/μW
NA 1.25 oil	100 μW	900 kHz	330 kHz	17 kHz	5700 Hz/μW
NA 1.46 oil	100 μW	1400 kHz	320 kHz	15 kHz	10800 Hz/μW

Table 2: Excitation powers and obtained signal strengths for measurements with different focusing elements for RPDM illumination.

The emission profiles of dipoles near planar surfaces are described analytically.[NOV06] Compared to the emission pattern in a homogeneous medium, the change of the refractive index that is taking place at a surface influences the radiation behavior. In this case the dipolar emitter is at the air side of an air–glass interface. The rays directed from the dipole towards the surface are, depending on the angle towards the surface, transmitted and/or reflected. Additionally, the near field of the dipole that penetrates the surface of the glass is also partially transmitted into the far field thus more intensity is transmitted through the glass.

In Figure 18 the ratio between the collected and total radiated energy of a dipole at an air glass interface is plotted against the collection angle of a focusing element like an objective lens or parabolic mirror. The dipole is placed $\lambda/10$ over the interface and is oriented either normal (a) or parallel (b) to the interface. In addition the angles of the four used focusing elements are highlighted by gray (air side) and dark red (glass side) vertical lines. Clearly, placing a collecting optical element at the glass side of this system results in an increase of the detectable signal. This is due to the close distance of the glass to the dipole. At this close distances, the glass leads to a propagation of the near field part of the dipoles emission into the far field.
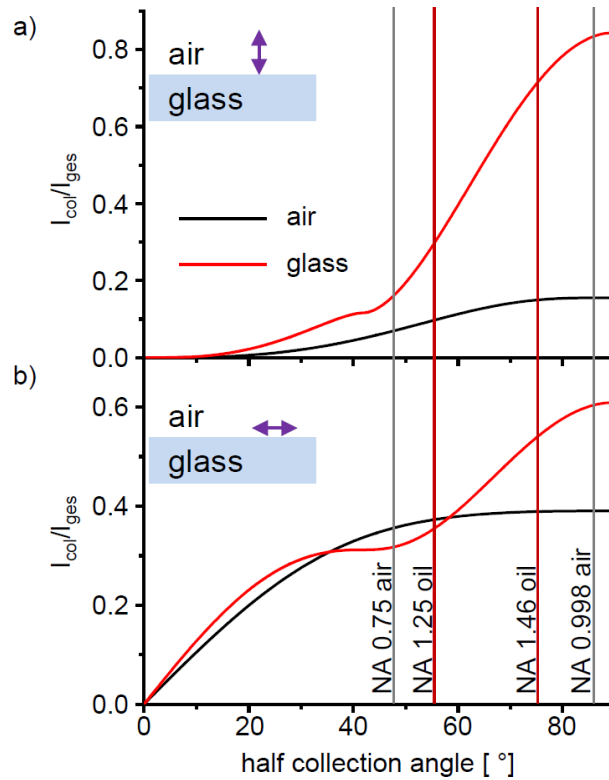
Figure 18: Simulation of an upright standing (a) and a lying dipole (b) at a glass air interface. The ratio between the energy that is collected at the air side or at the glass side and the total radiated energy is plotted versus the half collection angle that ranges from 0° (normal to the glass surface) to 90°. In addition the angles that correspond to the numerical apertures of the used focusing elements are highlighted as gray (for the collection in air) and dark red lines (for the collection in glass).

A direct comparison of the experimental data with the transmission ratios (I_{col}/I_{ges}) of the simulated dipole is given in

Table 3. The values for air and glass collection are varying much stronger for the experimental data. Such a high gain of the signal by collection via the glass cannot be correlated with the properties of a dipole. Interestingly, the values for either air- or glass-side detection are comparable. The difference either between the air lens and the parabolic mirror or between the two oil immersion lenses are matching roughly in the magnitude. Here, minor differences can be explained by the specific transmission characteristics of the single collection elements, e.g. the parabolic mirror has a much better reflectivity compared to the transmittance of the air lens. The big difference between the air- and the glass-side detection relates to the real character of the gold post structure. First of all, between the glass and the gold an ITO layer for conductance is present. For 632.8 nm the refractive index of ITO is 1.94 [LAU98] instead of a refractive index of 1.5 for glass used in the simulation. The higher refractive index of ITO in comparison to glass would lead to a higher transmission ratio for the oil immersion lenses. Second, the gold cone itself

doesn't act like a perfect dipole, while the process to gain one-photon gold luminescence (see chapter 2.2) suggests the simultaneous emission of several dipoles. Additionally, the emission at the interface between the gold structure and the ITO cannot be detected at the air side.

	APDM/parallel Dipole		RPDM/perpendicular Dipole	
	$\dfrac{I_{signal} - I_{background}}{P_{exc}}$	$\dfrac{I_{col}}{I_{ges}}$	$\dfrac{I_{signal} - I_{background}}{P_{exc}}$	$\dfrac{I_{col}}{I_{ges}}$
NA 0.75 AO	43,5 Hz/µW	0.36	51,9 Hz/µW	0.07
NA 0.998 PM	75 Hz/µW	0.39	400 Hz/µW	0.16
NA 1.25 oil	1650 Hz/µW	0.36	5700 Hz/µW	0.32
NA 1.46 oil	2050 Hz/µW	0.55	10800 Hz/µW	0.74

Table 3: Comparison between the excitation power normalized intensities found by measuring single gold posts with the APDM and RPDM with the transmission ratio of the simulated dipole.

4.1.1. Conclusion

Gold nano posts were used to verify the capabilities of different focusing/collecting elements to image emitters on a glass substrate. For a theoretical dipolar emitter, standing upright on the glass surface, the optical element which collects via the glass substrate has a clear advantage. For a dipolar emitter oriented parallel to the surface the advantage of the immersion based techniques starts for half collecting angles larger than 60°.

Experimentally, the gain of the immersion based techniques is at least one order of magnitude higher compared to the dipole simulations. This additional advantage results from the different behavior of a dipole and a plasmonic structure. Obviously, the emission characteristics of the plasmonic structure varies strongly from the emission characteristics of a dipole. The gold nano posts are nice tools to evaluate the characteristics of a microscope. The non bleachable one-photon gold luminescence provides a stable signal and the ordered arrangement of the single posts in a rectangular array gives a way to check the linearity of a scanning system.

To study emitters at a glass interface, oil immersion lenses have a huge advantage. In comparison to the air lens, their transmittance is much higher, while even the high NA and the high reflectivity of the parabolic mirror can't compensate the losses given by the glass.

4.2. Gold discs

Gold discs are lithographically fabricated by Monika Fleischer (research group "Plasmonic Nanostructures", University of Tübingen) according to a procedure published before.[STA07] On this sample, the heights of all the nano structures are fixed at 100 nm. For the optical measurements nano discs with diameters of 60 nm, 100 nm and 180 nm are used. The aspect ratios (the length of the long axis versus the length of the short axis) of these three types of nano objects are 1.5, 1 and 1.8. The inter-particle distances are not smaller than 2 µm.

Contrary to Chapter 4.1, the gold discs here are manufactured on a silicon waver piece. Due to the opaque behavior of silicon, the immersion free focusing elements, namely the parabolic mirror (NA 0.998) and the air objective lens (NA 0.75), have to be used. Additionally, the focal fields at an interface depend on the refractive indexes of the air and the substrate. For focusing the APDM, only the size of the focal field changes with the change of the focusing element. As shown in Figure 19, the full width at half maximum (FWHM) of the total focal field using the parabolic mirror is approximately one time the wavelength of the used laser, while the FWHM of the AO is approximately 1.5 times the wavelength.

Figure 19: Intensity distributions of a focused 632.8 nm wavelength, APDM in the focus of different focusing elements at a silicon air interface. The air objective lens (AO) (black solid line), focuses with the weakest NA of 0.75 has the largest focus with a focal diameter of more than 1 λ. The parabolic mirror (PM) (red dashed line) with the high NA of 0.998 in air achieves a higher confinement to a focal diameter of approximately 1 λ.

For the RPDM, the main difference between glass and silicon lies in the intensity ratios of the focal fields. Thus, directly at the interface, the longitudinal field is much stronger for both focusing elements compared to an air-glass interface, the intensity ratio between

longitudinal and transversal field dramatically collapses in the air lens focus 100 nm above the surface. Therefore, the field in a 100 nm high structure is highly inhomogeneous when illuminated by the RPDM focused through a 0.75 NA air lens. The distance dependence of the intensity distributions in the focus for the silicon air interface is compared in Figure 20.
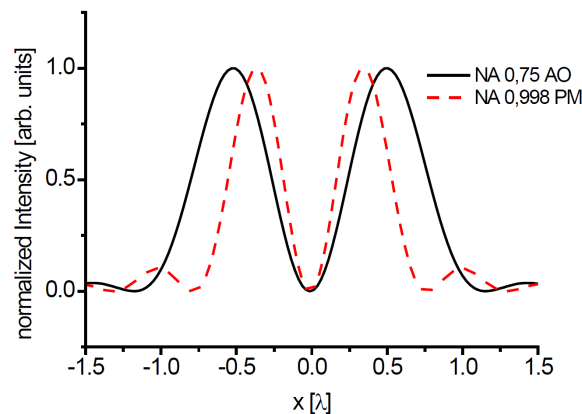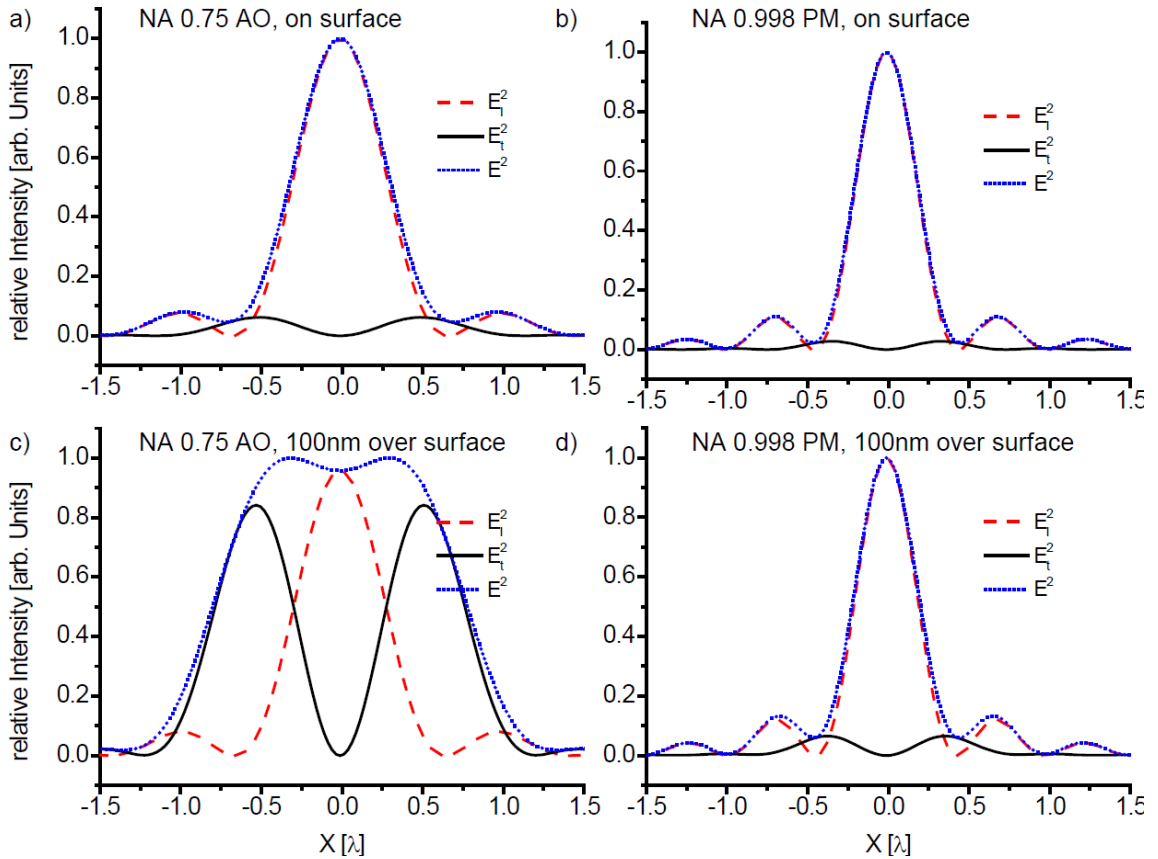

Figure 20: Intensity distributions of a focused 632.8 nm wavelength, RPDM in the focus of different focusing elements at a silicon air interface. The longitudinal- or z-field (E_l^2) is plotted as a red, dashed line while the black solid line represents the transversal- or in plane field component (E_t^2) in the focus. The sum of both fields ($E^2 = E_l^2 + E_t^2$) is plotted with a blue, dotted line. The single graphs showing the focal fields a) and c) for an air objective lens with an NA of 0.75, b) and d) for a parabolic mirror with a NA of 0.998. While for a) and b) the focal field at the interface is displayed, c) and d) are representing the fields at a height of 100 nm above the surface.

The differences in the excitation patterns for both modes and the comparison between the two used setups are shown in Figure 21. As illustrated in Figure 20 the longitudinal field of a focused RPDM using the air objective is weaker compared to the transversal field component. The pattern in Figure 21 excited with the RPDM at 632.8 nm using the AO

(center column, rows a), c) and e)) can be considered as superposition between the azimuthal component (rows b), d) and f)) and the purely longitudinal field pattern. The best fit to a purely longitudinal field pattern is acquired with the radial focus of the parabolic mirror (right column, rows a), c) and e)). The images recorded with 632.8 nm excitation wavelength in azimuthal mode are getting more intense by enlarging the diameter of the structures.

4.2.1. Variation of the excitation wavelength

Upon excitation of the samples with the wavelength 514.5 nm the difference between illumination with RPDM and APDM appear to be faint. The APDM illumination results in a ring shaped excitation pattern for every size of the structure. The maximum intensity in the images didn't change much over the modification of the size. Only the largest structure (180 nm) exhibits a weaker signal under the same experimental conditions with respect to the others. Changing the excitation mode to RPDM, the pattern looks similar. The low signal to noise ratio of the pattern of the 60 nm structure, excited with the RPDM at a wavelength of 514.5 nm (see Figure 21a), and the level of the signal in the center of the pattern having a similar level like the background indicates, that only the in plane component of the radial mode is able to excite the nano particle. This is a direct discrimination of the two different fields in the focus of the air objective by the plasmonic modes of the nano particle at a wavelength of 514.5 nm. Figure 21 shows for the same 60 nm diameter disc excited with 632.8 nm (AO), the RPDM-image is a superposition of the very weak longitudinal and the stronger transversal field in the focus of the AO. As the resonance frequency of the in plane axis is close to 514.5 nm the optical effect is enhanced in a way, that the azimuthal beam shows a more intensive excitation pattern. Assuming a perfect radial beam at 514.5 nm the presented structures are not resonant in the out of plane direction and result in absence of the corresponding longitudinal part of the pattern.
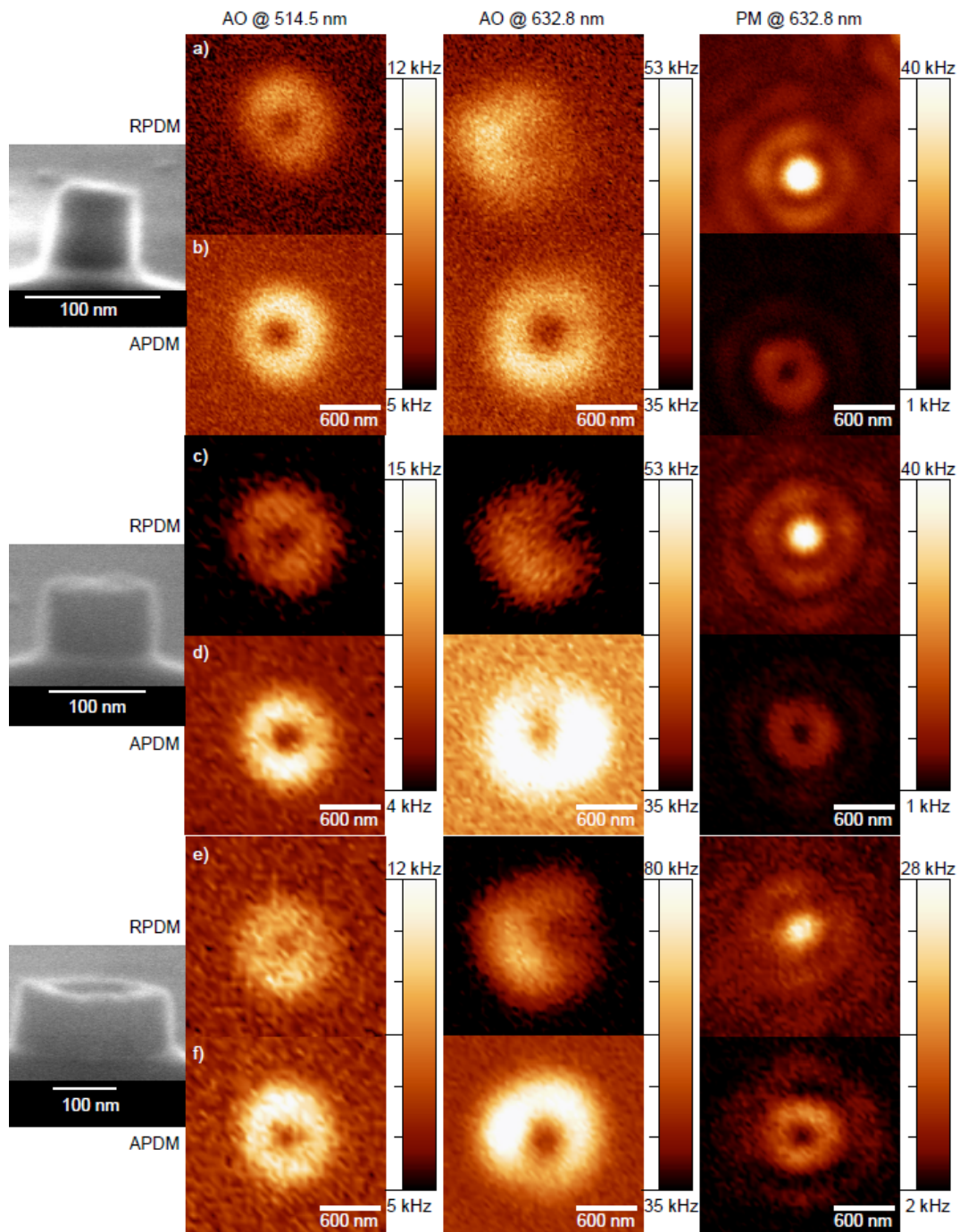
Figure 21: Photoluminescence images of gold nano disc with a diameter of 60 nm (rows a) and b)), 100 nm (rows c) and d)) and 180 nm (rows e) and f)). The excitation mode was the RPDM in rows a), c) and e) whereas in rows b), d) and f) the APDM was used. An SEM image of the corresponding discs is given on the left side.

A comparison with the excitation patterns acquired with the parabolic mirror at an excitation wavelength of 632.8 nm gives a good impression of the excitability of the three different nano discs at this wavelength. Under excitation with the RPDM, the excitation

pattern of all three structures are looking similar, mirroring the longitudinal focal field. Nevertheless, the total signal strength declines by increasing the diameter of the nano structures as a consequence of a shift in the according plasmon resonance. The direct comparison of the RPDM images recorded with the parabolic mirror to the ones recorded with the AO reveal a dipole like behavior of the plasmon emission. This emitting dipole stands upright at the silicon surface. While the PM has an NA of nearly one and therefore is able to collect nearly all of the emitted luminescence, the AO has an NA of only 0.75 and therefore it has a half collection angle of just 49°. This low collection angle is not able to collect most of the emitted signal of the upright standing dipole resulting in much weaker image contrasts.

The maximum intensity of the excitation patterns acquired with the APDM rises with increasing diameter of the nano discs. This indicates a better excitability of the in plane plasmon resonance of larger discs. Also the luminescence intensity of the RPDM patterns is much weaker compared to the APDM pattern. Here, a dipole parallel to the surface serves as a model for the excitation pattern of the structure. This lying dipole emits a lot of energy directly into the AO along its optical axis. For the PM, emission directly at the optical axis is cut out by the aperture in the mirror, serving as entrance window of a near field head and therefore the intensity of the excitation pattern acquired with the APDM is weaker. In addition, the focal electric field on the interface air – silicon increases differently for the AO and the PM. In the PM, the maximum intensity is 288 nm away from the surface, while it is only 200 nm away from the surface for the AO (see Figure 22).
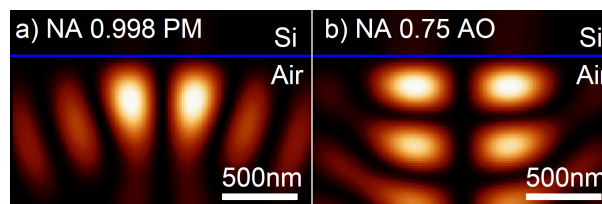

Figure 22: xz-cut through the simulated electrical fields in the focal region of the parabolic mirror (a) and the AO (b) for the APDM at a silicon – air interface (silicon above the blue line, air below the blue line). The distance between the surface of the silicon (blue line) and the maximum of the electric field is higher for the parabolic mirror compared to the AO.

4.2.2. Luminescence spectra

Most of the published studies concerning plasmonic properties of nano structures refer to white light scattering-spectra [ANK08, LAM00, LAR07, MCF03]. Others utilize SERS enhancement factors to characterize plasmonic structures [DIE06]. A different way to study the plasmonic properties of gold NPs is to look at the relation between the gold luminescence and the spectral position of the plasmonic resonances.[BOY86, DUL04, STE08] Previous investigations showed the relation between the luminescence spectra of gold NP-aggregates, excited by discrete laser wavelengths, and their respective white light scattering spectra, while excitation with the resonance wavelength results in a plasmon enhanced PL. [HU12, SHA12, STE08, WAC12, YOR12]

Here, the plasmonic properties of gold nano-disc-arrays are studied by the spectral behavior of their PL. Due to the suboptimal performance in transmission of the AO, the spectra acquired for the excitation wavelength of 632.8 nm are recorded with the parabolic mirror, while the spectra for the excitation wavelength of 514.5 nm, were acquired only with the AO setup. Upon exciting the nano structures with the wavelength of 632.8 nm we observed a strong enhanced luminescence for the discs with a diameter of 60 nm. The resonance frequency of some especially bright discs is close to the excitation laser frequency. A generally higher enhancement was achieved by exciting the nano discs with the RPDM (Figure 23b)), in comparison to the excitation with the APDM (Figure 23d). This result shows that RPDM focused by a PM-setup is effectively excites a dipole like momentum that is oriented normal to the substrate. For radially polarized excitation, the spectral position of the luminescence peak has a blue shift with increasing diameters. Here the respective plasmon resonance in z-direction also shows a blue shift since the z-axis of the disc becomes the short axis of the particle. Similar behavior was found e.g. in absorption spectra and theoretical calculations of gold nano rods in aqueous solution.[LIN99, NIK03, PER05] The plasmon resonance frequency of the short axis reacts with a slight blue-shift on the increase of the long axis.
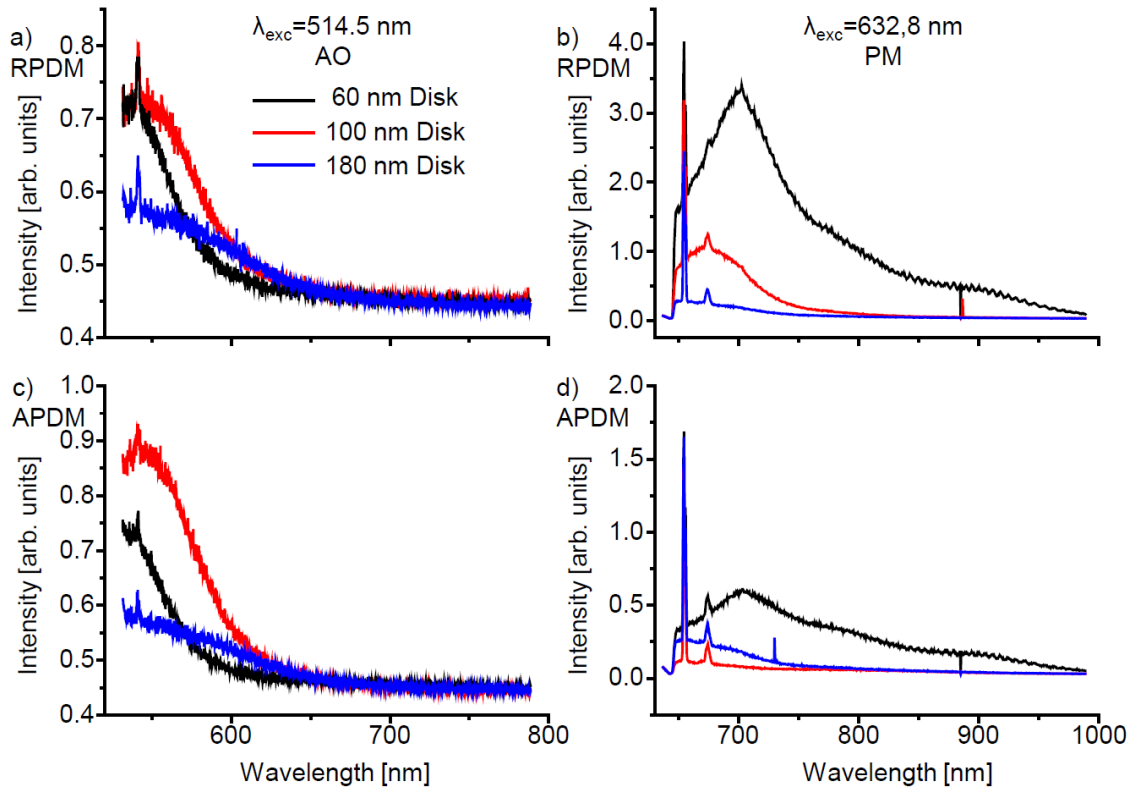
Figure 23: Photoluminescence spectra of gold nano discs recorded with an excitation-wavelength at a) and c) 514.5 nm and b) and d) 632.8 nm at the same excitation power. The exciting mode for a) and b) was the RPDM and for c) and d) the APDM. For 514.5 nm excitation the peak maximum for the discs with a higher aspect ratio (diameter 60 nm) is blue shifted to the peak maximum of the discs with 100 nm diameter whereas the peak maximum is red-shifted for excitation with 632.8 nm.

The excitation with the APDM at a wavelength of 632.8 nm shows the same trend at much lower levels. A look at the mechanism of the gold luminescence shows, that the excited plasmon depletes over an exciton and then either the exciton luminesces or converts again into a plasmon that luminesces.[WAC13] Independent of the way the luminescence is generated, the path towards the exciton erases all polarization information of the excitation laser beam from the resulting luminescence. By this way, the azimuthally polarized excitation is able to emit luminescence of the resonance in z-direction and vice versa. Due to the inefficiency of all these processes, the intensity of the luminescence signal decreases.

The spectra acquired under 514.5 nm wavelength RPDM and APDM excitation are shown in Figure 23a and c, respectively. For both spectra, a trend towards longer wavelengths for increasing disc diameters can be observed. The higher intensity of the 100 nm disc under excitation with the APDM shows, that this size of discs has the best excitability for the in plane mode at this wavelength. Unfortunately, due to the weak

overlab of the excitation laser with the Plasmon resonance and the narrow collecting angle of the AO, the collected signal is very weak and misses the spectral components from plasmonic modes that radiate at angles too large for the NA of the lens.

4.2.3. Conclusion

The optical properties of gold nano discs with different diameters were characterized by using the RPDM and APDM at the wavelengths 632.8 nm and 514.5 nm. Two different focussing elements are used for a comparison of their abilities to image and for taking spectra of non transparent samples. Due to the high NA of the parabolic mirror, it dominates the comparison in both disciplines. Its imaging possibilities are better, not only by a higher confined focal field, but also by the high collection angle. The great collecting capabilities of the parabolic mirror also enhance the possibility to collect spectra.

The 60 nm diameter gold nano discs' z-directed resonance is well excitable by the 632.8 nm laser. The spectra as well as the luminescence image do exhibit the highest signal strength. Even by keeping the height of the nano structures constant, the excitability of this z-resonance fades away when the diameter is increased. The excitation of the gold nano discs in z-direction by the 514.5 nm laser is not observed. This could be the result of three effects. First, there is nearly no excitability in the nano discs z-axis at a wavelength of 514.5 nm. Second, the longitudinal field of the RPDM at 514.5 nm in the focus of the AO is too weak to excite this direction or third, the collection angle of the AO and the emission angle of the z-plasmon did not overlap, resulting in a weak collection efficiency.

4.3. Gold cones on glass

The properties of cylindrical gold nano structures were discussed before. The change from cylindrical to a cone-like geometry of the gold structure introduces a defined main axis into the nano structure, namely the axis from the tip to the base. The excitation of plasmons along this axis leads to a high field enhancement in the apex of the cone, resulting in the "lighting rod effect".[STA07] Here the electrons of the plasmon are concentrated by the shape of the gold cone in the apex leading to a high localized charge density. This effect is used in optical antenna systems like the bow tie antenna to concentrate energy from an electromagnetic wave in the gap between two aligned triangles.[NOV11] Such bow tie configurations are present e.g. in fisher patterns, which are produced by covering a monolayer of polymer nano spheres with a metal film. After removing the nano spheres, a hexagonal lattice of triangles all in tip to tip - or bow tie - configuration remains at the surface. These "Fischer patterns" are used for e.g. surface enhanced Raman scattering (SERS) [CAM08, HAY03, HEN12] or localized surface plasmon resonance (LSPR) sensing [WHI05, WIL06]. This bow tie configuration usually has a 2D structure, lying flat on a substrate surface. By using gold nano cones, a 3D configuration of such a bow tie antenna is possible by placing a sharp tip above a cone, enabling more degrees of freedom in the control of the gap size and tip to tip orientation.[FLE08] Therefore, the knowledge of the real tip to base resonance, also called z-resonance, of these cones is crucial. Using dark field scattering spectroscopy to find the resonance, like in [SCH13], is a demanding task, because the z-resonance behaves like a standing dipole emitter, thus the scattered photons are usually cut by the dark field aperture or the low NA of the detecting lens. However, the one-photon luminescence spectra of gold nano particles excited with blue light is modulated by the plasmon resonances of the particle.[BEV03, BOU05, DUL04, HU12, STE08, YOR12] The plasmon resonances of the gold nano particles are acting as a spectral enhancement factor for the intrinsic one-photon gold luminescence spectrum as found in bulk gold.[SHA12] The measurement of the plasmon modulated gold luminescence spectra offers a method to gain access to the cones z-plasmons resonance.

The gold cones are manufactured by Julia Fulmes (research group "Plasmonic Nanostructures", University of Tübingen) via e-beam lithography on a 22 mm x 22 mm standard microscopy cover slide with a thickness of 0.17 mm. To ensure the conductivity

of the sample, a transparent 50 nm indium tin oxide (ITO) layer was added between the glass and the gold cones.[SCH13] Three different cone heights are used in this study, namely 95 nm, 130 nm and 170 nm. The aspect ratio of all these cones is kept at 0.8 leading to base diameters of 118 nm, 160 nm and 200 nm, respectively.
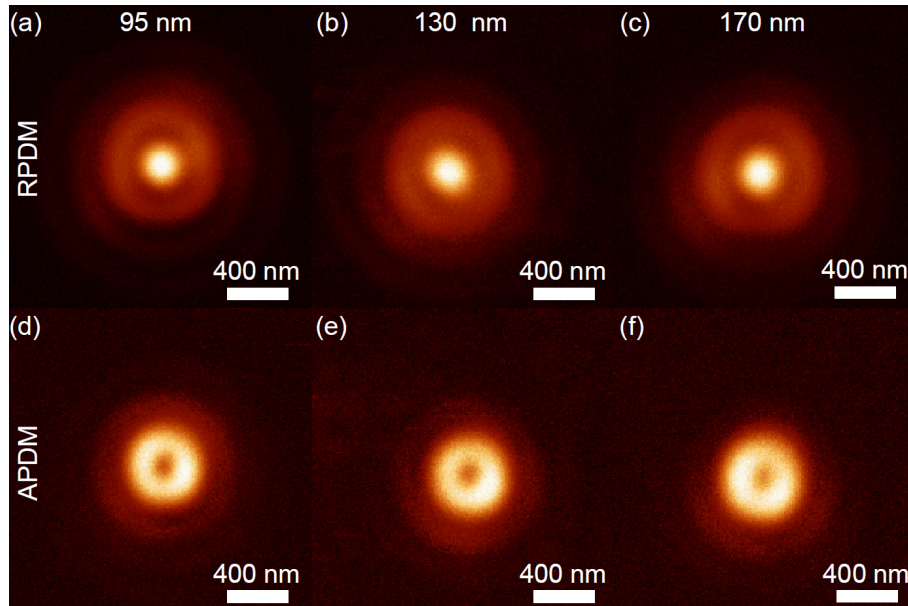
Figure 24: Confocally acquired luminescence patterns of 95 nm (a, d), 130 nm (b, e) and 170 nm (c, f) high gold nano cones for radially (a-c) and azimuthally (d-f) polarized excitation.

The one-photon gold luminescence patterns of the cones acquired with a 100x oil immersion objective with an NA of 1.46 upon excitation with a 488 nm RPDM or APDM are shown in Figure 24. The size of the excitation patterns increases with the size of the individual cones. In the case for RPDM excitation (Figure 24a-c), the pattern represents the field distribution of the focal field, having an intense spot in the center, due to the longitudinal field of the focus. This spot is surrounded by a ring that represents the in plane field component in the focus of the RPDM. The patterns acquired with the APDM are convolutions of the cones base shape and the focal field distribution. For the 95 nm and 170 nm cones a nearly round patterns are acquired. The slightly higher intensities at the left and right flank of the pattern are the result of an oval deformation of the cones' base (Figure 24d and f). The asymmetry in the APDM excitation pattern of the 130 nm high cone is most likely resulting of a slight misalignment of the azimuthal mode (Figure 24e). The luminescence intensity slightly decreases from the 95 nm cones as the brightest emitters to the 170 nm cones independent of the excitation polarization. The maximum

amplitude of the luminescence intensity of these confocal measurements decreases by 25 %. Most of this decrease is the result of the defocusing in the measurements with the 130 nm and 170 nm high cones.

The luminescence spectra of the gold cones acquired with the RPDM differ in their shape from the luminescence spectra acquired with the APDM. In the spectra acquired with 488 nm wavelength RPDM excitation, a dominant peak around 520 nm, depending on the cone size, is present. A second peak around 650 nm is also visible as a weak shoulder. For excitation with the APDM, the former dominant peak around 520 nm and the peak around 650 nm have similar intensities.
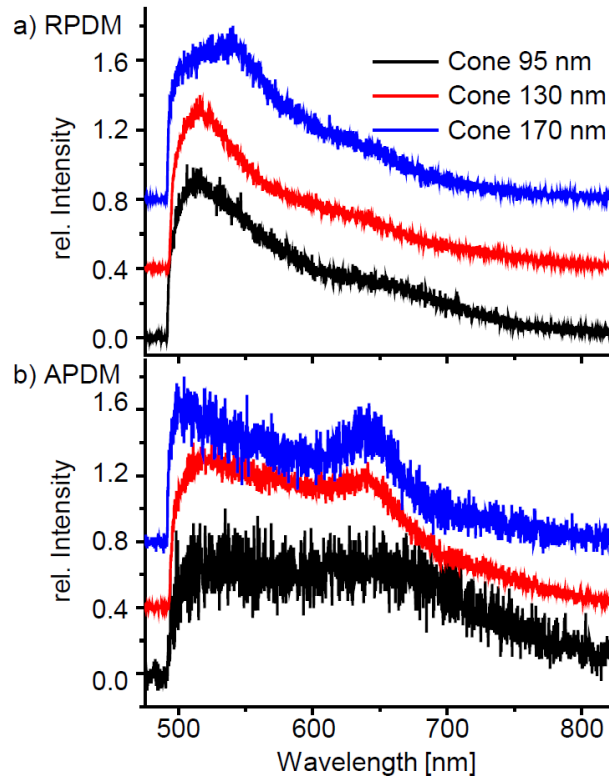
Figure 25: Normalized one-photon luminescence spectra of gold cones for an excitation with 488 nm wavelength RPDM (a) and APDM (b). The spectra for the 95 nm (black line), 130 nm (red line) and 170 nm (blue line) high cones are separated by an offset of 0.4 units of relative intensity.

The bluest peak in the luminescence spectra acquired with the RPDM varies by a red shift with increasing cone size. By fitting the spectra, peak positions from 512 nm for the 95 nm high cones over 516 nm for the 130 nm high cones to 529 nm for the 170 nm high cones are found.

Comparing the spectra of cones acquired with the RPDM to the spectra acquired at a 130 nm thick gold film using either the RPDM or the APDM (Figure 26), the shape of the spectrum looks similar. This spectrum acquired from the 130 nm thick gold film acts here as a model for the spectrum of bulk gold recorded at the same conditions. The used excitation laser wavelength of 488 nm matches the absorption band of the gold d-band electrons to the sp-band, leading to a direct excitation of electron hole pairs. The bulk luminescence spectra of gold results of the decay of these electron hole pairs.
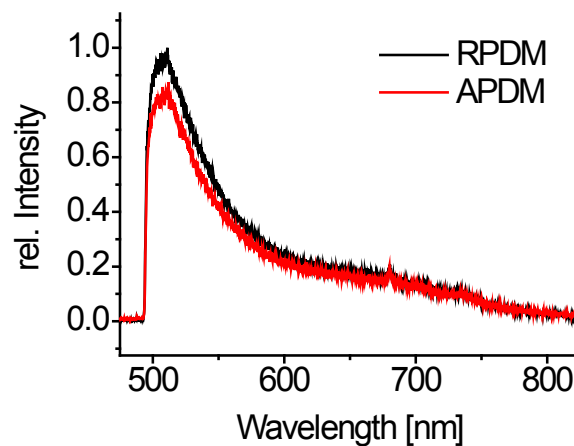
Figure 26: Luminescence spectrum of a 130 nm thick gold film, excited by a 488 nm wavelength RPDM (black) and APDM (red) laser focus.

The similarity in the RPDM spectra of the cones to the spectrum of bulk gold may be caused by the shape of the cone in combination of the exciting polarization. The longitudinal component of the RPDM focus drives the electron hole pairs from the base to the tip leading to a concentration of the electron hole pairs in the apex, due to the shape of the cone. Here the electron hole pairs can recombine undisturbed from the glass surface. By excitation with the APDM, the electron hole pairs are excited at the interface between glass and gold and move along the base of the cone. Due to the excitation of the electron hole pairs near the gold-glass interface, an additional energy reducing factor for the electron hole pairs is introduced, resulting in a different shape of the decay luminescence spectrum.

Information about the plasmon resonances can also be seen in the spectra. The plasmon resonances of gold nano structures can enhance luminescence processes. A simple model to understand the modulation of the shape of a gold luminescence spectrum is the assumption of the plasmon resonances to be simple enhancement factors.[SHA12] The final luminescence spectrum is then the result of a multiplication of the gold bulk luminescence spectra and the plasmon bands. To gain access to the plasmon band positions, the bulk luminescence spectrum has to be divided by the luminescence spectra of the cones.
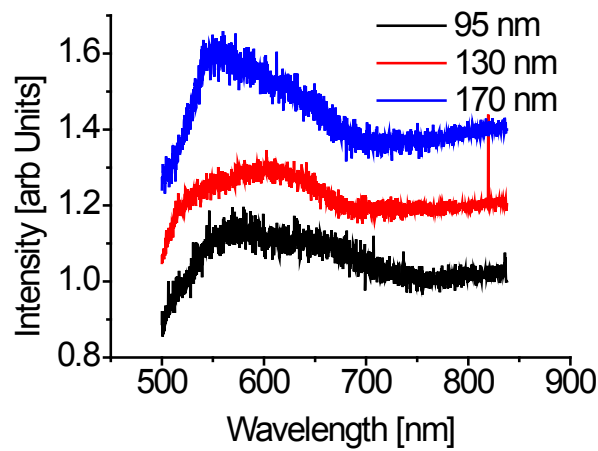
Figure 27: The cone spectra of Figure 25a (RPDM) divided by the luminescence spectra of a gold film shown in Figure 26. This partition clarifies the parts of the plasmon enhanced gold luminescence from the unenhanced luminescence of bulk gold at the same experimental conditions.

By fitting the spectra resulting of this partition, three peak positions can be found. First, the most red, very broad peak has a position at a wavelength of 830 nm ±20 nm and a spectral width of at least 300 nm. This peak is an artefact of the division of the cone and bulk luminescence spectra. Because, at high wavelengths, two signals running into their background signal, or as relative number running to zero, and then are divided one by another, with the divisor (bulk spectra) at slightly smaller numbers compared to the dividend (cone spectra). Second, the middle peak with values of 654 nm for the 95 nm high cones, 607 nm for the 130 nm high cones and 621 nm for the 170 nm high cones represents the in plane or base resonance of the cones. Third, the most blue peak, representing the out of plane or tip to base resonance of the cone has values of 556 nm for the 95 nm high cones, 548 nm for the 130 nm high cones and 550 nm for the 170 nm high cones.

4.3.1. Comparison with simulated plasmon resonances

The plasmon resonances of the three types of cones are calculated using the finite element method programme Comsol Multiphysics. The model includes gold cones on an ITO substrate, with ideal shape and the same dimensions as the ones used in the experimental part. The excitation of the base and the tip to base resonances are achieved by a plane wave with either x- or z-polarisation, approaching the cone from the side. The resulting scattering spectra are normalized with respect to the intensity maximum as shown in Figure 28a for the tip to base resonance and in Figure 28b for the base resonance.
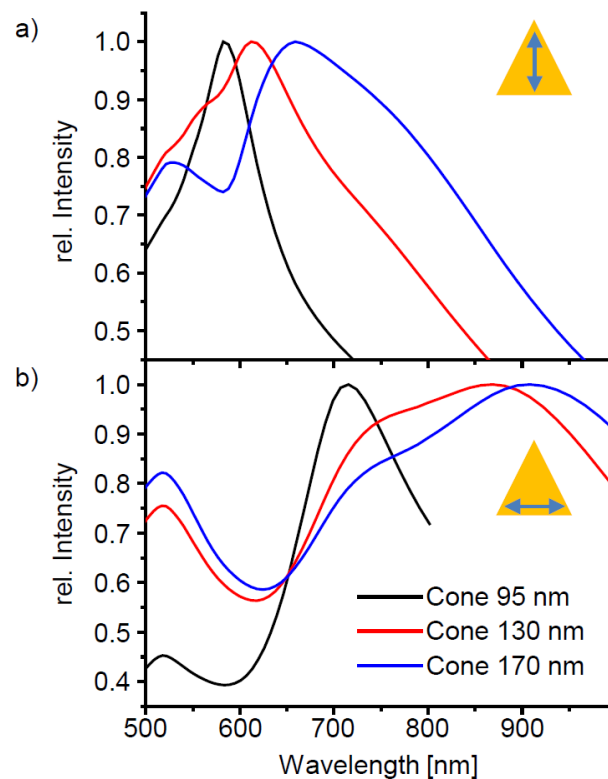
Figure 28: Simulated plasmon resonance spectra of gold cones with 95 nm (black), 130 nm (red) and 170 nm (blue) heights. The out of plane a) and the in plane b) resonance of the cones are shown separately. Note that the peak at 520 nm wavelength is a result of the d-band absorption of gold.

An overview of the experimentally found and the calculated resonances are presented in Table 4. Both the tip-base as well as the base resonances found experimentally deviates largely from the resonances derived by the simulation. This discrepancy can be the result of different factors.

cone height	tip-base experimental	tip-base simulation	base experimental	base simulation
95 nm	556 nm	582 nm	654 nm	715 nm
130 nm	548 nm	611 nm	607 nm	731 nm & 894 nm
170 nm	550 nm	658 nm	621 nm	729 nm & 922 nm

Table 4: Comparison of the experimentally found cone resonances to the resonances calculated by finite element method.

One factor is the deviation of the real cone size and shape from an ideal shape. Figure 29 shows an SEM image of a 95 nm high cone, acquired after the luminescence spectra has been recorded. Obviously the apex of the cone is not as sharp as expected from fabrication and has now a radius of approximately 20 nm. This flattening of the cones can be found only at cones, where luminescence spectra are taken from. Possibly, the excitation of the cones with a laser wavelength of 488 nm heats up the cones at their apex, where at radially polarized excitation the highest near field intensity is located. By this geometrical change, the plasmon resonances will change accordingly. The tip to base resonance for smaller cones should blue shift, while the base resonance should exhibit red shift.[SCH13]
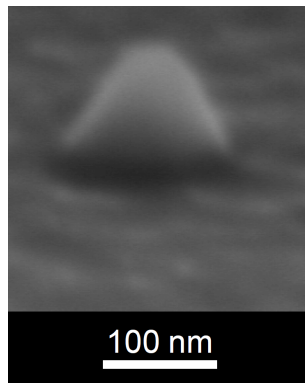
Figure 29: SEM image of a 95 nm high cone, acquired after the confocal luminescence measurements were performed. An obvious flattening of the apex of the cone has occurred.

Second, in the simulation the cones are modelled to rest on an ITO surface. In the experiment, the ITO layer is only 50 nm thick while the main substrate is glass. The difference in refraction index between glass and ITO could also shift the resonances.

An interesting effect appears for the simulated base resonances. The cones with 130 nm and 170 nm height, respectively, are showing three resonances. The first resonance at 520 nm is linked directly to the sp-d band absorption of gold. While the more intense resonance at higher wavelengths shows a profound shift by changing the cone size, the weaker resonance doesn't show this behavior and is fixed at around 730 nm. The cone-size dependent resonance here is located at too high wavelengths. According to literature, there should be only one resonance for the base mode, which should not exceed a wavelength of 800 nm for a cone with 200 nm height.[SCH13]

4.3.2. Conclusion

The gold luminescence spectra of nano cones excited by the focal field of either an azimuthally or a radially polarized, 488 nm laser beam differ in their shape. A first approach has been to relate the differences in the spectra with the plasmon resonances. The shape of the cones influences the shape of the raw luminescence spectra. Under excitation with the RPDM, the longitudinal field of the focus drives the electrons associated with the plasmon oscillation into the apex, where they are concentrated. Additionally, electron hole pairs are most efficiently formed at the tip apex where the local electrical field strength reaches the highest values and correspondingly the highest probability for electron-hole formation is reached. Furthermore, electron hole pairs in the tip are only surrounded by air and therefore can recombine preferably by emission of a photon. This last mechanism is further supported by the enhanced local density of optical states around the tip apex. Therefore the RPDM cone spectrum looks like the bulk gold spectra. Exciting the cones with the APDM, the electron hole pairs are located at the interface between gold and glass. At this interface an alternative depletion path for the electron hole pairs is possible i.e. the transfer of parts of the electron hole pair energy as heat to the glass results in smaller electron hole pair energies.

The gold luminescence spectra of plasmonic particles is composed of the bulk gold luminescence spectra modified by the plasmon resonances of the particle. These plasmon resonances are acting like enhancement factors multiplied to the bulk gold luminescence spectra. By partition of the experimentally found spectra of the gold cones by the bulk gold spectrum, the plasmon resonance spectrum can be calculated. By correlating these results

to simulated plasmon resonance spectra of gold cones, a large blue shift of the observed resonances is found. One reason for this mismatch is the melting of the tip that occurs under illuminated with the 488 nm wavelength laser. The RPDM laser focus seems to melt up the tips of the single cones, flattening them to a radius of about 20 nm. Second, the spectrum used as "bulk" gold spectrum was experimentally recorded of a 130 nm thick gold film. A deviation of this spectrum to a real bulk spectrum (i.e. of a gold crystal) influences the result of the performed partition. Other explanations of the mismatch between the experimentally found values and the calculated ones may be due to the different refractive index of the substrate in the simulations. The simulation also shows a split up of the resonances for larger cones, which is not expected from simulations.

For a better understanding of the resonances found by analyzing the luminescence spectra of the gold cones, a comparison to scattering spectra of the same cones would be needed. To gain access especially to the tip to base resonance a dark field spectroscopy system as described in Reference [SCH08] has to be used. This technique works like a total internal reflection fluorescence (TIRF) microscope, where the exciting beam is focussed at angles high enough, to undergo total internal reflection at the sample surface. In addition, in one half of the microscope's back aperture the transmission of light and also the back reflected excitation light is blocked. The spectroscopic information is scattered by the nano structure at the sample surface and by this can be detected in the unblocked part of the optical path.

4.4. Gold nano rings

For matching the symmetry between cylindrical vector beams and nano objects, there is no way around the ring shape. This kind of structures attracted significant scientific interest over the last years ranging from the fabrication of these structures to their optical properties. Several different resonances can be found for these kind of objects depending on the diameter of the ring, the width and the height of the sidewalls.[HAO08] For linearly polarized excitation, the plasmonic properties of such nano rings can be described as linear combination of the electromagnetic modes of a plasmonic nano disc and a plasmonic nano hole forming a bonding and an antibonding plasmonic mode.[AIZ03, PRO03] The interaction of nano rings with radially and azimuthally polarized excitation was theoretically investigated in 2007.[SUA07] In this paper Suarez et al. found a promising model to explain the interaction of plasmonic nano rings with radially and azimuthally polarized excitation. To identify the possible resonances of such plasmonic nano rings with radially and azimuthally polarized excitation, simple geometrical considerations can be made. Due to the symmetry match of the ring shape to the radially and azimuthally polarization states, there are only two basic resonances to consider, namely the in plane resonance depending on the ring thickness and the axial resonance depending on the rings height.

The luminescence behavior of gold nano rings is investigated for eight different ring diameters excited by a 632.8 nm wavelength APDM and RPDM focus of an oil objective lens with an NA of 1.25. The ring diameters are ranging from 350 nm to 700 nm in 50 nm steps with constant ring height and thickness of 50 nm. The ring structures are manufactured by Julia Fulmes (research group "Plasmonic Nanostructures", University of Tübingen). The confocal luminescence patterns are presented in Figure 30. The luminescence patterns acquired by excitation with the APDM (Figure 30b) resemble those of a ring, while the luminescence patterns acquired by excitation with the RPDM (Figure 30c) look similar to the RPDM focal field.
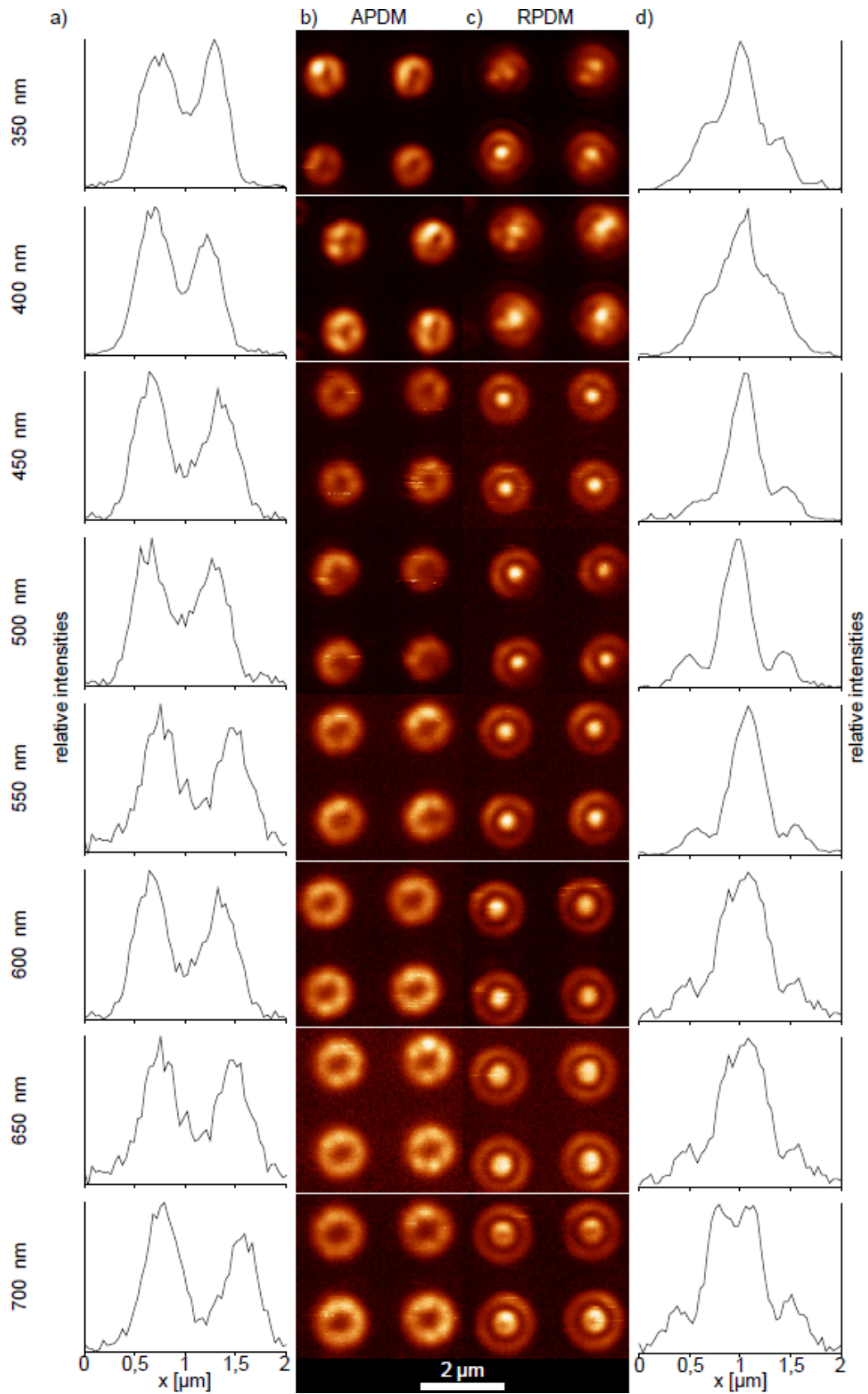
Figure 30: Luminescence measurements of gold nano rings with diameters ranging from 350 nm to 700 nm in 50 nm steps. The width and the height of the ring walls is 50 nm for all rings. Confocal images illuminated by the APDM and RPDM are shown in columns (b) and (c), respectively. Columns (a) and (d) are representative intensity profiles of the corresponding rings for APDM (a) and RPDM (b) illumination.

The discrimination of the in and out of plane resonance of the walls of such gold nano rings was performed in 2013 by Fulmes et al.[FUL14] The two resonances were detected by using a combination of dark field scattering spectroscopy and extinction spectroscopy of tilted samples, and compared to finite element simulations. The plasmon resonances for in plane and out of plane directions are at 607 nm and 535 nm, respectively. Applying this to the excitation wavelength of 632.8 nm means, that mainly the in plane resonance is excited and the excitation of the out of plane resonance by the longitudinal focal field of the RPDM is negligible.
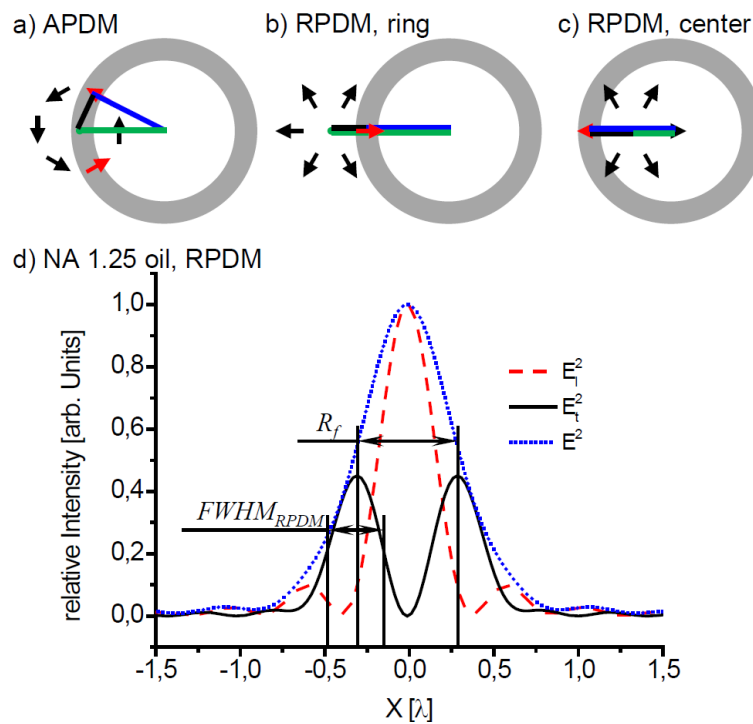
Figure 31: Geometrical construction to describe the main features of the luminescence pattern of a gold nano ring excited by an APDM (a) or a RPDM (b) outer ring and (c) inner spot. The meanings of the focus radius R_f as well as the $FWHM_{RPDM}$ are explained with the intensity distributions of a RPDM in the focus of a 1.25 NA oil immersion lens.

Luminescence patterns result from a superposition between the in plane focal fields of either the APDM or the RPDM and the rings wall width. From geometrical considerations the main parameters of the luminescence patterns can be derived. In general, for the highest luminescence signal, the excitation has to be optimized. Therefore, the electric field vector of the exciting beam has to be perpendicular to the ring wall. This is illustrated in Figure 31, where the correctly aligned electrical field vector is drawn as a red arrow, while black arrows represent the not contributing field vectors. The blue line corresponds

to the radius of the ring denoted as R_r. The black line corresponds to the radius of the intensity maximum of the in plane field in the focus. This radius is the same for the APDM as well as for the RPDM, namely $R_f = 187.5$ nm (see Figure 31d). The green line is the radius of the resulting luminescence pattern ring at maximum luminescence intensity.

To estimate the radius of the luminescence ring for APDM illumination, we have to apply the Pythagorean Theorem. In Figure 31a it is shown, that R_r (blue line) and R_f (black line) are the legs of the rectangular triangle and the radius of the luminescence ring, $R_{l,APDM}$ (green line) is the base of the rectangular triangle. For the radius of the luminescence ring follows: $R_{l,APDM} = \sqrt{R_r^2 + R_f^2}$.

The pattern acquired by excitation with the RPDM is more complex and consists of a ring and a Gaussian profile in its center. The explanation of the ring is the simple summation of the radius of the ring R_r (blue line) and the radius of the intensity maximum of the in plane field in the focus R_f (black line), as shown in Figure 31b. Therefore, the radius of the radial luminescence ring is: $R_{l,RPDM,1} = R_r + R_f$. The situation for the center spot is illustrated in Figure 31c. According to the measured data in Figure 30c, for rings with a bigger diameter than the diameter of the focus, the resulting center spot is a ring (see the 700 nm diameter nano ring). The radius of this luminescence ring can be calculated by $R_{l,RPDM,2} = |R_r - R_f|$. However, for $R_r = R_f$ the radius of the resulting luminescence pattern reaches its minimum and the diameter of the center spot rises for smaller as well as for larger rings. Additionally, the diffraction limit is still valid and therefore even for the 650 nm diameter nano ring, the center pattern can't be resolved as a ring. The correlation of the ring size to the size of the central spot in the RPDM luminescence pattern can be done regarding the FWHM of the pattern. When $R_r = R_f$, then the diameter of the inner luminescence ring should be $R_{l,RPDM,2} = 0$. In this case, the $FWHM_{RPDM}$ of the central spot should have the FWHM of the in plane focal field generated by the RPDM (see Figure 31d for the definition of $FWHM_{RPDM}$). For a 100x oil immersion lens with an NA of 1.25, this $FWHM_{RPDM}$ has the value of 190 nm. Finally, the full width at half maximum of the center spot is: $FWHM_{RPDM} = R_{l,RPDM,2} + FWHM_{RPDM}$.
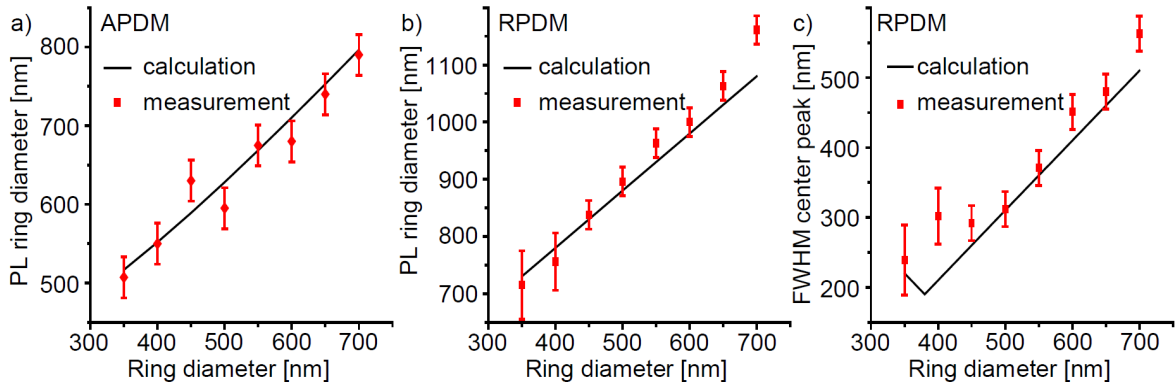
Figure 32: Comparison between the calculated and the measured properties of the luminescence pattern of gold nano rings. For the excitation with the APDM (a) the diameter of the ring pattern, while for the excitation with the RPDM the diameter of the outer ring (b) and the FWHM of the center peak (c) are plotted.

In Figure 32 the calculated luminescence pattern parameters are compared with the parameters extracted from the experimental data. For each ring size, 9 individual rings have been studied. The properties of the luminescence patterns acquired with the APDM are in a good agreement with the corresponding geometrical calculation. The variations from the calculated line depend on the exact position of the focus for each ring size, as the focus position for all nine observed rings has not been changed. Comparing the experimental and calculated luminescence patterns acquired with the RPDM, a good match for ring diameters of 450 nm to 650 nm can be found. As for the azimuthal case, most of the deviations result from the variation of the focal plane from their ideal position. For the 700 nm nano rings, the central spot is ring shaped and so the FWHM can differ. The patterns acquired with the RPDM on the gold nano rings with 350 and 400 nm diameter are blurred (see Figure 30) and cause large error bars for these rings in Figure 32b and c, differing from the calculated trend. These two ring diameters are in the regime of the diameter of the in plane field of the RPDM focus, where the FWHM of the center luminescence pattern should increase with smaller sizes of the nano rings (Figure 32c).

4.4.1. Conclusion

Gold nano rings are nice examples for symmetry matching excitation and its effects. Despite of the capability of nano rings to be excited along the ring, and maybe forming a ring current with plasmons, this ring plasmon would not be a particle but more a

propagating plasmon and would have a resonance far in the infrared region. The excitation with a wavelength of 632.8 nm gives access to the ring walls width. By excitation with the RPDM, luminescence excitation patterns reveal no influence of the ring height, which might interact with the strong longitudinally polarized part of the focus. Instead, only two rings can be found that are representing two cases: first, where the center of the focus is outside of the ring and second, where it is inside. By excitation with the APDM, the superposition of the polarization vectors with the width of the ring walls leads to a luminescence pattern with only one ring. The next step towards a perfect symmetry matching between excitation with the RPDM and the APDM is presented in the next chapter, where also an azimuthal excitability of the whole structure can be achieved.

4.5. From magneto inductive coupling to plasmonic oligomers

This chapter bases on [HEN13] and [JAE13].

The coupling phenomena of plasmonic nano particles have been hot topics in the last few years.[ALE08, CHE09, JAI10, LIN10, MIR09, SOE05] First ideas to couple such systems via magneto inductive coupling have been discussed in general by Ekaterina Shamoniva in 2007 [HES07] and for plasmonic systems by Harald Giessen in 2008 [LIU08].

Due to the perpendicular magnetic and electric field components in a light wave, the (electric-) azimuthally polarized mode can also be named as magnetically radially polarized mode. In the focal area, the electric field keeps its shape and symmetry, while the magnetic field, like the electric field of the RPDM, expresses an additional z-field. On the other hand, split ring resonators (SRR) can be described as tiny oscillating circuits where the two legs of the SRR are seen as a capacitor and the connection between the legs as a coil.[LIN04] The electric field of the APDM excites a plasmon in the SRR, driving the electrons effectively from one leg to the other. This movement of the electrons results in a magnetic field in the center of the SRR. With a "UC" arrangement of such SRRs (see Figure 33), the electric and the magnetic field should couple from one to the next SRR with low losses. At its end, the transmitted signal could be used to excite a quantum emitter or simply can be scattered towards a detector by a nano object, to analyze the behavior of such a magneto inductive waveguide.
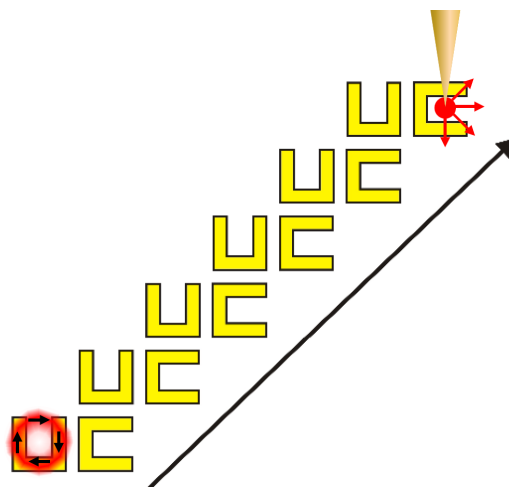
Figure 33: Idea of the magneto inductive coupling system with split ring resonators, excited by azimuthally polarized laser light. After Propagation in direction of the arrow, the transmitted optical signal can be scattered e.g. by a sharp tip.

The single split ring resonators can be manufactured to be resonant with a 632.8 nm laser with dimensions much smaller compared to the size of the azimuthally polarized focus. In Figure 34 an example for images recorded with the APDM and RPDM by using the parabolic mirror microscope is shown. Regardless of the real sizes of the SRR, the dimensions extracted from the luminescence patterns are reflecting the size of the foci. This results in an inefficient excitation due to the incomplete coverage of the focal area by one SRR as well as an additional excitation of the neighbouring SRR, leading to unwanted effects like destructive interference.
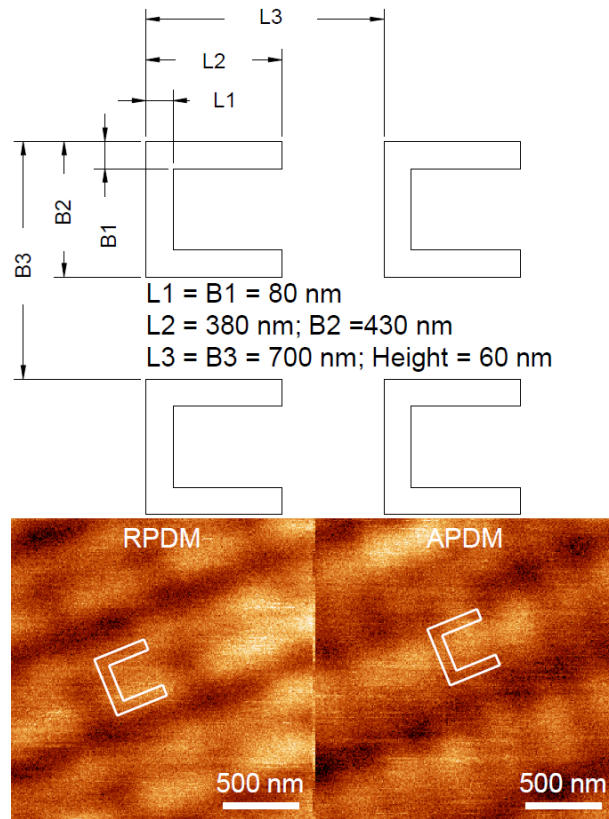
Figure 34: Confocal one-photon luminescence images of gold split ring resonators on silicon acquired by using the parabolic mirror (NA = 0.998). The pattern in the RPDM image resembles the form of the SRR. In the APDM image, the highest intensity can be found where a perfect overlap between the focus and the SRR takes place. The orientation of the SRR is illustrated with a white, schematic drawing in the image. The dimensions extracted of the images are: L2 = 511 nm; B2 = 538 nm; L3, B3 = 717 nm.

The mismatch between the size of the focus and the size of the split ring resonator, when the SRR fulfills the resonance condition for the magneto inductive coupling at 632.8 nm, isn't the only challenge. Additionally, at shrinking sizes of the structures it is harder to control the manufacturing process leading to structures deviating strongly from their ideal shape. Therefore alternative nano structures have to be considered.

4.5.1.   From Split Ring Resonators to Plasmonic Oligomers

Gold discs oriented in a circle have been identified as a potential alternative for the split ring resonators (see Figure 35). The resonance of the single gold discs can be tuned to the desired wavelength. The plasmons in each particle lead towards a magnetic field which sums up in the center of the structure.
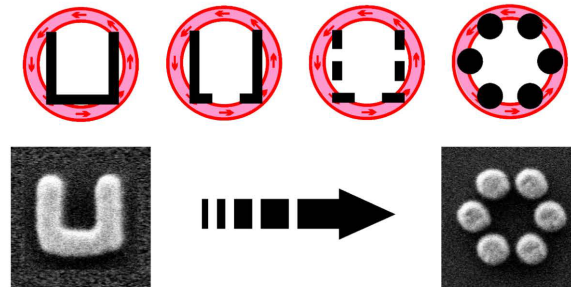
Figure 35: Transformation of a single split ring resonator towards a plasmonic oligomer with coupled individual dots to tailor the resonance frequency of the structure and gain a symmetry match with the APDM. Taken from [HEN13]

Plasmonic oligomers made of gold by Mario Hentschel (4th physics Institute and Research Center SCoPE, University of Stuttgart) were used to prove the excitability of such structures by a 632.8 nm wavelength APDM and RPDM. Here three different structures were researched in detail:

- six particles in a hexameric arrangement,
- seven particles in a heptameric arrangement and
- six particles in a heptameric arrangement where one space in the lattice is kept empty.

The particles have a diameter of 95 nm with a height of 30 nm. The diameter of the whole ensemble is 700 nm, leading to inter particle distances of 200 nm for the hexameric arrangement and 160 nm for the heptameric arrangements. White light spectra of the structures show a resonance of about 700 nm (Figure 36).
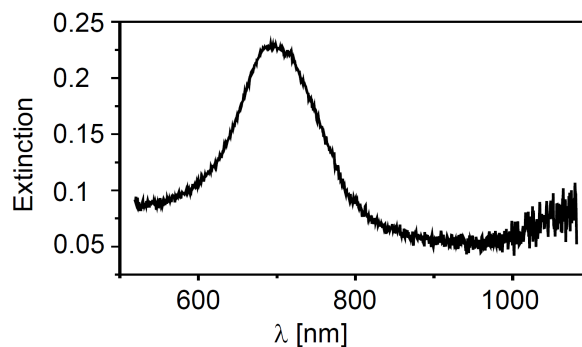
Figure 36: White light extinction spectra of an ensemble of the used oligomers with a resonance about 700 nm.

The closed hexa- and heptameric structures have almost the same confocal luminescence pattern, independent of the use of either the APDM or the RPDM (Figure 37 a, c, d and f). In general, the excitation wavelength of 632.8 nm is within the resonance of the particles. When the center of the focus of the APDM or RPDM matches with the center of the oligomer, dipolar plasmons are excited in every single disc, pointing either from the center to the rim (RPDM) or towards each other (APDM). Here the highest luminescence intensity, as expected, can be found. Due to the circular symmetry of the oligomer, the intensity at every other position has to be weaker and the complete luminescence pattern has to be center symmetric. A different situation can be found for the six heptameric arranged structures. Here, a defect in the heptameric lattice of the structure directly influences the resulting luminescence pattern in the confocal images (Figure 37g and i). The luminescence pattern in the case of excitation with the RPDM (Figure 37i) has a slight oval shape with the long axis towards the defect, but the overall variation isn't strong. At excitation with the APDM, the variation of the luminescence pattern is obvious (Figure 37g). The bright spot in the center has a long oval shape and again is directed towards the missing disc of the structure. Additionally, the pattern around the center changes from a bright disc to a crescent, with the open part towards the missing disc.
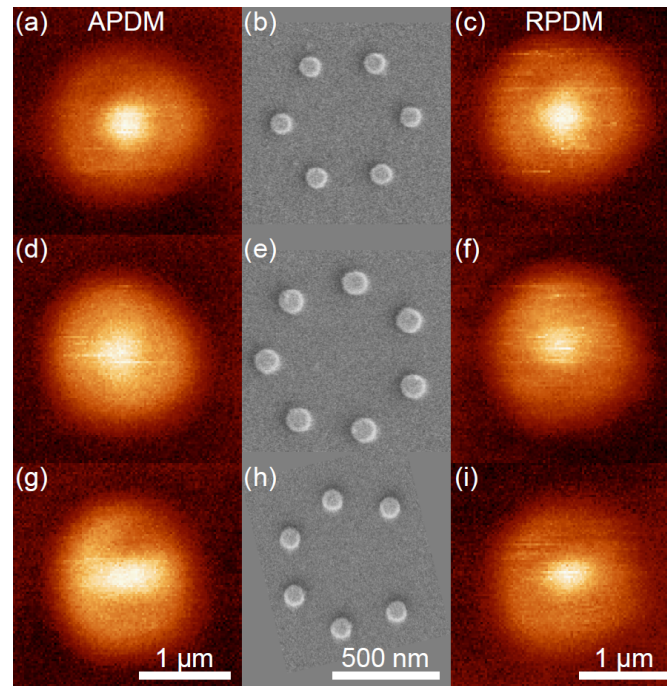
Figure 37: Confocal luminescence excitation images of gold plasmonic oligomers on silicon, recorded with an NA = 0.75 air objective lens. For the hexamer (a, c) and the heptamer (d, f) the luminescence patterns recorded with the APDM (a, d) and RPDM (d, f) are similar. For the heptamer (g, i) the position of the missing particle is visible by a change in the rotation symmetry of the luminescence patterns. This asymmetry is more obvious in the image recorded with the APDM (g) compared to the image recorded with the RPDM (i). In the center column, SEM images of the hexamer (b), the heptamer (e) and the heptamer with a missing particle (h) are shown in the same orientation like in the confocal measurement.

The confocal luminescence pattern can be described by a convolution of the focal fields with the structure. For this purpose, the absorption pattern of one gold disc with a height of 30 nm and a diameter of 95 nm is simulated using the surface integral method.[KER09] The luminescence signal and the absorption of a gold nano structure are linearly dependent on the near-field very close to the particle surface and therefore the absorption pattern is similar to the luminescence pattern. Using this pattern, six and seven particle configurations are assembled by orienting the needed number of single particle patterns in the corresponding geometry and adding up the absorption / luminescence values. The result of this superposition is shown in Figure 38. A very good agreement with the experimentally acquired luminescence pattern in Figure 37 is found.
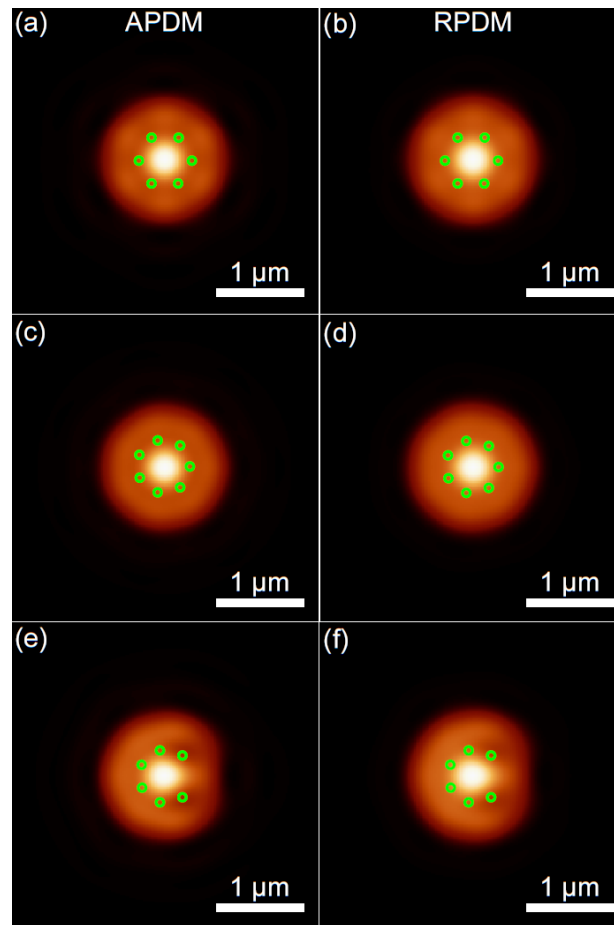
Figure 38: Simulated luminescence patterns of the plasmonic oligomers in the configuration shown in Figure 37. The green circles indicating the position of the single gold discs in relation to the luminescence pattern. A good conformity with the experimental data is eminent.

The distance of the particles used here was too large to achieve a coupling between them and so the generation of a ring-current in the structure that leads to a magnetic field in the center of the structure. To achieve this, the particles need to come closer towards each other, by keeping the overall size of the structure constant to achieve a good overlap with the focal field. When the particles in the structure are coupling, new effects have to be considered.

4.5.2. Azimuthal and Radial coupling in Plasmonic Oligomers

To describe the coupling of plasmonic particles, the hybridisation as in molecular orbital theory was adapted towards the field of plasmonics, boosting the search for new,

molecule like structures.[PRO03, WAN07] Especially structures similar to aromatic molecules like benzene are in the scope of research.[ALO11, DRE11, FAN10, HEN11, HEN10, LUK10, MIR09] At linearly polarized excitation, the spectra of these structures show a very sharp dip inside a broad absorption band. This sharp mode, also named as fano resonance, is the result of the coupling of a bright, radiative mode and a sharp dark, nonradiative mode. The use of the fano resonance of these systems for localized surface plasmon resonance (LSPR) sensing[MIR09], for metamaterials[FAN10], for specifically tailored surface enhanced raman spectroscopy (SERS) substrates[YE12] as well as possible waveguiding effects of such dens packed structures[LIU12] has been discussed.

The planar eigenmodes of a plasmonic oligomer with seven, spherical particles with the symmetry point group D_{6h} , the same point group like the molecular analogue of these structures, benzene, have been calculated by Nordlander et al. in 2009.[MIR09] Comparing these modes with the RPDM and APDM, the matching eigenmodes to these excitation beams are the A_{1g} (RPDM) and A_{2g} (APDM). While the azimuthal A_{2g} mode refers to the energetically lowest mode, whereas the radial A_{1g} mode corresponds to the energetically highest mode that can be directly excited with a symmetry matching external optical field. By using structures that are manufactured by e-beam lithography on the surface of e.g. a glass cover slide, the symmetry of the structure is decreased to the C6 point group. Furthermore, the consideration of the planar eigenmodes, does not include modes perpendicular to the plane of the structure. This perpendicular excitation is achieved by using the focal fields of the RPDM.

Coupling the modes of plasmonic structures leads to a red-shift in their resonances. This red-shift increases with the number of coupled particles.[JAI06] The six outer particles in the ring of a plasmonic oligomer, if excited with APDM to the A_{2g} mode, would couple like an infinite row of particles and therefore undergo a very large red shift. The coupling in the A_{1g} case includes in the maximum 3 particles, where the in plane fields are repulsing one another in the center, and therefore the red shift is comparatively weak.

The azimuthal and radial resonances of a plasmonic oligomer are not accessible by any standard method. Only one structure has to be brought into the focus of a radially or azimuthally polarized laser beam while the absorption is measured. On the other hand, the calculation of such resonances is much easier. Figure 39 shows the simulation of the near-field intensity enhancement of a plasmonic oligomer out of aluminum, where the diameters

of the center and the outer particles are 150 nm and 140 nm, respectively while the height of all the particles is 80 nm. The simulation was performed using the surface integral method.[KER09]
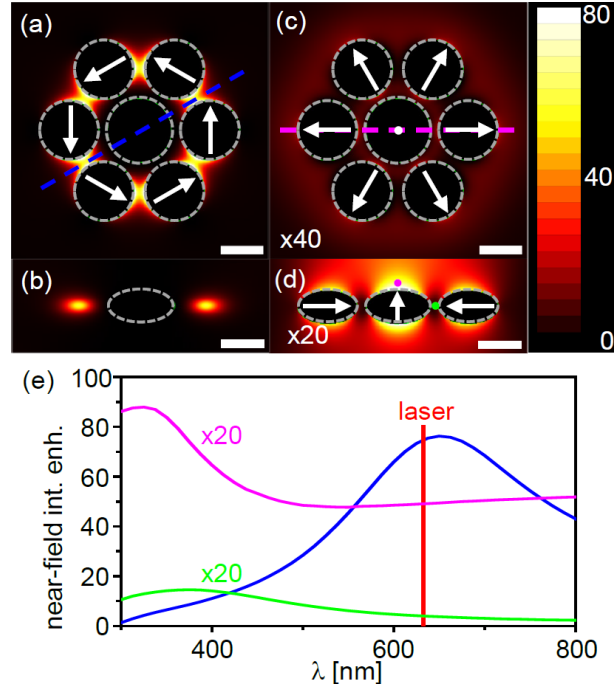
Figure 39: Simulated near-field intensity enhancement for an aluminum heptamer excited by a focused 632.8 nm APDM (a) and RPDM (c) represented in an xy-plane (focal plane) section through the center of the particles. The maximum of the intensity enhancement follows the polarization of the focal field and is located between the six particles in the ring by excitation with the APDM (a) or mainly above of the center disc at RPDM excitation (d). The white arrows indicate the symmetry of the particles' dipolar moments. The location of the near-field intensity enhancement in the xz-plane along the blue line in (a) is shown in (b), while the xz-section of the radial case shown in (d) cuts through the center of three particles (c). The azimuthal near-field intensity enhancement has its maximum centered at 650 nm and a spectral width of about 300 nm (see blue line in (e)), while the radial near-field intensity enhancement on top of the particles has its resonance at 325 nm with a spectral width of ~200 nm (see magenta line in (e) and magenta dot in (d)). The green dot in (d) marks the position where the second radial near-field intensity enhancement spectrum was taken from. It has a broad, very weak resonance around 375 nm. Note that the radial calculations are enhanced with respect to the azimuthal cases by a factor of 40 (c) or 20 (d, e). The scale bars in (a) - (d) represent 100 nm.

The blue line in Figure 39e represents the azimuthal near field intensity enhancement spectrum while the magenta and the green lines represent the radial near field intensity enhancement spectra. As predicted, the azimuthal resonance is much more red shifted compared to the radial resonance with values of 650 nm and 350 nm respectively. Additionally the radial resonance is approximately 20 times weaker compared to the azimuthal maximum. The near field intensity enhancements for a 632.8 nm excitation are

shown in Figure 39a-d. For an azimuthally polarized excitation, the near-field intensity enhancement is located in the gaps between the six particles in the ring (Figure 39a, b) and so strictly preserves the symmetry of the excitation beam. Under radially polarized excitation, the highest near-field intensity enhancement can be found mainly on top of the center particle (magenta line in Figure 39e) and some parts on top of the ring particles. A very weak near-field intensity enhancement can be found between the center and the outer particles (green line in Figure 39e). Here the plasmons of the outer particles are moving in radial direction, either pushing or pulling electrons towards the center particle. This process is energetically disfavored, and so the intensity of this signal is rather weak and at higher energies.

4.5.3. Au Nanotip as Luminescent Near-Field Probe

To measure the presence of the radial and azimuthal near fields that are excitable in the aluminum plasmonic oligomers discussed in Chapter 4.5.2 we have developed a new scanning near-field optical microscopy (SNOM) mode.[JAE13] Over the last few years, different techniques have been developed to map such near fields, near field induced polymerization [DAV96, DEE10, HUB08] or various scanning tip-based techniques [HEC00]. Within the tip-based techniques several probes like the luminescence of a single quantum emitter, e.g. single molecules [MIC00] or NV centers in nano diamonds [KUE01] were fixed at the apex of a SNOM tip. Unfortunately, the luminescence of single molecules suffer from blinking and bleaching, leading to noisy images, while the fixation of nano diamonds at the apex of a tip is a rather complicated process. Second, the scattering of e.g. a 100 nm gold sphere at the apex of a glass fiber tip [KAL01] or of a metallic or semiconductor tip with a tip radius of about 20 nm, is used in scattering Scanning Near-field Optical Microscopy (SNOM), [HAE04, HIL01] to map the near fields. These probes are quite large and have a strong perturbation effect on the near field of nano objects. Additionally, the signal scattered from the tip can interfere with the near field of the nano object, scrambling the detected signal. A different approach is the use of the luminescence of gold nano objects as a local field probe. In 2003 Novotny et al. published a method where the two- photon luminescence of a gold tip has been used to image the hot spots of gold particles upon illumination with a 120 fs laser at a wavelength of 780 nm.[BOU03]

Here the one-photon luminescence of a sharp gold tip is used to map the near-field distribution of a radially or azimuthally excited aluminum plasmonic oligomer. As a prerequisite for its use, the one-photon luminescence has to have a linear dependence towards the intensity of the exciting field, as introduced in chapter 2.2. Additionally, the shape and the intensity of the luminescence spectrum of a gold tip have to be independent of the polarization of the exciting field. In Figure 40 the one-photon luminescence of a sharp gold tip in the focus of a 632.8 nm wavelength APDM (blue) and the RPDM (red) is shown. The Intensity of the exciting field was the same for both measurements. The behavior of the real tip is very close to the prerequisites for the use as near field probe. The spectral shape in both polarizations is nearly the same, while the intensity of both spectra is only varying slightly.
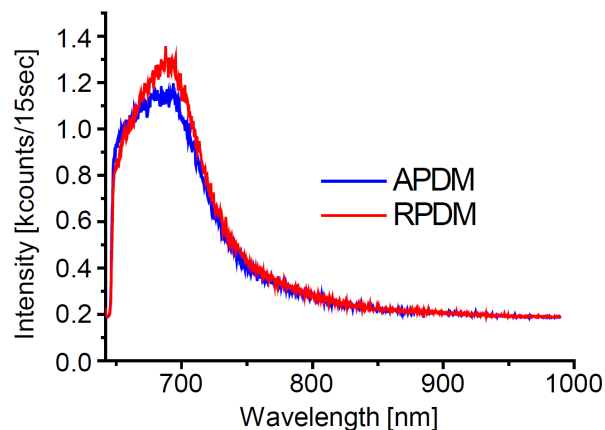
Figure 40: Luminescence spectrum of an Au-tip excited by a focused 632.8 nm wavelength radially (red) or azimuthally (blue) polarized laser beam.

The used aluminum plasmonic oligomer, like in 4.5.2, consists of 7 aluminum discs in a heptameric arrangement. The diameter of the center and the outer discs are 150 nm and 140 nm respectively while the height is 80 nm. An SEM image of the structure can be found in Figure 41b. The gaps between the particles have a size of min. 25 nm, leading to a reasonable coupling. Aluminum is chosen to shift the resonances of the oligomer to higher energies compared to the same structure made of other coinage metals.[BLA07, CHA08, LAN08] Additionally, aluminum does not emit luminescence when excited within the visible regime, enhancing the signal to noise ratio of the luminescence signal acquired from the tip.[GRY04] This structure has, as shown in Figure 39, an azimuthally excitable

resonance wavelength at 650 nm while the radially excitable resonance positions are below 400 nm. One of these oligomers is fixed exactly centered in the focus of a 632.8 nm wavelength APDM or RPDM and a sharp gold tip, see SEM image in Figure 41a, is raster scanned over the whole structure. Simultaneously, the topography and the luminescence signal are detected for each scanning step.
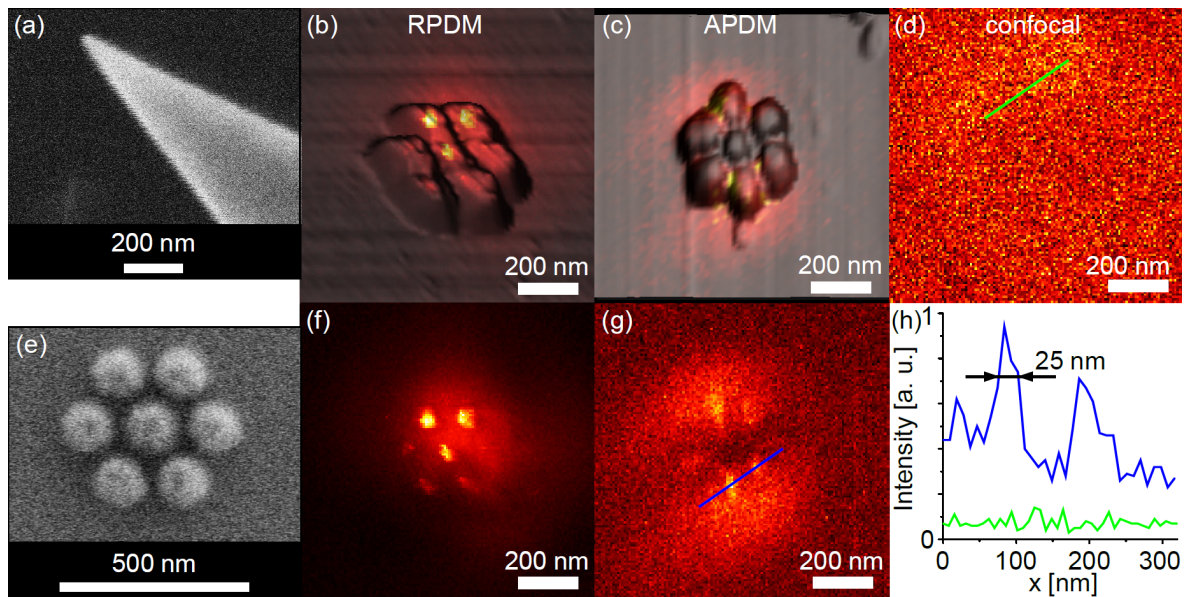
Figure 41: (a) SEM images of a typical Au-tip with an apex of >20 nm and (e) SEM image of the aluminum plasmonic oligomer. 3D topography of the aluminum heptamer in the RPDM (b) and the APDM (c) focus with the color layer representing the locally excited Au-tip luminescence intensity while the pure Au-tip luminescence images are shown in (f) for RPDM and (g) for APDM. The Au-tip luminescence measurements are in good agreement with the simulations in Figure 39. The luminescence signal (g) at tip positions inside of the gaps of the oligomer is at least two times stronger compared to the surrounding. The confocal scan image (d) of the same aluminum oligomer shows no traces of luminescence. (f) Line sections taken from the APDM tip luminescence image (g) (blue) and the confocal image (d) (green). Note, the Au-tip luminescence data are acquired at the same heptamer but with different tips and different scanning directions.

As predicted, the aluminum plasmonic oligomer does not show any luminescence when excited by a wavelength of 632.8 nm neither using the APDM nor the RPDM, see confocal image in Figure 41d. When the structure is fixed inside of the focus and scanned by the gold tip, the luminescence of the gold tip is high at the near field hotspots of the oligomer. As expected from the near field calculations, in the case of excitation with the RPDM (Figure 41b and f) the highest luminescence signal can be found on top of each of the seven discs. The strongest plasmon oscillation occurs at the center disc with a polarization

along the optical axis, i.e., along the Au-tip axis. Here a strong coupling of the plasmons in the aluminum discs with the plasmon in the Au-tip occurs. The asymmetric distribution of the luminescence signal in the direction of the upper discs in Figure 41b and f are related to a slight shift in the alignment of the heptamer towards the center of the RPDM focus.

For excitation with the APDM the highest signals are acquired in the gaps of the oligomer. Here the near fields of the oligomer are confined in the sample plane, perpendicular to the tips' main axis. An effective excitation of the Au-tip is only possible, if it dips into the near field located in the gaps between the outer discs of the oligomer. In Figure 41h an intensity profile of the confocal oligomer image (green) and the APDM tip luminescence image (blue) are compared. The FWHM of the Au-tip luminescence signal in the gaps is 25 nm, corresponding to the gap size between the particles in the aluminum plasmonic oligomer proving that the observed gold luminescence originates from the tips' apex. All images were recorded with the same excitation power of 150 µW. In the confocal cross section, as expected, only a steady background signal of about 0.8 kcounts/sec is found. The luminescence background signal of the APDM tip image has a value of 3-4 kcounts/sec and expresses some high features with 2.5 times higher luminescence intensity. The maximum signal to noise ratio for the radial case is 21 and for the azimuthal case 14.

Comparing the luminescence intensities of the two polarizations, a two times higher intensity for radially polarized excitation can be observed. This can be explained by the parallel orientation of the main axis of the Au-tip and the plasmon polarization of the plasmonic oligomers center particle, leading to an efficient energy transfer (Figure 42b). For azimuthal excitation, a perpendicular orientation of the particle plasmon polarization and the main axis of the Au-tip is present, leading to a much weaker coupling (Figure 42c).
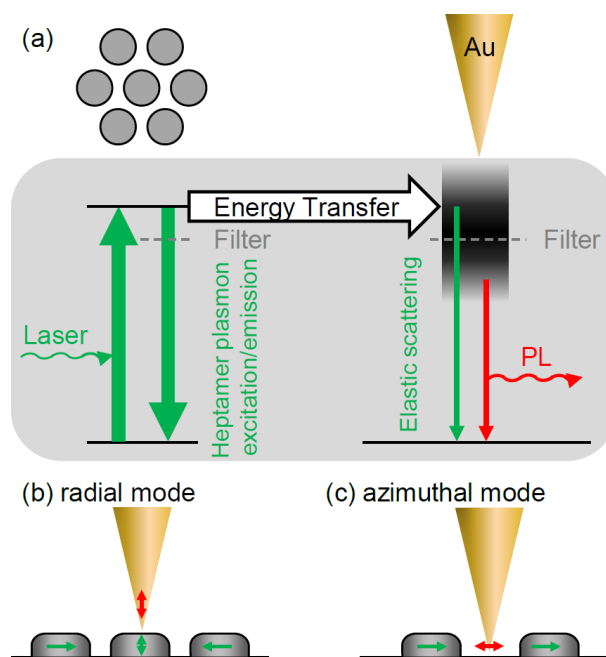
Figure 42: Sketch of the plasmonic energy transfer processes from the aluminum oligomer to the Au-tip. (a) Coupled plasmon oscillations are excited in the oligomer with λ=632.8 nm irradiation. This energy is partly stored in the optical near field which enables energy transfer from the aluminum oligomer into the gold tip. The energy of the near field excites a defined plasmon oscillation in the tip, which can release its energy either via elastic scattering or via luminescence. The elastically scattered light is completely blocked by a longpass filter in front of the detector. The two different coupling polarization configurations for radial and azimuthal illumination are shown in (b) and (c).

In Figure 42a the energy transfer process from the aluminum plasmonic oligomer to the Au-tip is schematically illustrated. The plasmonic oligomer exhibits a well defined resonance when excited by a 632.8 nm laser. The only possibilities for the plasmonic oligomer to relax into the ground state are either via elastic scattering, thermal losses or by electromagnetic near field coupling to the Au-tip. The elastic scattering of the system is not observed because of the use of a 640 nm long pass filter. The tip is acting like an optical broad band antenna, without a sharp plasmon resonance.[ZHA13] For this purpose, the energy band of the Au-tip is drawn as a broad gray-shaded area, illustrating that it can be excited by a range of wavelengths. The non-resonant behavior of the Au-tip leads to a quick relaxation either via elastic scattering, photoluminescence or nonradiatively via thermal losses.

The luminescence of the tip and the spectra of the oligomer's azimuthal plasmonic mode strongly overlap. On the other hand, the luminescence emission of the tip is strongly polarized along the tip's main axis, orthogonal to the oligomer's azimuthal mode. Due to the mismatch in the polarization direction, the tip luminescence cannot significantly populate the azimuthal mode of the oligomer and therefore the coupling is one-directional. For the radial oligomer mode the polarization of the tip luminescence matches. However, the Au-tip luminescence with $\lambda > 640$ nm is too far away of the oligomer's radial mode resonance around 350 nm to couple effectively.

To study the influence of the Au-tip to the aluminum plasmonic oligomer, the azimuthally polarized plasmonic mode of the oligomer and the perturbation of the excited near field by the Au-tip is simulated, using the surface integral method [KER09]. The azimuthal mode's relative amplitude (Figure 43 upper graph) and phase difference (Figure 43 lower graph) with respect to without the tip, in the ortho (blue), meta (red) and para gap (green) are shown. The phase shifts less than $\pi/20$ indicating a spectral shift of the mode's resonance by less than 1/10 of its total width. The shown amplitude change of approximately 10% is consistent to this result. A positive phase shift with the tip in the gap (e.g. for a tip displacement = 0) corresponds to a red shift of the mode's resonance, as is expected when increasing the coupling between the oligomer's particles. Such a small spectral shift in the plasmon resonance of the plasmonic oligomer validates that the introduction of the gold tip into the near field of the azimuthally excited oligomer has not much influence on the near fields.
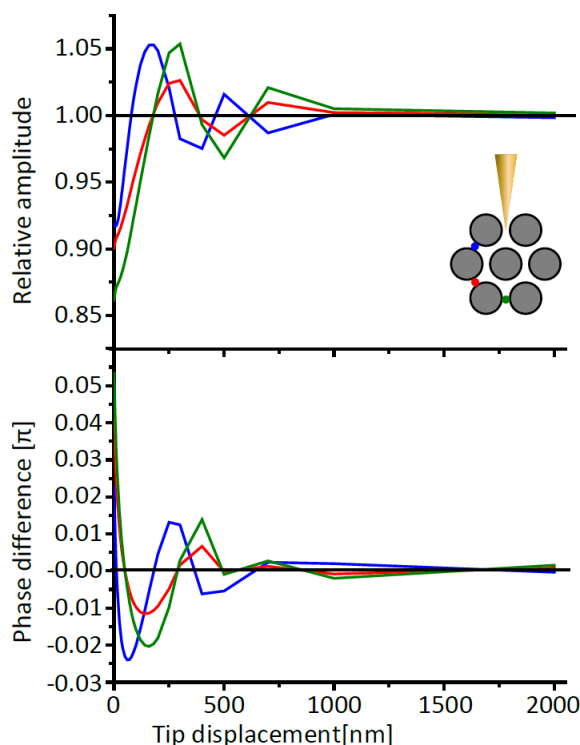
Figure 43: Simulated influence of the Au-tip to the near field of an azimuthally excited aluminum plasmonic oligomer. The tip is introduced into a gap of the oligomer and the relative amplitude (upper graph) and the phase difference (lower graph) with respect to the oligomer without tip is given for different tip heights. A tip displacement of zero corresponds to a position of the tip apex aligned with the particles centers.

As shown, the Au-tip fulfills the preconditions for the use as a near-field probe. The presence of the tip has little to no effect to the energy levels of the aluminum plasmonic oligomer. Second, the broad band antenna behavior of the tip leads to an effective unidirectional transfer of the energy from the oligomer to the tip, resulting in the observed luminescence signal of the tip. This unidirectional energy transfer has similarities to the Förster resonance energy transfer (FRET) process, where the energy is transferred from a donor molecule to a rapidly-decaying acceptor. The near-field interaction between the two plasmonic units is strong, but due to the little influence of the Au-tip on the energy levels of the oligomer, the coupling of the system stays weak. The broadband response of the tip leads to an excitability of plasmonic modes over a broad spectral range. By this, the tip can effectively enhance the excitation of electron-hole pairs as well as the emission of the luminescence by recombination of the electron hole pairs. These two enhancement processes are important for the observation of inefficient emissions like metallic photoluminescence.[KER12]

71

4.5.4. Conclusion and outlook

Plasmonic oligomers are a versatile structural element to tailor the resonance frequency of a coupled system into the desired value. In combination with radially and azimuthally polarized and so symmetry matching excitation, they are a good candidate for substitute split ring resonators in the investigation of a plasmonic magneto inductive coupling chain. In 2012 the coupling in such chains was predicted and the corresponding resonance peaks found in white light extinction spectra by Na Liu et al.[LIU12, LIU12a] Unfortunately, the whole structure is excited when the white light extinction spectra are taken, so that not a clear evidence of a real energy transport is present. Additionally, the simulations of the magnetic resonance coupling process are using a dipole placed at one gap of the structure for excitation. For a really efficient excitation of such a chain, the APDM with its symmetry matching electric field is the best candidate.

To see if these plasmonic oligomer chains are transferring the energy, the introduced method utilizing the one-photon luminescence of a sharp gold tip could be used. Here, the fact, that the intensity of the one-photon luminescence of a gold nano object has a linear dependence towards the excitation intensity is used and was shown for an aluminum heptamer excited by either the APDM or the RPDM.

5. Summary and outlook

The scope of this work is the interaction of plasmonic nano structures of cylindrical symmetry with radially and azimuthally polarized laser modes. This chapter will give a summary of the single chapters of this thesis. Following, I will present an outlook to experiments that can be based on this thesis.

5.1. Summary of the results

Chapter 1 expresses the motivation and the scope of this study and gives an outline to the structure of this thesis. In Chapter 2 the fundamentals regarding plasmons, one-photon photoluminescence of gold as well as a basic description of confocal and near-field microscopy are introduced. Additionally, the theoretical basis of the properties of cylindrical vector beams and the method to calculate their optical fields in a high numerical aperture focus is presented. The technical execution of the confocal and near field microscopes as well as of the formation of the cylindrical vector beams is described in chapter 3.

In chapter 4 the experiments are described and discussed in detail. Beginning with section 4.1 that scopes on the comparison of four different focusing/collecting elements, namely an air lens with an NA of 0.75, a parabolic mirror (NA 0.998) that also acts as an airside optical element and two oil immersion lenses with NAs of 1.25 and 1.46, respectively. As imaging object, plasmonic gold nano posts are chosen. The photoluminescence patterns of these gold nano posts are recorded at an excitation wavelength of 632.8 nm and compared to the calculated focal fields of the respective focusing element. Additionally the collecting efficiency of the different focusing/collecting elements is compared via the emission profile of a dipole at a glass air interface.

In section 4.2 the luminescence properties of gold nano discs with different sizes are compared. First, the imaging behavior of the air lens and the parabolic mirror at an air-silicon interface are discussed. For the parabolic mirror the wavelength 632.8 nm is used and for the air lens two different excitation wavelengths (514.5 and 632.8 nm) are chosen to investigate the difference in the behavior of the plasmonic nano discs. With the second wavelength (514.5 nm) different plasmonic modes are excitable and observable in the

luminescence image pattern. Two different excitabilities can be discriminated by using either the RPDM for the out of plane mode or the APDM for the in plane mode. Additionally, an analysis of the luminescence spectra is performed. Here, a trend of the plasmonic resonances for different disc sizes is observable.

The anisotropic behavior of the luminescence spectrum of gold nano cones is discussed in section 4.3. The one-photon gold photoluminescence spectra of nano cones are showing significant differences at the excitation with either the RPDM or the APDM at a wavelength of 488 nm. This difference mainly results of the concentration of charges that are driven by the RPDM into the apex of the cone. This concentration of charges has a flattening effect to the single cones, which is proven by SEM images. Additionally, the positions of the plasmon resonances are derived from the luminescence spectra and are compared with simulations.

In section 4.4, ring shaped gold nano structures and their interaction with both lasermodes, the APDM and the RPDM, is studied. The luminescence patterns formed by these structures are describable by a geometric interaction model taking into account the in plane excitability at a wavelength of 632.8 nm, which is perpendicular to the ring walls.

Section 4.5 starts with the overview of the project which focuses on the utilization of the APDM to excite plasmonic nano structures. First the excitation of split ring resonators is investigated. These split ring resonators are U-shaped gold nano structures that are acting as tiny, plasmonic LC resonators. The effective excitation of these split ring resonators with the APDM at a wavelength of 632.8 nm could not be achieved due to the mismatch of the size of a split ring resonator that is resonant to this wavelength and the size of the APDM focus. As an alternative structure, plasmonic oligomers are used. The excitability of such plasmonic oligomers with structure sizes comparable to a 632.8 nm wavelength APDM focus is much easily tunable, i.e. by switching from gold to aluminum. Therefore, a theoretical description of the interaction between the APDM and the RPDM focus with a heptameric structure is discussed. Herein, a strong, ring shaped coupling by excitation of the heptameric structure with the APDM is predicted. To experimentally prove this high near field coupling of the heptameric structure in the APDM focus, a new near field microscopy operating mode is developed. Here, the one-photon gold photoluminescence of a sharp gold tip is utilized to detect the strong near fields of the heptameric structure.

5.2. Outlook

In this thesis, the principle excitability of plasmonic nano structures with CVBs has been demonstrated. For future work, two types of structures have the highest potential: the gold nano cones and the plasmonic oligomers.

The gold nano cones can, due to their shape, concentrate the plasmons at their apex. This hot spot is the perfect location to study the interaction between plasmonic nano structures and single quantum emitters like single molecules or quantum dots. Therefore the single quantum emitter has to be localized within the region of the high near field at the apex of the cone. This could be achieved by utilizing the gold affinity of thiol functional groups to couple a dye or a quantum dot directly to the gold. To selectively bind the thiol to the apex of the gold cone, a passivation of the cones flanks has to be performed prior to the functionalization. Alternatively, a process similar to the near field assisted polymerization could be used. The cone would be completely layered by a photo resist monomer. Afterwards the cones are illuminated by radially polarized light that forms a near field at the apex of the cone. In this near field, the intensity of the electromagnetic field is high enough to polymerize the monomer. Either, the monomer solution could already contain dye molecules or quantum dots that are fixed by the polymerization process to the apex of the cone or only the polymer at the apex could be functionalized to bind a quantum emitter directly. A second technique to place such quantum emitters to the apex of the tip utilizes a sharp silicon or glass AFM tip, where the emitter is attached to. With this technique, the position of the emitter can be controlled with respect to the position of the cone.

The principle of plasmonic oligomers can be extended consequently towards a waveguide that uses the magneto inductive coupling mechanism. This was already demonstrated in 2012 by Liu et al. where the authors build a wave guiding system consisting of hexagonal oriented single discs.[LIU12, LIU12a] The coupling into such a waveguide can be much more effective by using the APDM. Here, the SNOM method presented in chapter 4.5 can be used to prove the wave guiding effect more specifically.

The SNOM technique, utilizing the gold luminescence of a sharp gold tip, could be adapted to a wider range. In our experiments, the investigated plasmonic oligomer consists

of aluminum and thus doesn't emit any luminescence (in the spectral region of interest). In principle, this method should also work for luminescent materials like gold, where the luminescence of the structure creates a higher background signal. Proving this method to be adaptable to luminescent structures, would open this operation mode to a wide range of experiments.

5.3. Zusammenfassung

Das Ziel dieser Arbeit ist die Wechselwirkung zwischen plasmonischen Nanostrukturen zylindrischer Symmetrie mit radial und azimutal polarisierten Laserstrahlen zu untersuchen. In Kapitel 1 wird die Motivation für diese Arbeit zum Ausdruck gebracht sowie eine Übersicht über den Aufbau dieser Monographie gegeben. Das Kapitel 2 führt ein in die Grundlagen zu den Themen Plasmonen, Einphotonenlumineszenz von Gold, konfokale- und Nahfeld-Mikroskopie sowie zu den Eigenschaften von Zylindersymmetrischen Vektor-Strahlen (CVB). Zudem wird eine Methode zur Berechnung der optischen Felder von fokussierten CVBs im Fokus von Mikroskopobjektiven mit hoher Numerischer Apertur vorgestellt. Die technische Ausführung des konfokalen- und Nahfeld-optischen Mikroskops sowie die Erzeugung der Zylindersymmetrischen Vektor-Strahlen sind in Kapitel 3 ausgeführt.

In Kapitel 4 werden die einzelnen Experimente im Detail beschrieben und diskutiert. Zunächst wird in Abschnitt 4.1 ein Vergleich zwischen vier verschiedenen fokussierenden/sammelnden optischen Elementen durchgeführt. Dies sind: Ein Luftobjektiv mit einer NA von 0.75, ein Parabolspiegel mit einer NA von 0.998, der ebenfalls in Luft arbeitet, und zwei Ölimmersionsobjektive mit den Numerischen Aperturen 1.25 und 1.46. Als abzubildendes Objekt werden plasmonische Gold-Nanopfosten verwendet. Die Lumineszenzmuster dieser Gold-Nanopfosten werden bei einer Anregungswellenlänge von 632.8 nm aufgenommen und mit den berechneten fokalen Feldern der einzelnen fokussierenden optischen Elemente verglichen. Außerdem wird die Sammeleffizienz der verschiedenen fokussierenden/sammelnden optischen Elemente mittels Emissionsverhalten eines Dipols nahe einer Glasoberfläche verglichen.

Die Lumineszenz-Charakteristika einzelner, Gold Nanoscheiben verschiedener Größe werden in Abschnitt 4.2 verglichen. Zuerst werden die Abbildungseigenschaften des

Luftobjektivs und des Parabolspiegels an einer Luft-Silizium Grenzfläche erörtert. Bei den Experimenten mit dem Parabolspiegel wird die Wellenlänge 632.8 nm und im Fall des Luftobjektivs werden zwei verschiedene Anregungswellenlängen (524.5 und 632.8 nm) zur Untersuchung der Unterschiede im plasmonischen Verhalten der Nanoscheiben verwendet. Mit der zweiten Wellenlänge (514.5 nm) können andere plasmonische Moden angeregt werden. Diese Unterschiede können in den Lumineszenzmustern beobachtet werden. Zwei verschiedene Anregungsrichtungen können durch die Verwendung entweder des RPDM, für die zur Ebene senkrechte Mode, oder durch die Verwendung des APDM, für die zur Ebene parallele Mode, unterschieden werden. Durch eine zusätzliche Analyse von gemessenen Lumineszenzspektren, wird der Trend der Plasmonenresonanzen für verschiedene Scheibengrößen deutlich.

Das anisotrope Verhalten des Lumineszenzspektrums von Gold Nanokegeln wird in 4.3 diskutiert. Die Einphotonen-Gold-Lumineszenzspektren der Gold Nanokegel weisen signifikante Unterschiede zwischen der Anregung mit RPDM und APDM bei einer Wellenlänge von 488 nm auf. Dieser Unterschied resultiert hauptsächlich aus der, durch die Anregung mit der RPDM hervorgerufenen, Konzentrierung von Ladungen in der Spitze des Kegels. Diese Konzentrierung von Ladungen hat zudem einen abflachenden Effekt auf die Geometrie der Kegel, was durch Rasterelektronenmikroskopische aufnahmen nachgewiesen wird. Zusätzlich wird die Position der Plasmonenresonanzen aus den Lumineszenzspektren abgeleitet und mit Simulationsergebnissen verglichen.

In Kapitel 4.4 wird die Interaktion zwischen ringförmigen Gold Nanostrukturen und den beiden Lasermoden APDM und RPDM untersucht. Die durch diese Interaktion entstehenden Lumineszenzmuster werden durch ein geometrisches Modell beschrieben, welches die Anregbarkeit der Gold Nanoringen in der Ebene bei einer Wellenlänge von 632.8 nm (senkrecht zur Ringwand) berücksichtigt.

Das Kapitel 4.5 beginnt mit einem Überblick über das Projekt das sich mit der Verwendung des APDM zur Anregung plasmonischer Strukturen beschäftigt. Zuerst wird die Anregung von „Split-Ring" Resonatoren untersucht. Diese Split-Ring Resonatoren sind U-förmige Gold Nanostrukturen welche wie kleine, plasmonische Schwingkreise agieren. Zunächst wurden Split-Ring Resonatoren, die resonant zur Wellenlänge 632.8 nm sind, durch einen fokussierten APDM untersucht. Aufgrund einer physikalischen Diskrepanz zwischen der Größe eines bei 632.8 nm resonanten Split-Ring Resonators und der Größe

des APDM Fokus konnte eine effiziente Anregung nicht erreicht werden. Als eine alternative Struktur werden daher plasmonische Oligomere untersucht. Die Anregbarkeit von solchen plasmonischen Oligomeren, welche eine mit einem 632.8 nm APDM Fokus vergleichbare Größe haben, ist einfacher zu realisieren. Dies wurde durch den Wechsel von Gold zu Aluminium erreicht. So werden die Wechselwirkungen der APDM und RPDM mit einer heptameren Struktur aus Aluminium berechnet. Durch theoretische Beschreibung der Interaktion zwischen einem heptameren Oligomer und den Foki des APDM und des RPDM werden starke, ringförmig angeordnete Kopplungen bei der durch den APDM Fokus angeregten heptameren Struktur vorhergesagt. Um diese starke Nahfeldkopplung der heptameren Struktur im APDM Fokus nachweisen zu können wurde eine neuartige Betriebsart für die Nahfeldoptische Mikroskopie entwickelt. Diese Methode nutzt die Einphotonen-Gold-Lumineszenz einer sehr scharfen Goldspitze um die starken Nahfelder der heptameren Struktur sichtbar zu machen.

6. References

[AIZ03]   Aizpurua, J.; Hanarp, P.; Sutherland, D. S.; Kall, M.; Bryant, G. W.; Garcia de Abajo, F. J., Optical properties of gold nanorings. *Physical Review Letters* 2003, 90, 057401.

[ALE08]   Alegret, J.; Rindzevicius, T.; Pakizeh, T.; Alaverdyan, Y.; Gunnarsson, L.; Kall, M., Plasmonic properties of silver trimers with trigonal symmetry fabricated by electron-beam lithography. *Journal of Physical Chemistry C* 2008, 112, 14313-14317.

[ALO11]   Alonso-Gonzalez, P.; Schnell, M.; Sarriugarte, P.; Sobhani, H.; Wu, C.; Arju, N.; Khanikaev, A.; Golmar, F.; Albella, P.; Arzubiaga, L.; Casanova, F.; Hueso, L. E.; Nordlander, P.; Shvets, G.; Hillenbrand, R., Real-space mapping of Fano interference in plasmonic metamolecules. *Nano Letters* 2011, 11, 3922-6.

[ANK08]   Anker, J. N.; Hall, W. P.; Lyandres, O.; Shah, N. C.; Zhao, J.; Van Duyne, R. P., Biosensing with plasmonic nanosensors. *Nature materials* 2008, 7, 442-53.

[BEV03]   Beversluis, M. R.; Bouhelier, A.; Novotny, L., Continuum generation from single gold nanostructures through near-field mediated intraband transitions. *Physical Review B* 2003, 68, 115433.

[BIA12]   Biagioni, P.; Brida, D.; Huang, J. S.; Kern, J.; Duo, L.; Hecht, B.; Finazzi, M.; Cerullo, G., Dynamics of four-photon photoluminescence in gold nanoantennas. *Nano Letters* 2012, 12, 2941-7.

[BLA07]   Blaber, M. G.; Arnold, M. D.; Harris, N.; Ford, M. J.; Cortie, M. B., Plasmon absorption in nanospheres: A comparison of sodium, potassium, aluminium, silver and gold. *Physica B* 2007, 394, 184-187.

[BOH83]   Bohren, C. F.; Huffman, D. R., *Absorption and scattering of light by small particles*; Wiley: 1983.

[BOU05]   Bouhelier, A.; Bachelot, R.; Lerondel, G.; Kostcheev, S.; Royer, P.; Wiederrecht, G. P., Surface plasmon characteristics of tunable photoluminescence in single gold nanorods. *Physical review letters* 2005, 95, 267405.

[BOU03]   Bouhelier, A.; Beversluis, M. R.; Novotny, L., Characterization of nanoplasmonic structures by locally excited photoluminescence. *Applied Physics Letters* 2003, 83, 5041-5043.

[BOY86]   Boyd, G. T.; Yu, Z. H.; Shen, Y. R., Photoinduced luminescence from the noble metals and its enhancement on roughened surfaces. *Phys. Rev. B Condens. Matter* 1986, 33, 7923-7936.

[BRA07]   Braun, K. Aufbau und Charakterisierung eines Nahfeldmoduls für nahfeldoptische Untersuchungen in einem Parabolspiegelmikroskop. Diploma Thesis, Universität Tübingen, 2007.

[CAM08]   Camden, J. P.; Dieringer, J. A.; Zhao, J.; Van Duyne, R. P., Controlled plasmonic nanostructures for surface-enhanced spectroscopy and sensing. *Accounts Chem Res* 2008, 41, 1653-1661.

[CHA08]   Chan, G. H.; Zhao, J.; Schatz, G. C.; Van Duyne, R. P., Localized surface plasmon resonance spectroscopy of triangular aluminum nanoparticles. *Journal of Physical Chemistry C* 2008, 112, 13958-13963.

[CHE09]   Chen, W. B.; Abeysinghe, D. C.; Nelson, R. L.; Zhan, Q. W., Plasmonic Lens Made of Multiple Concentric Metallic Rings under Radially Polarized Illumination. *Nano Letters* 2009, 9, 4320-4325.

[DAV96]   Davy, S.; Spajer, M., Near field optics: Snapshot of the field emitted by a nanosource using a photosensitive polymer. *Applied Physics Letters* 1996, 69, 3306-3308.

[DEE10]   Deeb, C.; Bachelot, R.; Plain, J.; Baudrion, A. L.; Jradi, S.; Bouhelier, A.; Soppera, O.; Jain, P. K.; Huang, L.; Ecoffet, C.; Balan, L.; Royer, P., Quantitative analysis of localized surface plasmons based on molecular probing. *ACS Nano* 2010, 4, 4579-86.

[DIE06]   Dieringer, J. A.; McFarland, A. D.; Shah, N. C.; Stuart, D. A.; Whitney, A. V.; Yonzon, C. R.; Young, M. A.; Zhang, X. Y.; Van Duyne, R. P., Surface enhanced Raman spectroscopy: new materials, concepts, characterization tools, and applications. *Faraday Discussions* 2006, 132, 9-26.

[DOR64]   Doremus, R. H., Optical Properties of Small Gold Particles. *The Journal of Chemical Physics* 1964, 40, 2389-2396.

[DOR03]   Dorn, R.; Quabis, S.; Leuchs, G., Sharper focus for a radially polarized light beam. *Physical review letters* 2003, 91, 233901.

[DRE11]   Dregely, D.; Hentschel, M.; Giessen, H., Excitation and tuning of higher-order Fano resonances in plasmonic oligomer clusters. *ACS Nano* 2011, 5, 8202-11.

[DUL04]   Dulkeith, E.; Niedereichholz, T.; Klar, T. A.; Feldmann, J.; von Plessen, G.; Gittins, D. I.; Mayya, K. S.; Caruso, F., Plasmon emission in photoexcited gold nanoparticles. *Physical Review B* 2004, 70, 205424.

[FAI07]   Failla, A. V.; Jager, S.; Zuchner, T.; Steiner, M.; Meixner, A. J., Topology measurements of metal nanoparticles with 1 nm accuracy by Confocal Interference Scattering Microscopy. *Optics Express* 2007, 15, 8532-42.

[FAN10]   Fan, J. A.; Wu, C.; Bao, K.; Bao, J.; Bardhan, R.; Halas, N. J.; Manoharan, V. N.; Nordlander, P.; Shvets, G.; Capasso, F., Self-assembled plasmonic nanoparticle clusters. *Science* 2010, 328, 1135-8.

[FAN12]   Fang, Y.; Chang, W. S.; Willingham, B.; Swanglap, P.; Dominguez-Medina, S.; Link, S., Plasmon emission quantum yield of single gold nanorods as a function of aspect ratio. *ACS Nano* 2012, 6, 7177-84.

[FLE08]   Fleischer, M.; Stanciu, C.; Stade, F.; Stadler, J.; Braun, K.; Heeren, A.; Haffner, M.; Kern, D. P.; Meixner, A. J., Three-dimensional optical antennas: Nanocones in an apertureless scanning near-field microscope. *Applied Physics Letters* 2008, 93, 111114.

[FUL14]   Fulmes, J.; Schäfer, C.; Jäger, S.; Gollmer, D. A.; Horrer, A.; Zhang, D.; Adam, P.-M.; Meixner, A. J.; Kern, D. P.; Fleischer, M., Mapping the electric field distribution of cylindrical vector beams with gold nanorings. 2014 (in preparation).

[GRY04]   Gryczynski, I.; Malicka, J.; Gryczynski, Z.; Nowaczyk, K.; Lakowicz, J. R., Ultraviolet surface plasmon-coupled emission using thin aluminum films. *Analytical Chemistry* 2004, 76, 4076-81.

[HAE04]   Haefliger, D.; Plitzko, J. M.; Hillenbrand, R., Contrast and scattering efficiency of scattering-type near-field optical probes. *Applied Physics Letters* 2004, 85, 4466-4468.

[HAO08]   Hao, F.; Larsson, E. M.; Ali, T. A.; Sutherland, D. S.; Nordlander, P., Shedding light on dark plasmons in gold nanorings. *Chemical Physics Letters* 2008, 458, 262-266.

[HAY03]   Haynes, C. L.; Van Duyne, R. P., Plasmon-sampled surface-enhanced Raman excitation spectroscopy. *Journal of Physical Chemistry B* 2003, 107, 7426-7433.

[HEC00]   Hecht, B.; Sick, B.; Wild, U. P.; Deckert, V.; Zenobi, R.; Martin, O. J. F.; Pohl, D. W., Scanning near-field optical microscopy with aperture probes: Fundamentals and applications. *Journal of Chemical Physics* 2000, 112, 7761-7774.

[HEN12]   Hennemann, L. E.; Kolloch, A.; Kern, A.; Mihaljevic, J.; Boneberg, J.;
           Leiderer, P.; Meixner, A. J.; Zhang, D., Assessing the plasmonics of gold
           nano-triangles with higher order laser modes. *Beilstein journal of
           nanotechnology* 2012, 3, 674-83.

[HEN13]   Hentschel, M.; Dorfmuller, J.; Giessen, H.; Jager, S.; Kern, A. M.; Braun,
           K.; Zhang, D.; Meixner, A. J., Plasmonic oligomers in cylindrical vector
           light beams. *Beilstein journal of nanotechnology* 2013, 4, 57-65.

[HEN11]   Hentschel, M.; Dregely, D.; Vogelgesang, R.; Giessen, H.; Liu, N.,
           Plasmonic oligomers: the role of individual particles in collective behavior.
           ACS Nano 2011, 5, 2042-50.

[HEN10]   Hentschel, M.; Saliba, M.; Vogelgesang, R.; Giessen, H.; Alivisatos, A. P.;
           Liu, N., Transition from isolated to collective modes in plasmonic
           oligomers. *Nano Letters* 2010, 10, 2721-6.

[HES07]   Hesmer, F.; Tatartschuk, E.; Zhuromskyy, O.; Radkovskaya, A. A.;
           Shamonin, M.; Hao, T.; Stevens, C. J.; Faulkner, G.; Edwards, D. J.;
           Shamonina, E.; Hao, T.; Stevens, C. J.; Faulkner, G.; Edwards, D. J.;
           Shamonina, E., Coupling mechanisms for split ring resonators: Theory and
           experiment. *Phys Status Solidi B* 2007, 244, 1170-1175.

[HIL01]   Hillenbrand, R.; Knoll, B.; Keilmann, F., Pure optical contrast in scattering-
           type scanning near-field microscopy. *Journal of microscopy* 2001, 202, 77-
           83.

[HU12]   Hu, H.; Duan, H.; Yang, J. K.; Shen, Z. X., Plasmon-modulated
           photoluminescence of individual gold nanostructures. *ACS Nano* 2012, 6,
           10147-55.

[HUB08]   Hubert, C.; Bachelot, R.; Plain, J.; Kostcheev, S.; Lerondel, G.; Juan, M.;
           Royer, P.; Zou, S. L.; Schatz, G. C.; Wiederrecht, G. P.; Gray, S. K., Near-
           field polarization effects in molecular-motion-induced photochemical
           imaging. *Journal of Physical Chemistry C* 2008, 112, 4111-4116.

[HUS11]   Huss, A. Investigations and optical manipulations of gold nanostructures
           using cylindrical vector beams. Diploma Thesis, Universität Tübingen,
           2011.

[JAE13a]   Jäger, R.; Chizhik, A. M.; Chizhik, A. I.; Wackenhut, F.; Meixner, A. J.,
           Cylindrical Vector Beams for Spectroscopic Imaging of Single Molecules
           and Nanoparticles. In *Vectorial Optical Fields: Fundamentals and
           Applications*, Zhan, Q., Ed. World Scientific Publishing Company
           Incorporated: 2013.

[JAE13]   Jäger, S.; Kern, A. M.; Hentschel, M.; Jäger, R.; Braun, K.; Zhang, D.; Giessen, H.; Meixner, A. J., Au Nanotip as Luminescent Near-Field Probe. *Nano Letters* 2013, 13, 3566–3570.

[JAI10]   Jain, P. K.; El-Sayed, M. A., Plasmonic coupling in noble metal nanostructures. *Chemical Physics Letters* 2010, 487, 153-164.

[JAI06]   Jain, P. K.; Eustis, S.; El-Sayed, M. A., Plasmon coupling in nanorod assemblies: optical absorption, discrete dipole approximation simulation, and exciton-coupling model. *The Journal of Physical Chemistry B* 2006, 110, 18243-53.

[JOU13]   Joud, F.; Warnasooriya, N.; Bun, P.; Verpillat, F.; Suck, S. Y.; Tessier, G.; Atlan, M.; Desbiolles, P.; Coppey-Moisan, M.; Abboud, M.; Gross, M., 3D exploration of light scattering from live cells in the presence of gold nanomarkers using holographic microscopy. *3D Res* 2011, 2, 1-8.

[KAL01]   Kalkbrenner, T.; Ramstein, M.; Mlynek, J.; Sandoghdar, V., A single gold particle as a probe for apertureless scanning near-field optical microscopy. *Journal of Microscopy-Oxford* 2001, 202, 72-76.

[KEL03]   Kelly, K. L.; Coronado, E.; Zhao, L. L.; Schatz, G. C., The Optical Properties of Metal Nanoparticles: The Influence of Size, Shape, and Dielectric Environment. *Journal of Physical Chemistry B* 2003, 107, 668-677.

[KER09]   Kern, A. M.; Martin, O. J., Surface integral formulation for 3D simulations of plasmonic and high permittivity nanostructures. *Journal of the Optical Society of America. A, Optics, image science, and vision* 2009, 26, 732-40.

[KER12]   Kern, A. M.; Meixner, A. J.; Martin, O. J., Molecule-dependent plasmonic enhancement of fluorescence and Raman scattering near realistic nanostructures. *ACS Nano* 2012, 6, 9828-36.

[KRE71]   Kretschmann, E., Die Bestimmung optischer Konstanten von Metallen durch Anregung von Oberflächenplasmaschwingungen. *Z. Physik* 1971, 241, 313-324.

[KUE01]   Kühn, S.; Hettich, C.; Schmitt, C.; Poizat, J. P.; Sandoghdar, V., Diamond colour centres as a nanoscopic light source for scanning near-field optical microscopy. *Journal of Microscopy* 2001, 202, 2-6.

[LAM00]   Lamprecht, B.; Schider, G.; Lechner, R. T.; Ditlbacher, H.; Krenn, J. R.; Leitner, A.; Aussenegg, F. R., Metal nanoparticle gratings: Influence of dipolar particle interaction on the plasmon resonance. *Physical Review Letters* 2000, 84, 4721-4724.

[LAN08]   Langhammer, C.; Schwind, M.; Kasemo, B.; Zoric, I., Localized surface plasmon resonances in aluminum nanodisks. *Nano Letters* 2008, 8, 1461-71.

[LAR07]   Larsson, E. M.; Alegret, J.; Kall, M.; Sutherland, D. S., Sensing Characteristics of NIR Localized Surface Plasmon Resonances in Gold Nanorings for Application as Ultrasensitive Biosensors. *Nano Letters* 2007, 7, 1256-1263.

[LAU98]   Laux, S.; Kaiser, N.; Zöller, A.; Götzelmann, R.; Lauth, H.; Bernitzki, H., Room-temperature deposition of indium tin oxide thin films with plasma ion-assisted evaporation. *Thin Solid Films* 1998, 335, 1-5.

[LIE01]   Lieb, M. A. Mikroskopie mit Parabolspiegeloptik. PhD Thesis, Universität Siegen, 2001.

[LIE01a] Lieb, M. A.; Meixner, A. J., A high numerical aperture parabolic mirror as imaging device for confocal microscopy. *Optics Express* 2001, 8, 458-474.

[LIN10]   Lin, H. Y.; Huang, C. H.; Chang, C. H.; Lan, Y. C.; Chui, H. C., Direct near-field optical imaging of plasmonic resonances in metal nanoparticle pairs. *Optics express* 2010, 18, 165-72.

[LIN04]   Linden, S.; Enkrich, C.; Wegener, M.; Zhou, J. F.; Koschny, T.; Soukoulis, C. M., Magnetic response of metamaterials at 100 terahertz. *Science* 2004, 306, 1351-1353.

[LIN99]   Link, S.; Mohamed, M. B.; El-Sayed, M. A., Simulation of the optical absorption spectra of gold nanorods as a function of their aspect ratio and the effect of the medium dielectric constant. *Journal of Physical Chemistry B* 1999, 103, 3073-3077.

[LIU08]   Liu, N.; Kaiser, S.; Giessen, H., Magnetoinductive and Electroinductive Coupling in Plasmonic Metamaterial Molecules. *Advanced Materials* 2008, 20, 4521-4525.

[LIU12]   Liu, N.; Mukherjee, S.; Bao, K.; Brown, L. V.; Dorfmuller, J.; Nordlander, P.; Halas, N. J., Magnetic plasmon formation and propagation in artificial aromatic molecules. *Nano Letters* 2012, 12, 364-9.

[LIU12a] Liu, N.; Mukherjee, S.; Bao, K.; Li, Y.; Brown, L. V.; Nordlander, P.; Halas, N. J., Manipulating Magnetic Plasmon Propagation in Metallic Nanocluster Networks. *Acs Nano* 2012.

[LUK10]   Luk'yanchuk, B.; Zheludev, N. I.; Maier, S. A.; Halas, N. J.; Nordlander, P.; Giessen, H.; Chong, C. T., The Fano resonance in plasmonic nanostructures and metamaterials. *Nature materials* 2010, 9, 707-15.

[MAI07]   Maier, S. A., *Plasmonics: Fundamentals and Applications*; Springer
             Science+Business Media, LLC: 2007.

[MAI60]   Maiman, T. H., Stimulated Optical Radiation in Ruby. *Nature* 1960, 187,
             493-494.

[MAL01]   Malinsky, M. D.; Kelly, K. L.; Schatz, G. C.; Van Duyne, R. P., Nanosphere
             lithography: Effect of substrate on the localized surface plasmon resonance
             spectrum of silver nanoparticles. *Journal of Physical Chemistry B* 2001,
             105, 2343-2350.

[MCF03]   McFarland, A. D.; VanDuyne, R. P., Single Silver Nanoparticles as Real-
             Time Optical Sensors with Zeptomole Sensitivity. *Nano Letters* 2003, 3,
             1057-1062.

[MIC00]   Michaelis, J.; Hettich, C.; Mlynek, J.; Sandoghdar, V., Optical microscopy
             using a single-molecule light source. *Nature* 2000, 405, 325-328.

[MIE08]   Mie, G., Beiträge zur Optik trüber Medien, speziell kolloidaler
             Metallösungen. *Annalen der Physik* 1908, 330, 377-445.

[MIN57]   Minsky, M. Microscopy Apparatus. US003013467, 19 Dec. 1961, 1957.

[MIR09]   Mirin, N. A.; Bao, K.; Nordlander, P., Fano resonances in plasmonic
             nanoparticle aggregates. *The Journal of Physical Chemistry A* 2009, 113,
             4028-34.

[MOH00]   Mohamed, M. B.; Volkov, V.; Link, S.; El-Sayed, M. A., The 'lightning'
             gold nanorods: fluorescence enhancement of over a million compared to the
             gold metal. *Chemical Physics Letters* 2000, 317, 517-523.

[MOO69]   Mooradian, A., Photoluminescence of Metals. *Physical Review Letters*
             1969, 22, 185-187.

[NIK03]   Nikoobakht , B.; El-Sayed, M. A., Preperation and Growth Mechanism of
             Gold Nanorods (NRs) Using Seed-Mediated Growth Method. *Chemestry of
             Materials* 2003, 15, 1957 - 1962.

[NOV06]   Novotny, L.; Hecht, B., *Principles of Nano-Optics*, 1 ed.; Cambridge
             University Press: 2006; p 539.

[NOV06a]   Novotny, L.; Stranick, S. J., Near-field optical microscopy and spectroscopy
             with pointed probes. *Annual review of physical chemistry* 2006, 57, 303-31.

[NOV11]   Novotny, L.; van Hulst, N., Antennas for light. *Nature Photonics* 2011, 5,
             83-90.

[PER05]   Perez-Juste, J.; Pastoriza-Santos, I.; Liz-Marzan, L. M.; Mulvaney, P., Gold nanorods: Synthesis, characterization and applications. *Coordination Chemistry Reviews* 2005, 249, 1870-1901.

[PRO03]   Prodan, E.; Radloff, C.; Halas, N. J.; Nordlander, P., A hybridization model for the plasmon response of complex nanostructures. *Science* 2003, 302, 419-22.

[RAE88]   Raether, H., *Surface Plasmons on Smooth and Rough Surfaces and on Gratings*: Springer Verlag, 1988; Vol. 111, p 136.

[RAY96]   Rayleigh, L., On the theory of optical images, with special reference to the microscope. *Philosophical Magazine Series 5* 1896, 42, 167-195.

[RIC59]   Richards, B.; Wolf, E., Electromagnetic Diffraction in Optical Systems. II. Structure of the Image Field in an Aplanatic System. *Proceedings of the Royal Society of London. Series A. Mathematical and Physical Sciences* 1959, 253, 358-379.

[SAC08]   Sackrow, M.; Stanciu, C.; Lieb, M. A.; Meixner, A. J., Imaging nanometre-sized hot spots on smooth Au films with high-resolution tip-enhanced luminescence and Raman near-field optical microscopy. *Chemphyschem* 2008, 9, 316-320.

[SAH12]   Saha, K.; Agasti, S. S.; Kim, C.; Li, X.; Rotello, V. M., Gold nanoparticles in chemical and biological sensing. *Chemical reviews* 2012, 112, 2739-79.

[SCH13]   Schafer, C.; Gollmer, D. A.; Horrer, A.; Fulmes, J.; Weber-Bargioni, A.; Cabrini, S.; Schuck, P. J.; Kern, D. P.; Fleischer, M., A single particle plasmon resonance study of 3D conical nanoantennas. *Nanoscale* 2013.

[SCH08]   Schmelzeisen, M.; Austermann, J.; Kreiter, M., Plasmon mediated confocal dark-field microscopy. *Optics Express* 2008, 16, 17826-41.

[SHA11]   Shah, N. B.; Dong, J.; Bischof, J. C., Cellular uptake and nanoscale localization of gold nanoparticles in cancer using label-free confocal Raman microscopy. *Molecular pharmaceutics* 2011, 8, 176-84.

[SHA12]   Shahbazyan, T. V., Theory of plasmon-enhanced metal photoluminescence. *Nano Letters* 2012.

[SIE86]   Siegman, A. E., *Lasers*; University science books: 1986; p 1283.

[SOE01]   Sönnichsen, C. Plasmons in metal nanostructures. Dissertation, Ludwigs-Maximilians-Universität München, 2001.

[SOE05]   Sönnichsen, C.; Reinhard, B. M.; Liphardt, J.; Alivisatos, A. P., A molecular ruler based on plasmon coupling of single gold and silver nanoparticles. *Nat Biotechnol* 2005, 23, 741-745.

[STA07]   Stade, F.; Heeren, A.; Fleischer, M.; Kern, D. P., Fabrication of metallic nanostructures for investigating plasmon-induced field enhancement. *Microelectronic Engineering* 2007, 84, 1589-1592.

[STA96]   Stalder, M.; Schadt, M., Linearly polarized light with axial symmetry generated by liquid-crystal polarization converters. *Optics Letters* 1996, 21, 1948-1950.

[STE08]   Steiner, M.; Debus, C.; Failla, A. V.; Meixner, A. J., Plasmon-enhanced emission in gold nanoparticle aggregates. *Journal of Physical Chemistry C* 2008, 112, 3103-3108.

[STE60]   Stern, E. A.; Ferrell, R. A., Surface Plasma Oscillations of a Degenerate Electron Gas. *Physical Review* 1960, 120, 130-136.

[SUA07]   Suarez, M. A.; Grosjean, T.; Charraut, D.; Courjon, D., Nanoring as a magnetic or electric field sensitive nano-antenna for near-field optics applications. *Optics Communications* 2007, 270, 447-454.

[TCH11]   Tcherniak, A.; Dominguez-Medina, S.; Chang, W. S.; Swanglap, P.; Slaughter, L. S.; Landes, C. F.; Link, S., One-Photon Plasmon Luminescence and Its Application to Correlation Spectroscopy as a Probe for Rotational and Translational Dynamics of Gold Nanorods. *Journal of Physical Chemistry C* 2011, 115, 15938-15949.

[VER09]   Verellen, N.; Sonnefraud, Y.; Sobhani, H.; Hao, F.; Moshchalkov, V. V.; Van Dorpe, P.; Nordlander, P.; Maier, S. A., Fano Resonances in Individual Coherent Plasmonic Nanocavities. *Nano Letters* 2009, 9, 1663-1667.

[WAC13]   Wackenhut, F.; Failla, A. V.; Meixner, A. J., Multicolor Microscopy and Spectroscopy Reveals the Physics of the One-Photon Luminescence in Gold Nanorods. *The Journal of Physical Chemistry C* 2013, 117, 17870-17877.

[WAC12]   Wackenhut, F.; Failla, A. V.; Zuchner, T.; Steiner, M.; Meixner, A. J., Three-dimensional photoluminescence mapping and emission anisotropy of single gold nanorods. *Applied Physics Letters* 2012, 100, 263102-4.

[WAN07]   Wang, H.; Brandl, D. W.; Nordlander, P.; Halas, N. J., Plasmonic nanostructures: artificial molecules. *Accounts Chem Res* 2007, 40, 53-62.

[WHI05]   Whitney, A. V.; Elam, J. W.; Zou, S.; Zinovev, A. V.; Stair, P. C.; Schatz, G. C.; VanDuyne, R. P., Localized Surface Plasmon Resonance

Nanosensor: A High-Resolution Distance-Dependence Study Using Atomic Layer Deposition. *Journal of Physical Chemistry B* 2005, 109, 20522-20528.

[WIL06]   Willets, K. A.; Van Duyne, R. P., Localized surface plasmon resonance spectroscopy and sensing. *Annu. Rev. Phys. Chem.* 2007, 58, 267-97.

[WOL59]   Wolf, E., Electromagnetic Diffraction in Optical Systems. I. An Integral Representation of the Image Field. *Proceedings of the Royal Society of London. Series A. Mathematical and Physical Sciences* 1959, 253, 349-357.

[YE12]   Ye, J.; Wen, F.; Sobhani, H.; Lassiter, J. B.; Van Dorpe, P.; Nordlander, P.; Halas, N. J., Plasmonic nanoclusters: near field properties of the Fano resonance interrogated with SERS. *Nano Letters* 2012, 12, 1660-7.

[YOR12]   Yorulmaz, M.; Khatua, S.; Zijlstra, P.; Gaiduk, A.; Orrit, M., Luminescence quantum yield of single gold nanorods. *Nano Letters* 2012, 12, 4385-91.

[YOU00]   Youngworth, K. S.; Brown, T. G., Focusing of high numerical aperture cylindrical-vector beams. *Optics Express* 2000, 7, 77-87.

[ZHA09]   Zhan, Q., Cylindrical vector beams: from mathematical concepts to applications. *Adv. Opt. Photon.* 2009, 1, 1-57.

[ZHA13]   Zhang, D.; Meixner, A. J., Book Chapter, Parabolic Mirror Assisted Gap-Mode Optical Ultramicroscopy. In *Handbook of Molecular Plasmonics*, Singapore, P. S. P., Ed. 2013; p 450.

7. Appendix

7.1. Scientific Contributions

7.1.1. Publications

[1]   Failla, A. V.; Jager, S.; Zuchner, T.; Steiner, M.; Meixner, A. J., Topology measurements of metal nanoparticles with 1 nm accuracy by Confocal Interference Scattering Microscopy. *Optics Express* 2007, 15, 8532-42.

[2]   Fleischer, M.; Zhang, D.; Braun, K.; Jager, S.; Ehlich, R.; Haffner, M.; Stanciu, C.; Horber, J. K. H.; Meixner, A. J.; Kern, D. P., Tailoring gold nanostructures for near-field optical applications. *Nanotechnology* 2010, 21, 065301.

[3]   Zeeb, B.; Jager, S.; Schafer, C.; Nill, P.; Meixner, A. J.; Kern, D. P.; Fleischer, M., Self-aligned gold nanocone probe tips. J*ournal of Vacuum Science & Technology B* 2010, 28, C6o34-C6o37.

[4]   Hentschel, M.; Dorfmuller, J.; Giessen, H.; Jager, S.; Kern, A. M.; Braun, K.; Zhang, D.; Meixner, A. J., Plasmonic oligomers in cylindrical vector light beams. *Beilstein journal of nanotechnology* 2013, 4, 57-65.

[5]   Jäger, S.; Kern, A. M.; Hentschel, M.; Jäger, R.; Braun, K.; Zhang, D.; Giessen, H.; Meixner, A. J., Au Nanotip as Luminescent Near-Field Probe. *Nano Letters* 2013, 13, 3566–3570.

[6]   Fulmes, J.; Schäfer, C.; Jäger, S.; Gollmer, D. A.; Horrer, A.; Zhang, D.; Adam, P.-M.; Meixner, A. J.; Kern, D. P.; Fleischer, M., Mapping the electric field distribution of cylindrical vector beams with gold nanorings. In preperation 2014.

7.1.2. Conference Contributions

[1]   Jäger, S., Hentschel, M., Braun, K., Zhang, D., Meixner, A.J., Giessen, H. Magnetoinduktive Kopplung und laterale Propagation optischer Anregungen in Metamaterial–Ketten auf der Nanometer–Skala. *Statusworkshop Kompetenznetz Funitionelle Nanostrukturen* 2009 Bad Herrenalb (Poster)

[2]   Jäger, S., Hentschel, M., Braun, K., Zhang, D., Meixner, A.J., Giessen, H. Magnetoinduktive Kopplung und laterale Propagation optischer Anregungen in Metamaterial–Ketten auf der Nanometer–Skala. *Statusworkshop Kompetenznetz Funitionelle Nanostrukturen* 2010 Bad Herrenalb (Poster)

[3]   Jäger, S., Braun, K., Zhang, D., Meixner, A.J., Langguth L., Liu N., Weiss T., Giessen, H. Lichtausbreitung in gekoppelten Metamaterialien *Forschungstag Hochtechnologieforschung* 2010 Stuttgart (Poster)

[4]   Jäger, S., Hentschel, M., Braun, K., Zhang, D., Meixner, A.J., Giessen, H. Magnetoinduktive Kopplung und laterale Propagation optischer Anregungen in Metamaterial–Ketten auf der Nanometer–Skala. *Statusworkshop Kompetenznetz Funitionelle Nanostrukturen* 2011 Bad Herrenalb (Poster)

[5]   Jäger, S., Braun, K., Fleischer, M., Zhang, D., Kern, D., Meixner, A.J., Selective Plasmonic Excitation of Rotationsymmetric Nanostructures. *SPIE Optics and Photonics* 2011 San Diego, USA (Poster)

[6]   Jäger, S., Braun, K., Fleischer, M., Zhang, D., Kern, D., Meixner, A.J., Selective Plasmonic Excitation of Rotation-Symmetric Nanostructures. *Quantum and Nano Plasmonics (491. Wilhelm und Else Heraeus-Seminar)* 2012 Bad Honnef (Poster)

[7]   Jäger, S., Kern, A.M., Hentschel, M., Braun, K., Zhang, D., Giessen, H., Meixner, A.J., Visualisation of ringmodes in plasmonic aromatic-molecules. *11th International Conference on Hole Burning, Single Molecule and Related Spectroscopies: Science and Applications* 2012 Tübingen (Poster)

[8]   Jäger, S., Kern, A.M., Hentschel, M., Braun, K., Zhang, D., Giessen, H., Meixner, A.J., Visualisation of ringmodes in plasmonic aromatic-molecules. *12th International Conference on Near-field Optics, Nanophotonics and Related Techniques (NFO12)* 2012 San Sebastian, Spain (Poster)

[9]   Jäger, S.; Kern, A. M.; Hentschel, M.; Jäger, R.; Braun, K.; Zhang, D.; Giessen, H.; Meixner, A. J., Sharp Gold-tip as Luminescent Nearfield Probe. *Forschungstag Hochtechnologieforschung* 2013 Stuttgart (Poster)

[10]   Jäger, S.; Kern, A. M.; Hentschel, M.; Jäger, R.; Braun, K.; Zhang, D.; Giessen, H.; Meixner, A. J., Au-Nanotip as Luminescent Near-Field Probe. *Statusworkshop Kompetenznetz Funitionelle Nanostrukturen* 2013 Bad Herrenalb (Talk)

7.2. Scientific Teachers

Prof. Dr. K. Albert   (Organic Chemistry)

Prof. Dr. T. Chassé   (Physical Chemistry)

Prof. Dr. D. Christen   (Physical Chemistry)

Prof. Dr. H. Eckstein   (Organic Chemistry)

PD Dr. H.-J. Egelhaaf   (Physical Chemistry)

Prof. Dr. G. Gauglitz   (Physical Chemistry)

Prof. Dr. G. Häfelinger   (Organic Chemistry)

Prof. Dr. V. Hoffmann   (Physical Chemistry)

Prof. Dr. N. Kuhn   (Inorganic Chemistry)

Prof. Dr. E. Linder   (Inorganic Chemistry)

Prof. Dr. M. E. Maier   (Organic Chemistry)

Prof. Dr. H. A. Mayer   (Inorganic Chemistry)

Prof. Dr. A. J. Meixner   (Physical Chemistry)

Prof. Dr. H.-J. Meyer   (Inorganic Chemistry)

Prof. Dr. U. Nagel   (Inorganic Chemistry)

Prof. Dr. H. Oberhammer   (Physical Chemistry)

Prof. Dr. C. Ochsenfeld   (Theoretical Chemistry)

PD Dr. G. Reinhardt   (Physical Chemistry)

Prof. Dr. V. Schurig   (Organic Chemistry)

Prof. Dr. E. Schweda   (Inorganic Chemistry)

Prof. Dr. Dr. h.c. J. Strähle   (Inorganic Chemistry)

Prof. Dr. U. Weimar   (Physical Chemistry)

Prof. Dr. L. Wesemann   (Inorganic Chemistry)

Prof. Dr. K. P. Zeller   (Organic Chemistry)

Prof. Dr. T. Ziegler   (Organic Chemistry)

7.3. Acknowledgement

I thank *Prof. Alfred J. Meixner* for the supervision of my PhD thesis and for the opportunity to carry out my research in his group. Additionally I like to say "thank you" for his trust in me to organize the movement of the lab from one building in the other.

I also want to thank *Dr. Marc Brecht* for his willingness to be referee of this Thesis.

For all his hard working synapses and transistors I like to thank *Dr. Andreas M. Kern* because of his marvelous work for the simulations I needed and his patience in the discussions of my results.

A very special "Thank You" I like to say to *Regina Jäger* for her everlasting support, all the discussions, the joint efforts in the lab and for being my beloved wife.

I thank *Kai Braun* for his support in questions of technical nature especially for the explanations of the Near-field microscopy techniques.

Thanks to *Dr. Dai Zhang* for the stimulating discussions and for letting me use the parabolic mirror microscope.

For the fruitful discussions and the common work at the microscopes in the 4th floor I like to thank *Frank Wackenhut*, with whom I implemented a multi source mode conversion system and other improvements to the microscopes.

I also want to say thank you to all other members of the *Nano-Optics group* for the good atmosphere and all the discussions.

I want to thank the people of the *AG Kern* in the physics department of the University of Tübingen for all the nice samples they had produced for this thesis. Namely *Dr. Monika Fleischer, Julia Fulmes, Christian Schäfer, Dominik Gollmer Dr. Peter Nill* and *Bastian Zeeb*.

Thank you to *Dr. Mario Hentschel* and *Prof. Harald Giessen, University Stuttgart* for the nice samples they have provided as well as for the good discussions of our common project.

7.4. Curriculum Vitae

Name:	Sebastian Jäger
Geburtstag:	26. Mai 1981 in Albstadt
Staatsangehörigkeit:	Deutsch
Familienstand:	verheiratet mit Regina Jäger geb. Nold
	keine Kinder

Ausbildung:

09/1987 – 07/1996	Schillerschule, Grund-, Haupt- und Werkrealschule, Albstadt Onstmettingen, Hauptschulabschluss
09/1996 – 07/1998	Walther-Grotz-Schule, Albstadt Ebingen, Kaufmännische Berufsfachschule, Fachschulreife
09/1998 – 06/2001	Phillip-Matthäus-Hahn-Schule, Technisches Gymnasium fachgebundene Hochschulreife (Note 1,8)
07/2001 – 03/2002	5. Panzergrenadierbataillon 294, Stetten a. k. M. Wehrdienst
04/2002 – 01/2007	Eberhard-Karls-Universität Tübingen, Diplomstudiengang Chemie Abschluss: Diplom Chemiker (Note: gut)

Ehrenamtliches Engagement:

09/1995 – 09/2011	Riegenführer in der Jugendschwimmausbildung DLRG Ortsgruppe Tailfingen
Sprachen:	Deutsch (Muttersprache), Englisch (fließend in Wort und Schrift)